

Universita' di Pisa

Dipartimento di Fisica.

Thesis for the XXIX Cycle of PhD in Physics

**THE QCD PHASE DIAGRAM AT
IMAGINARY CHEMICAL POTENTIAL**

Michele Mesiti

Supervisor:

M. D'Elia

Introduction

QCD has been established as the fundamental theory describing strong interactions. Since the proof of asymptotic freedom[1, 2], this theory has received a lot of confirmations, showing its predictive power in the perturbative regime and in the low energy sector. Nonetheless, big issues are still open. As an example, the features of the phase diagram of QCD still remain really difficult to study from the theoretical point of view: while at zero density it has been possible to do extensive numerical simulations starting from first principles, at finite density there are very few certainties.

From the experimental point of view, the phase diagram is being studied with heavy ion collision experiments, where strongly interacting matter is heated in the collision, melting into - according to theoretical predictions - a plasma of quark and gluons, and subsequently cooling down and “condensing” into hadrons again. The properties of the quark-gluon plasma can be inferred by looking at various experimental probes, and by analyzing the hadrochemical composition of the product of the collisions it is possible to recover some information on the phase structure of QCD, namely the chemical potential and the temperature at which the hadrons are formed.

From the theoretical standpoint, several effective approaches have been devised to (at least try to) make predictions on the structure of the QCD phase diagram. The obvious fields of application where this fundamental knowledge would be of great interest would be in the physics of the early universe, and in the understanding of the properties of neutron stars. In the study of gauge theories in general, a lot of achievements have been reached in the last decades with numerical methods based on lattice discretizations of the fundamental theory: with this approach, the infinite dimensional path integrals of the continuum theory are approximated with finite dimensional integrals, and approximated versions for all observables and their moments can then be written in the discretized theory. Via a careful tuning of the parameters in the chosen lattice formulation of the theory (which are *dimensionless*), it may be possible to reduce the corresponding physical value of the lattice spacing, thus approaching the *continuum limit*, and by enlarging the lattice it is possible to approach the *thermodynamic limit*, towards the real theory which lives in a continuum, infinite space. The *cut-off* and the *finite volume* effects on the approximated observables can be assessed by evaluating them on lattices with different values of the lattice spacings and different size, and an estimate of the physical quantities in the physical theory can thus be given, once the necessary renormalizations are carried out.

The methods commonly used for evaluating the path integrals of the discretized theory are based on *importance sampling*: the integration domain is sampled mostly in the regions which give the largest contributions. The individuation of such regions, and this approach in general, are straightforward if the integrand is a positive definite quantity which can be interpreted as a probability density. Else, the calculation is affected by the so called *sign problem*.

As an example, *real time* QCD is affected by this problem beyond any hope (at least at present). Lattice QCD is indeed formulated at imaginary time, where the sign problem is, at least in the simplest cases,

absent: while of course this approach does not allow to study real time dynamics, it is very fruitful for investigating the time-independent thermodynamic properties of the theory. Unfortunately, even in the context of QCD thermodynamics, the sign problem arises in other circumstances: most notably, and for what we are concerned here, in the presence of a non-zero baryon chemical potential μ_B , where the fermion determinant becomes complex.

Various approaches have been tried to circumvent this problem. Reweighting methods can be used, where the sampling is done according to a probability density defined *ad hoc* (for instance, the one for zero chemical potential) and then the computed values of the observables are re-weighted according to the ratio between the “ad hoc” probability density and the original factor. Of course these methods have some limits: first, the region of field space explored with the modified importance sampling can actually be quite different from the one we are interested in, and due to the fact that the new ensemble has finite size this can lead to huge errors: this is the so-called *overlap* problem. Moreover, the reweighting ratio can be affected by huge statistical uncertainties while becoming exponentially small with the volume, thus making the thermodynamic limit hard to explore¹.

Another possible approach that allows to use the ensemble extracted at zero chemical potential is the Taylor expansion method. The observables are expanded in Taylor series and the derivatives in the chemical potential which make up the series are measured on the lattice. Clearly, this method will work only for small enough μ_B . Moreover, in general, higher order derivatives can be very expensive to compute precisely.

It is also possible to exploit the fact that the fermion determinant is actually *real* for imaginary values of the chemical potential, so the sign problem is absent. Then, thanks to the fact that for finite systems the partition function is analytic, we can use analytic continuation to obtain information for small enough real μ . This is the approach used in the work that will be described in the following thesis.

Given the importance of the subject, it is no surprise that many other more sophisticated approaches have been devised to attack this problem. As an example, the grand canonical partition function can be evaluated at imaginary baryon chemical potential (without the sign problem), and its Fourier coefficients are the canonical partition functions for a fixed value of the baryon number². Unfortunately the sign problem reappears in the Fourier transform, and is mitigated only for small values of the total baryon number: this makes the thermodynamic limit at fixed baryon density hard to study, as with the re-weighting method.

Some groups have been recently exploring approaches whose validity is yet to be completely justified. As an example, complex Langevin dynamics just avoids importance sampling, and use stochastic quantization to explore the complexified integration domain, for real chemical potential. This is in principle possible if the action is an analytic function (unfortunately the logarithm of the fermion determinant is not analytic). While there have been some successes for toy models and simplified theories, there is no proof that this procedure converges to the right result in the case of complex actions, and current studies still focus on the fundamentals.

However, the possibility of studying QCD at imaginary chemical potentials is also interesting *per se*. The phase diagram of QCD at imaginary μ_B shows interesting features, like the so-called Roberge-Weiss phase transition. The structure of the phase diagram becomes even richer when one considers also the quark masses as free parameters, and can be put in relation to the so-called “Columbia plot” at vanishing chemical potential, where the order of the deconfinement-chiral phase transitions are displayed as a function of the light and strange quark masses. Moreover, the pure-imaginary μ_B situation can work

¹This is due to the fact that this ratio is the exponential of the difference of two free energies, which are extensive quantities.

²In other words, the canonical partition functions are the coefficient in the *fugacity expansion* of the grand canonical partition function, where the fugacity is $e^{-\mu/T}$.

as a testbed for the validity of some effective approaches used to make predictions on the phase diagram at real μ_B , provided that those approaches can be extended to imaginary chemical potentials.

In the first Chapter of this thesis, a brief introduction to the relevant topics in Lattice QCD will be given. It is by no means intended to be a comprehensive exposition, but just a collection of important results and references to give the context for the following parts. Chapter 2 is about the determination of the curvature of the critical line of QCD, with a brief introduction to the experimental context. Chapter 3 is about the determination of the properties of the Roberge-Weiss transition, for physical quark masses and towards the chiral limit. In Chapter 4 the main results and possible future developments of the present work are summarized.

Finally, in the appendices, a Lattice QCD code implementation making use of OpenAcc (used for the most recent data presented in Chapter Three) is described.

Contents

Introduction	i
1 Lattice QCD	1
1.1 Path Integrals, Lattice actions	1
1.2 Fermions on the lattice: the no-go theorem and staggered fermions	2
1.3 Finite density and the sign problem	4
1.4 QCD: Center and chiral symmetry	5
1.4.1 The chiral transition and deconfinement	5
1.4.2 The phase diagram of QCD as a function of mass and imaginary chemical potential	6
1.4.3 Center symmetry and the fermion determinant	8
1.5 General Remarks on the numerical setup	11
1.5.1 Line of Constant physics and scale setting	12
2 The critical line of QCD and analytic continuation	14
2.1 Phenomenology of the QCD phase diagram	14
2.2 Heavy Ion collision Experiments	16
2.2.1 Theoretical description of Heavy Ion collision	16
2.2.2 Experiments probing the phase diagram of QCD	18
2.3 Lattice QCD and Analytic Continuation	20
2.4 Numerical setup and observables	21
2.4.1 Setup of chemical potentials	22
2.4.2 Observables on the Lattice, Renormalization and location of $T_c(\mu_B)$	23
2.5 Analytic continuation with and without a strange quark chemical potential	24
2.6 Numerical Results	26
2.6.1 Continuum limit for $\mu_s = 0$ - First method	30
2.6.2 Continuum limit for $\mu_s = 0$ - Second method	33
2.6.3 Strength of the transition as a function of μ_B	34
2.6.4 Inclusion of $\mu_s \neq 0$ and systematics of analytic continuation	36
2.6.5 Discussion of results	37
2.7 Parameter sets and data at $T = 0$	38
2.8 Comparison with other determinations in the literature	39
2.8.1 Comparison with other methods	39
2.8.2 The curvature of the critical line in the literature	41
2.9 Conclusions	44
3 At Large $\text{Im}\mu_B$: the Roberge-Weiss phase transition	46
3.1 The Roberge-Weiss transition	46
3.1.1 The Roberge Weiss transition in the literature	47
3.1.2 Our goals	48
3.1.3 Determination of the order of the transition: Finite size scaling	49
3.1.3.1 The case of a tricritical point	50
3.1.3.2 The first order case	51

3.1.3.3	The Binder cumulant and finite size scaling	53
3.2	Location of the Roberge-Weiss-like transition for $\mu_s = 0$	53
3.2.1	One loop Polyakov effective potential	54
3.3	General framework and numerical setup	55
3.4	Numerical Results for physical quark masses	57
3.4.1	Finite size scaling and universality class of the transition	57
3.4.2	Critical temperature: continuum extrapolated value	60
3.4.3	Relation with the pseudocritical chiral transition line	61
3.4.4	Conclusions	62
3.5	Towards the chiral limit	64
3.5.1	Results for finite size scaling	64
3.5.2	The light chiral susceptibility at the RW transition	66
4	Conclusions and Outlooks	68
A	Implementation of a full dynamical fermions Monte Carlo with Hybrid parallelism (OpenAcc and MPI)	70
A.1	Numerical challenges of Lattice QCD	70
A.1.1	Why LQCD is a computational grand challenge	71
A.1.2	Numerical algorithms for LQCD	72
A.1.3	Data structures and computational challenges	73
A.2	Gauge and Fermion improvements	74
A.2.1	Stout Fermions	74
A.2.2	Tree Level Symanzik improvement	74
A.3	OpenAcc implementation of the Lattice QCD code	75
A.3.1	Memory allocation structure	75
A.3.2	Implementation of the full algorithm	77
A.3.3	Multi-rank implementation	81
B	Measurement of Fermionic observables	86
B.1	Noisy estimators and noise vectors	86
B.1.1	Errors	87
B.2	Chiral condensate	88
B.3	Nonzero chemical potential on the lattice and the quark number	90
B.3.1	The case of a biased estimator: $ \text{Im}N $	91
B.3.2	A pedagogical failure: the susceptibility of $ \text{Im} n_l $ at the transition	92
	Bibliography	94

Chapter 1

Lattice QCD

1.1 Path Integrals, Lattice actions

Lattice QCD is a discretized version of QCD which uses a lattice as a ultraviolet regulator, approximating the path integral in the continuum with a finite dimensional integral. In this approach, the fermion fields live on the lattice vertices, while the gauge fields retain their meaning of a “connection” being replaced by the parallel transport operators, or “links”, which represent the exponentiation of the path ordered integral of the original gauge fields in the continuum (in practice, they are $SU(3)$ matrices). If we Wick-rotate the time axis in the complex plane with the transformation $t = -i\tau$, then the Minkowski metric becomes the Euclidean one in four dimensions, and the gamma matrices, the partial derivative and the gauge fields transform accordingly. With the lattice approach, it is possible to study the thermodynamic properties of QCD. In this Wick-rotated system, we take periodic boundary conditions on the τ axis for the gauge fields, and anti-periodic boundary conditions for the fermionic fields. The finite extent of the lattice in the Euclidean time direction is proportional to the inverse of the temperature, with a proportionality constant given by the lattice spacing in physical units¹.

The Euclidean path integral can be written as

$$Z = \int DU D\bar{\psi} D\psi \exp[-(S_g^E + S_f^E)] = \int DU \exp(-S_g^E) \text{Det}(M_f^E) \quad (1.1)$$

where S_g^E is the gauge part of the Euclidean action which is expressed in terms of the $SU(3)$ links denoted as U , while the integration of the fermionic quark fields ψ , which in the path integral formalism require to be treated as Grassmann variables, has yielded the determinant of the Euclidean Dirac operator $M_f^E = [\gamma_\rho^E (\partial_\rho - igA_\rho) + m]$. The Gauge part of the QCD Euclidean action in the continuum can be discretized as

$$S_g^E = \sum_{n,\mu,\nu} [1 - \text{Re Tr } W_{\mu,\nu}^{1 \times 1}(n)] , \quad (1.2)$$

where $W_{\mu,\nu}^{1 \times 1}(n)$ represents the product of the four $SU(3)$ “links” U around a *plaquette* in the $\mu - \nu$ plane. This action, called the Wilson Gauge action, is the simplest one. The possible choices are infinite and the only requirement is that they give the correct continuum limit. This freedom has been exploited to construct different “improved” actions, which make use of next-to-nearest-neighbor terms to improve

¹ Here and in the following natural units, that is the convention $\hbar = c = 1$, are used.

convergence to the continuum limit. Thanks to various improvements it has been possible to study QCD with physical quark masses, obtaining quantitative results on real-world physics. An example of improvement to the gauge action, derived from the ‘‘Symanzik improvement program’’ [3, 4] is the tree-level Symanzik action [5, 6, 7]. It is worth mentioning also the Iwasaki action [8], which was instead obtained from renormalization group considerations. The way fermions are introduced in the theory requires a separate discussion, given the importance and complications involved.

1.2 Fermions on the lattice: the no-go theorem and staggered fermions

As can be easily seen, a naive discretization of the Dirac Lagrangian leads to the so-called ‘‘fermion doubling’’ problem: the periodicity of the lattice and the use of the symmetric discretization of the first derivative make so that the dispersion relation has 2^D different zeros (in the massless case) in the first Brillouin zone, even in the continuum limit. This implies there are 2^D linearly independent fermion-like excitations, which are called ‘‘doublers’’ (see e.g. [9] for an illustration of the problem). Different strategies have been devised in order to circumvent this issue. The first attempt consists in the so-called Wilson fermions formulation: an irrelevant term proportional to a second order derivative is added to the Lagrangian, which vanishes as a higher power of the lattice spacing a in the continuum limit, while at the same time suppressing the doublers. One of the major problems related to this ploy is that the newly added term is, Dirac-indices-wise, exactly like a mass term, which breaks explicitly chiral symmetry. Moreover, since the newly added term and the mass term have the same symmetries, they mix, thus implying that quark mass renormalizes additively.

Another possible approach are the so-called ‘‘Staggered’’ (or Kogut-Susskind) fermions. This approach is based on the fact that the naive fermion action has a four-fold degeneracy: it can be seen, by acting on the fermion field with the point dependent transformation

$$T(n) = \gamma_1^{n_1} \gamma_2^{n_2} \gamma_3^{n_3} \gamma_4^{n_4} , \quad (1.3)$$

where n_1, \dots, n_4 represents the (integer) coordinated of the point, that the Dirac operator is diagonalized in the Dirac indices, and the four-fold degeneracy becomes evident:

$$T^\dagger(n) \gamma_\mu T(n + \hat{\mu}) = \eta_\mu(n) \mathbf{1} . \quad (1.4)$$

The quantities $\eta_\mu(n)$ (called ‘‘staggered phases’’) are just ± 1 factors, as it can be easily computed:

$$\eta_\mu(n) = (-1)^{n_1 + \dots + n_{\mu-1}} , \quad \eta_1(n) = 1 . \quad (1.5)$$

Exploiting this degeneracy, we are allowed to take only one of the four Dirac components of the field, which we will call $\chi(n)$. The fermionic action written in terms of $\chi(n)$ reads

$$S_F^{stag} = \frac{1}{2} \sum_{n, \mu} \eta_\mu(n) \bar{\chi}(n) [\chi(n + \hat{\mu}) - \chi(n - \hat{\mu})] + am \sum_n \bar{\chi}(n) \chi(n) \quad (1.6)$$

(the mass term is trivial). Exploiting the fact that the staggered phases $\eta_\mu(n)$ are periodic in n in all four directions, we can decompose the lattice in cubes with dimensions 2^4 , and decompose the index n in an index N and an index ρ , with N indicating the 2^4 block and ρ indicating the position within the 2^4 block.

With these ideas, the staggered fermion action can be rewritten as

$$S_F^{stag} = \frac{1}{2} \sum_{N,\rho,\mu} \eta_\mu(\rho) \bar{\chi}(2N+\rho) [\chi(2N+\rho+\hat{\mu}) - \chi(2N+\rho-\hat{\mu})] + am \sum_n \bar{\chi}(n) \chi(n). \quad (1.7)$$

We can also define a field $\chi_\rho(N) \equiv \chi(2N+\rho)$, having 2^4 components labeled by the multi-index ρ . By looking explicitly at Equation 1.7, it is possible to see that the ρ -labeled components of $\chi_\rho(N)$ represent 4 Dirac fields (commonly dubbed “tastes”), which are degenerate in the non interacting case. Moreover, it can be proven that a $U(1)$ symmetry, remnant of chiral symmetry in the continuum, still holds for the massless Dirac operator (see [9] for an explicit calculation).

The fact that the theory contains four fermions instead of one is, in general, undesired. In the case that this degeneracy is present in the fermion determinant, we have

$$\det M_{st} = (\det M)^4 \quad (1.8)$$

So we are lead, in order to recover the determinant for a single fermion species, to take the fourth root [10]:

$$\det M = \det M_{st}^{1/4}. \quad (1.9)$$

In the actual simulation, the quantities derived from $\det M_{st}^{1/4}$ are computed using a rational approximation, which can be efficiently implemented in the algorithm. However, there are a number of problems related to rooting. The validity of the rooting procedure and the systematics related to it have been debated in the literature [11, 12, 13, 14] (for a review, see also [15]). In particular, when rooting is used the chiral limit $m_q \rightarrow 0$ and the continuum limit $a \rightarrow 0$ do not seem to commute, and in principle at finite lattice spacing there are some spurious effects due to the symmetries of the underlying unrooted staggered formulation. The conclusions that can be drawn these studies is that if one wants to study the physical chiral limit, the continuum limit must be taken first.

At the time of writing, staggered fermions are the cheapest strategy to perform simulations relevant to real-world physics.

One of the main practical issues is that rooting is justified only when the 4 “tastes” are exactly degenerate. Unfortunately, the doublers interact with each other thanks to high-moment gluons, through the so called taste-exchange interactions, which are suppressed in the continuum limit, and according to [16] make up the largest part of the $\mathcal{O}(a^2)$ cutoff effects in the staggered formulation, even larger than the ones coming from the discretization of the derivative, which are $\mathcal{O}(a^2)$ as well. A cheap possibility to reduce taste exchange interactions is *stouting*, where the gluon fields are smoothed in an analytic way [17] when entering the Dirac operator. This is the choice that will be used in the present work. In order to quantify taste symmetry violation it is possible to measure the two-point correlators for staggered mesons [18, 19]. In Fig.1.1 a measurement of the pion multiplet masses for the action of our choice is shown.

An alternative is using the so-called HISQ action [16], implemented in the MILC code, engineered specifically to suppress taste-exchange interactions. For a general comparison between variations of the staggered discretization and their effectiveness in dealing with taste symmetry violations, the reader can refer to [21].

In general, any discretization of Dirac fermions has to cope with the limitations due to the Nielsen-Ninomiya no-go theorem [22, 23, 24], from which it can be proven that with a fermionic discretization which respects hermiticity, locality and translational invariance, the doubler problem cannot be solved while

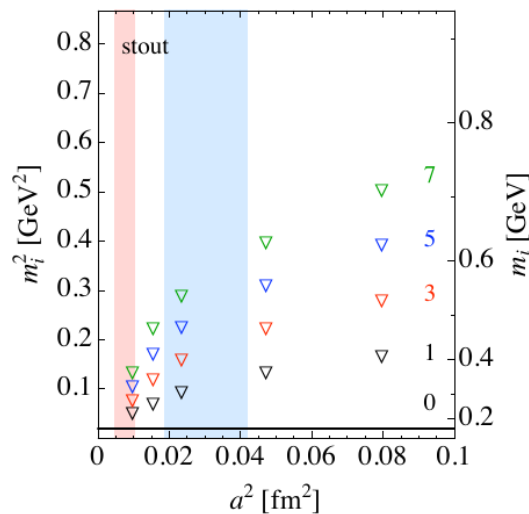


FIGURE 1.1: Masses for some of the pion multiplets (related to some irreducible representations of the staggered fermion symmetry group) for the action used in the present work, as a function of the lattice spacing. The black line at the bottom represents the physical pseudo-Goldstone boson, at 135 MeV. Figure taken from [20].

also keeping chiral symmetry intact in the fermionic action. It has been proven that a “minimal” violation of chiral symmetry on the lattice can be described by the Ginsparg-Wilson relation [25]:

$$\{D, \gamma_5\} = aD\gamma_5D. \quad (1.10)$$

It may be interesting that, apart from a different constant factor on the r.h.s., this equation is satisfied by the “blocked” (in the Renormalization Group idea) free Dirac operator. A Dirac operator satisfying this relation in the interacting case is the Neuberger Overlap Operator [26]. Such a Dirac operator would also satisfy exactly a variation of chiral symmetry, which tends to the proper chiral symmetry in the continuum [27]. Other notable implementations of fermions on the lattice are Domain Wall fermions, where chiral fermions are represented as domain walls along a fifth lattice dimension (whose finiteness causes an explicit breaking of chiral symmetry), and Twisted mass fermions, where a theory with two degenerate flavors of Wilson fermions is modified with a mass term which is not the identity in isospin space. For a rather recent and brief review on the subject, the reader can refer e.g. to [28], §7 and §10.

1.3 Finite density and the sign problem

Let us start with a system where just a single quark species is present (the generalization is straightforward). We wish to use a path integral representation of the grand canonical partition function, with μ as the thermodynamic potential associated to quark number Q .

$$Z = \text{Tr} e^{-H - \mu Q}, \quad Q = \int d^3x \bar{\psi}(x) \gamma_0 \psi(x). \quad (1.11)$$

The partition function must be even in μ , to satisfy charge conjugation symmetry. More explicitly,

$$Z = \int DAD\bar{\psi}D\psi \exp \left\{ -\frac{1}{4} F_{\lambda\rho} F_{\lambda\rho} + \bar{\psi} [\gamma_\rho (\partial_\rho - igA_\rho) - \mu \gamma_0 + m] \psi \right\}. \quad (1.12)$$

Note that the term containing the chemical potential looks like a minimal coupling term between the quark current and a $U(1)$ fixed gauge field directed in the temporal direction. Using this analogy, we can introduce the chemical potential on the lattice by multiplying all the links in the temporal direction by $e^{-a\mu}$, where a is the lattice spacing². In (1.1), this entails the dependence on μ of the fermion determinant $Det(M)$.

Let us see now how this causes the infamous *sign problem*. In the case of zero chemical potential, the Dirac Operator is γ_5 -hermitian:

$$(\not{D} + m)^\dagger = \gamma_5 (\not{D} + m) \gamma_5 . \quad (1.13)$$

If a chemical potential is present, we have

$$\gamma_5 (\not{D} + m - \gamma_0 \mu) \gamma_5 = (-\not{D} + m + \gamma_0 \mu) = (\not{D} + m + \gamma_0 \mu^*)^\dagger . \quad (1.14)$$

For the determinant, this implies

$$Det (\not{D} + m - \gamma_0 \mu) = [Det (\not{D} + m + \gamma_0 \mu^*)]^* \quad (1.15)$$

which means that the determinant is real if and only if μ is purely imaginary, otherwise it is in general complex. This means that the integrand in (1.12) is complex, and the integral cannot be evaluated with straightforward importance sampling methods. We choose instead to avoid this problem and study the theory at imaginary chemical potential[30], and in order to recover information about the theory at real μ we just use *analytic continuation*. This is justified by the fact that the lattice theory in a finite volume has a finite number of degrees of freedom, and this means that all observables should be analytic in the parameters of the theory³.

1.4 QCD: Center and chiral symmetry

1.4.1 The chiral transition and deconfinement

The changes expected for the properties of strongly interacting matter when it is put under extreme conditions are the subject of vast ongoing theoretical and experimental research efforts. Various parameters of phenomenological interest enter the description of such extreme conditions, like temperature, chemical potentials or external background fields. Part of this research consists in the study of the QCD phase diagram, that is in mapping the various phases of strongly interacting matter in equilibrium conditions (with the associated phase transitions and critical points) as a function of those parameters.

At high temperature confinement and chiral symmetry breaking are expected to disappear, and QCD is expected to be described in terms of quark and gluon effective degrees of freedom, in the so-called quark-gluon plasma phase. Lattice QCD simulations show that, indeed, a rapid change of properties takes place around a well defined temperature T_c . There is no compelling reason for expecting a true phase transition, since no exact symmetry of QCD, which could possibly change its realization at T_c , is known: chiral symmetry is exact only for vanishing quark masses, while the Z_3 center symmetry is

²Implementing a non-zero chemical potential in the *naive* way, that is adding a term $\sum_x \bar{\psi}(x) \gamma_0 \psi$ to the lattice action, leads to a non renormalizable lattice theory (see, for example, [29]).

³Obviously, this becomes false in the thermodynamic limit, where real phase transitions can occur. Clearly, in general, analytic continuation cannot be performed beyond such singularities.

exact only in the pure gauge theory, where its spontaneous breaking is associated to deconfinement. In fact, lattice simulations have shown that only a smooth crossover is present in the case of physical quark masses, at a temperature $T_c \sim 155 \text{ MeV}$ ⁴ [20, 31, 32, 33, 34].

The situation could be different in the presence of other external parameters. In particular, and most importantly for what we are concerned here, the crossover could turn into a real transition for large enough baryon chemical potential μ_B , starting from a critical endpoint in the $T - \mu_B$ plane. Such a critical point, and the associated critical behavior around it, could have a huge impact on strong interactions phenomenology, so that large theoretical and experimental efforts are being dedicated to investigate its existence and locate it.

1.4.2 The phase diagram of QCD as a function of mass and imaginary chemical potential

In the chiral and quenched limits there are two different order parameters for chiral symmetry and center symmetry, namely the chiral condensate and the Polyakov loop respectively. At zero chemical potential, these symmetries are both explicitly broken at finite mass: chiral symmetry is exact only at zero mass, while center symmetry is exact only in the infinitely-heavy-quark limit.

The phase diagram at zero chemical potential, as a function of the light quark mass m_l (take equal for the up and down quarks) and the strange quark mass m_s , has been studied extensively. The order of the transition in $N_f = 2 + 1$ QCD can be displayed as a function of light quark mass m_l and the strange quark mass m_s in the so-called Columbia plot [35] (see Fig.1.2, left). An important analytical work is [36], where the chiral transition was studied making use of an effective Lagrangian and a renormalization group analysis. An important conclusion is that, for $m_l = m_s = m_q$ (that is, the $N_f = 3$ case) the chiral phase transition must be first order in the chiral limit⁵. The expected effect of a nonzero quark mass m_q , which breaks explicitly chiral symmetry, is to weaken the 1st order chiral transition, up to the point where it becomes second order, in the Ising 3D universality class [38]; at larger masses a crossover takes places instead of a proper transition. At a sufficiently large value of the quark mass, the explicit violation of center symmetry decreases in magnitude, up to the point where a second-order phase transition appears, related to confinement. In [39] the Authors study the case of a single fermion with a large mass. Here the universality class is the one of a 3-state Potts model, with an external magnetic field associated to one spin direction[40] in the case of finite quark mass, thus breaking explicitly the Z_3 center symmetry to Z_2 : again, the second order transition is in the Ising 3D universality class. Then beyond this second order point the transition becomes 1st order as in the $SU(3)$ pure gauge theory [41].

The case with $m_s \neq m_l$ is of course more complex. Some results obtained in the $N_f = 3$ case, that is on the diagonal of the Columbia plot, can be extended by continuity to the neighboring regions. There are anyway some issues which still need to be investigated. In particular, in the $m_l = 0, m_s = \infty$ case ($N_f = 2$) there is not a clear-cut answer about the nature of the phase transition in the continuum limit, even if for finite lattice spacing ($N_t = 4$) it has been proven to be 1st order (see [42] and references therein for a broader view of the issue). The difficulty in studying this problem stems from the fact that when the

⁴This is the value obtained by defining T_c as the temperature at which the renormalized chiral condensate (defined as in Eq.2.13) has an inflection point.

⁵It is interesting to note how difficult it is to verify this in lattice simulations. For a recent review of the subject, see [37] and references therein.

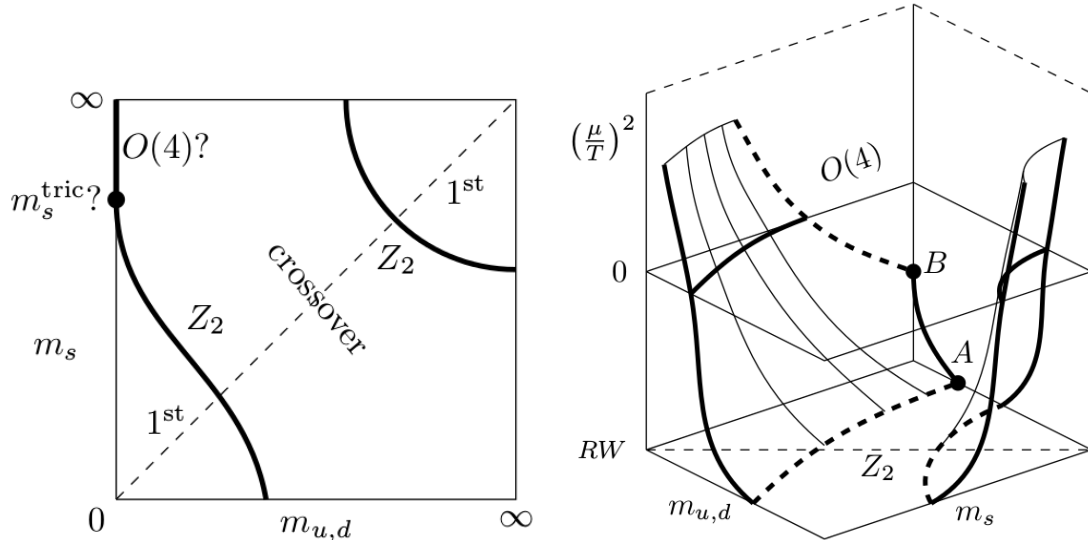


FIGURE 1.2: **Left:** A Possible Columbia plot at zero density. **Right:** a possible Columbia plot with an additional parameter on the z axis, μ_q^2 . In both cases, a second order chiral transition is assumed in the chiral limit for $N_f = 2$, i.e. the upper left corner of the left plot. Both figures taken from [42].

quark mass goes to zero the computational cost of Montecarlo simulations increases making numerical simulations unfeasible⁶.

The opposite corner of the Columbia plot (which corresponds to $N_f = 1$) is not particularly interesting: for $N_f = 1$ the chiral group is only $U_B(1) \times U_A(1)$, and the axial $U_A(1)$ symmetry is spontaneously broken by instantons [43, 44, 45] at zero temperature, while baryon number conservation cannot be violated: the only possible phenomenon is a partial restoration of $U_A(1)$ at high temperature due to instanton suppression [36].

In the case of nonzero chemical potential, the phase diagram acquires another axis (see Fig.1.2, right) It has been noted empirically that the strength of the chiral transition is increased in the case where a nonzero imaginary chemical potential $\mu_{I,q}$ is present, i.e. that the 1st order zone around the $m_s = m_l = 0$ corner expands in this case. This suggests that, for large enough imaginary chemical potential $\mu_{I,q}$, even in the $N_f = 2$ case a first order transition may take place in the chiral limit, and at the endpoint of this first order line a second order transition will take place for $m_l = m_{l,crit.}(\mu_{I,q}^2)$.

As a remark to the reader, let us stress that the topic touched here has been developed in a vast literature, and is an active field of research. For a general review including the latest development see e.g. [46] and references therein.

⁶ This is due to the computational cost of the inversion of the Dirac Operator, which may depend (even greatly) on the algorithm used.

1.4.3 Center symmetry and the fermion determinant

The gauge part of the QCD action is invariant under a transformation that multiplies all the temporal links in a time slice by the same element of the *center* of $SU(3)$ ⁷, which consist of the \mathbf{Z}_3 group formed by the three complex roots of 1. Notice that, under such a *center transformation* of the links, the Polyakov loop P [47, 48], defined as

$$P \equiv \frac{1}{L^3} \left\langle \sum_{\vec{x}} \text{Tr} \prod_{\tau=1}^{N_\tau} U_4(\vec{x}, \tau) \right\rangle \equiv \frac{1}{L^3} \sum_{\vec{x}} \langle P(\vec{x}) \rangle, \quad (1.16)$$

will not be invariant unless it is zero. So, if *center symmetry* is intact, we expect the Polyakov loop to be zero.

The Polyakov loop has an interesting physical interpretation. Indeed,

$$P \propto e^{-F_q \tau}, \quad (1.17)$$

where $F(q)$ is the free energy of the system associated to the presence of an infinitely heavy quark. This can be justified computing the partition function of an infinitely heavy quark coupled to a dynamical gauge field (see [49], and [9], §20). When the Polyakov loop is zero, the free energy of an isolated heavy quark is infinite so all quarks are confined. If instead the Polyakov loop is nonzero, the free energy of a heavy quark is finite and isolated quarks are present: this signals quark deconfinement.

Montecarlo studies have extensively evidenced that at large T the value of P becomes non zero, which means that center symmetry is broken. In the Yang-Mills $SU(N)$ theory, there are N possible ground states of equal energy connected by center transformations. This means that in the broken phase we have $P \propto \exp\left(\frac{2\pi i}{N} k\right)$, with integer k .

The situation is different when dynamical fermions are included in the theory. From the Lagrangian point of view, center symmetry is broken explicitly by the presence of the fermion determinant. For zero chemical potential, this causes the Polyakov loop to be a real, positive value.

This has also an interesting physical interpretation. The *Polyakov loop correlator*

$$\Gamma(\vec{y}) = \frac{1}{L^3} \left\langle \sum_{\vec{x}} P(\vec{x}) P^\dagger(\vec{x} + \vec{y}) \right\rangle \quad (1.18)$$

can be put in relation, with a construction similar to the one used for the Polyakov Loop, to the potential energy of a quark-antiquark couple; indeed (see, e.g., [9], §20)

$$\exp(-V_{\bar{q}q}(y)) = \frac{\langle P(0) P^\dagger(\vec{y}) \rangle}{|\langle P \rangle|^2}. \quad (1.19)$$

If $|P|$ is nonzero, cluster property entails that, for $|y| \rightarrow \infty$, we have $\langle P(0) P^\dagger(\vec{y}) \rangle \rightarrow |\langle P \rangle|^2$. This means that $V_{\bar{q}q} \rightarrow \text{const}$ at large distance, instead of the confining $V_{\bar{q}q} \propto \sigma r$ (where σ is the string tension): this can be put in relation to the fact that, in a theory with dynamical fermions, the string breaks thanks to the polarization of the medium.

Some aspects of the effect of fermions on the Polyakov loop have been studied in [50]. In particular, the authors studied the effect of an imaginary chemical potential coupled to the quark number. As already

⁷The center of a group G is defined as the subgroup of the elements of G which commute with *all* the elements of G . For $SU(N)$, in the fundamental representation, it is basically $C = \{e^{i\lambda} \mathbf{1} : N\lambda = 2k\pi\}$.

stated in Section 1.3, for a theory with a single quark field the Euclidean partition function becomes (in the continuum)

$$Z(\mu_I) = \text{Tr} e^{-H-\mu Q} = \int D\psi D\bar{\psi} DA_\mu \exp\left(-\int d^4x \left[\bar{\psi}(\gamma_\mu D_\mu - m)\psi - \frac{1}{4}F^2 - i\mu_I \bar{\psi}^\dagger \psi\right]\right), \quad (1.20)$$

where μ_I is the imaginary part of the chemical potential, and D_μ is the covariant derivative $\partial_\mu - iA_\mu$. A key observation is that the introduction of μ_I amounts to the introduction of a real nonzero Abelian A_4 , which cannot be gauged to zero because of the boundary conditions on in the Euclidean time direction. Alternatively, the introduction of μ_I can be seen just as a change in the boundary conditions:

$$\psi(\vec{x}, 0) = -\exp(i\mu_I \tau) \psi(\vec{x}, \tau). \quad (1.21)$$

which again evidences a 2π periodicity in μ_I . Here τ represents the Euclidean time extension of the lattice. Notice that $\mu_I \tau$ is equal to the dimensionless ratio μ_I/T , where T denotes the temperature.

As evidenced in [50], if the system contains single quark states, the partition function has a 2π periodicity in μ_I , but if only colorless states are present, where the quark number Q is a multiple of the number of colors N , the partition function should have a $2\pi/N$ periodicity. This is evident when looking at Eq.(1.20). In the same work, starting from the results in [51, 52, 53], the Authors compute an effective potential for the Polyakov loop for the high temperature case.

It is possible to choose a gauge where A_4 has only diagonal components⁸. In such a gauge, we have that

$$P(\vec{x}) = \text{Tr} e^{i\phi(\vec{x})\tau} \quad (1.22)$$

with

$$\phi(\vec{x}) = \text{diag}(\phi_1(\vec{x}), \dots, \phi_N(\vec{x})), \text{ with } \sum_{i=1}^N \phi_i(\vec{x}) = 0 \text{ mod } 2\pi, \quad (1.23)$$

and $\partial\phi_i/\partial x_4 = 0$. The phases $\phi_i(\vec{x})$ can be written as a constant background field ϕ_i plus a perturbation $\delta\phi_i(\vec{x})$. An effective potential can be calculated for the constant field ϕ_i , which consists of two contributions: the one coming from the gauge part of the action, and the one coming from the fermionic part⁹ of the action:

$$V_{eff}^{glu}(\phi_1, \dots, \phi_N) = \frac{1}{24} \pi^2 T^4 \sum_{i,j=1}^N \left\{ \left[\left(\frac{\phi_i - \phi_j}{\pi T} \right)_{\text{mod } 2} - 1 \right]^2 - 1 \right\}^2, \quad (1.24)$$

$$V_{eff}^{ferm}(\phi_1, \dots, \phi_N) = -\frac{1}{12} \pi^2 T^4 \sum_{i=1}^N \left\{ \left[\left(\frac{\phi_i}{\pi T} + 1 \right)_{\text{mod } 2} - 1 \right]^2 - 1 \right\}^2. \quad (1.25)$$

The total potential will be the sum of the two contributions, with the fermionic one depending also on μ_I :

$$V_{eff}(\phi_1, \dots, \phi_N, \mu_I) = V_{eff}^{glu}(\phi_1, \dots, \phi_N) + V_{eff}^{ferm}(\phi_1 + \mu_I, \dots, \phi_N + \mu_I). \quad (1.26)$$

The minima of V_{eff}^{glu} , considering the constraint $\sum_{i=1}^N \phi_i/T = 0 \text{ mod } 2\pi$, are when all ϕ_i are equal to each other and $\phi_i/T = \frac{2\pi m}{N}$; moreover by making use of Lagrange multipliers, it can be also straightforwardly proven that V_{eff}^{ferm} is minimized *locally* by such solutions: this implies that there are N possible local

⁸Of course, due to boundary conditions, it is not possible to chose a gauge where A_4 is zero, but it is possible to make so that it is constant in x_4 and diagonal.

⁹The formula obtained for V_{eff}^{ferm} is in principle valid only for massless fermions. It can be argued though that quark mass should not be relevant in the high temperature limit ($T \gg m$), and this can be explicitly checked in the computation of V_{eff}^{ferm} (see [52]).

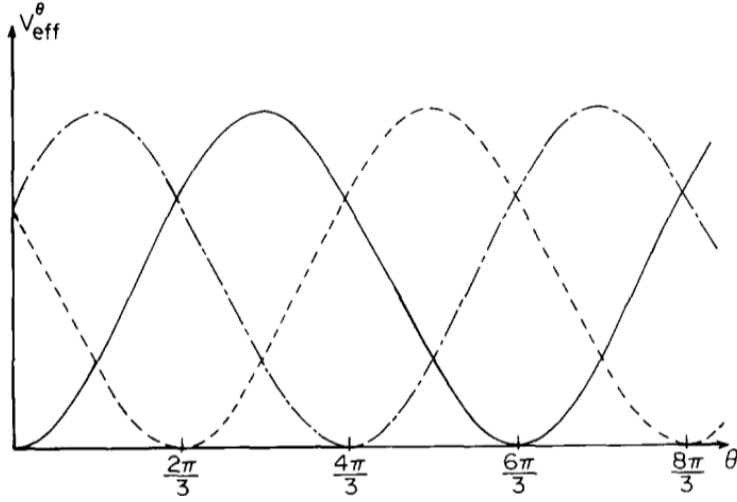


FIGURE 1.3: The effective potential for the three different center sector of $SU(3)$ as a function of $\theta = \mu_I/T$ (differentiated by line styles). Figure taken from [50].

minima, one for each *center sector*. The one that will be chosen (the absolute minimum) will depend on μ_I .

Considering the solution $\phi_i/T = \frac{2\pi m}{N}$, the minimum of V_{eff} as a function of μ_I is

$$V_{eff}(\phi_i/T = \frac{2\pi m}{N}) = -\frac{1}{12}\pi^2 T^4 N \left(1 - \frac{(\mu_I - 2\pi m T/N)^2}{\pi^2 T^2}\right)^2, \quad -\pi T < \mu_I < \pi T. \quad (1.27)$$

From Eq.(1.27) it is clear that for

$$\mu_I = \frac{(2m+1)\pi T}{N} \quad (1.28)$$

the “energy” associated to two center sectors is the same, while the derivative of V_{eff} with respect to μ_I has a discontinuity, so we expect a first order transition driven by μ_I , the so called Roberge-Weiss phase transition. For clarity, in Fig.1.3 the effective potential is plotted for the different center sectors.

This analysis extends trivially to the case with N_f different fermions with equal chemical potential μ_q : while the presence of the fermion determinant explicitly breaks center symmetry at zero density, when $\mu_q = i\frac{(2m+1)\pi T}{N}$ there is a residual Z_2 symmetry for two possible values of the Polyakov loop, namely the two elements of the center which are the closest to $e^{i\mu_q/T}$.

The same computation has been also easily extended to the case $\mu_l \neq \mu_s$ (i.e. $\mu_s = 0$) in Section 3.2, showing that in this case the Roberge-Weiss phase transition at extremely high temperature happens at a different value of μ_I ; the lattice data obtained confirm this picture. The most important effect is that the Roberge-Weiss-like transition happens at a larger value of the imaginary chemical potential, and this fact may be relevant for the validity of analytic continuation. In the following parts of Chapter 3 we will only study the case where the chemical potentials for all quarks are purely imaginary and equal to $i\mu_{q,I}$.

In [50] the $T = 0$ case is also studied, making use of the strong coupling expansion of the lattice field theory and of the loop expansion of the fermionic determinant. While the grounds of the computation in this case are less solid, it may be worth noting that these results hint that the expected value of P is a smooth function of μ/T instead, thus suggesting that no transitions take place at low T : this scenario suggests the existence of an endpoint at finite temperature, which is confirmed by lattice studies.

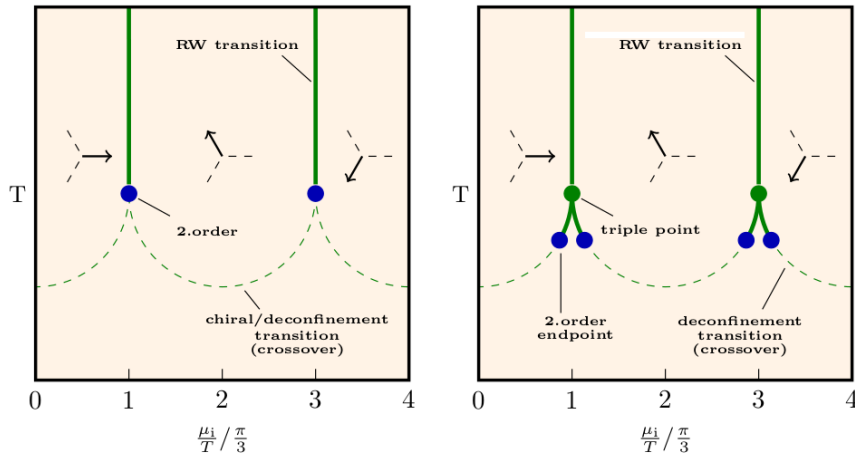


FIGURE 1.4: Depiction of the $T - \mu_l$ phase diagram in the case in which the Roberge-Weiss transition is of the second order kind (left) or of the first order kind (right). Figure taken and modified from [54].

If we look at the Roberge-Weiss transition in the $T - \mu_{q,l}$ phase diagram, a number of questions naturally arise. An important issue is the relation between the Roberge Weiss and the other transitions or crossovers, in particular the relation with the critical line of QCD (the topic of the first part of the present Thesis).

As far as the order of the Roberge-Weiss transition at the endpoint is concerned, we expect it to depend on the quark masses. When the deconfinement/chiral restoration transition is a first order transition for $\mu_l/T \sim \pi/3$, the endpoint of the Roberge-Weiss transition line is actually a triple point, when instead for $\mu_l/T \sim \pi/3$ we have a deconfinement/chiral restoration crossover the Roberge-Weiss transition at the endpoint will be of the second order kind (see Fig. 1.4 for a depiction of the two cases). These two situations are separated by the case where the Roberge-Weiss endpoint is a tricritical point. The general expectation about the order of the deconfinement transition at $\mu_l/T \sim \pi/3$ can be seen from Fig.(1.2, right), on the bottom plane. That figure suggests that in the low-masses corner, in the high-masses corner and in the chiral limit of the $N_f = 2$ case the Roberge-Weiss transition will be first order, while it should be second order for intermediate masses and in the chiral limit of the $N_f = 1$ case.

1.5 General Remarks on the numerical setup

The results of this work have been carried out by making use of an improved action, with the tree-level Symanzik improvement for the gauge part [5, 6] and twice-stout staggered fermions [17]. The partition function reads

$$\mathcal{Z} = \int \mathcal{D}U e^{-S_g^E} \prod_{f=u,d,s} \det \left(M_{\text{st}}^f[U, \mu_{f,l}] \right)^{1/4}. \quad (1.29)$$

For the tree-level Symanzik improved gauge action, we have

$$S_g^E = \sum_{n, \mu \neq \nu} \left(\frac{5}{6} W_{\mu, \nu}^{1 \times 1}(n) - \frac{1}{12} W_{\mu, \nu}^{1 \times 2}(n) \right), \quad (1.30)$$

where the product of 6 links around planar 1×2 rectangles are also taken into account. For the fermionic part, the fermion matrix for a quark f is defined as

$$(M_{\text{st}}^f)_{i,j} = am_f \delta_{i,j} + \sum_{\nu=1}^4 \frac{\eta_{i,\nu}}{2} \left[e^{ia\mu_{f,I}\delta_{\nu,4}} U_{i;\nu}^{(2)} \delta_{i,j-\hat{\nu}} e^{-ia\mu_{f,I}\delta_{\nu,4}} U_{i-\hat{\nu};\nu}^{(2)\dagger} \delta_{i,j+\hat{\nu}} \right]. \quad (1.31)$$

where:

- i, j represent lattice sites;
- $\eta_{i,\nu}$ represent the *staggered phases*:

$$\eta_{i,\nu} = (-1)^{\sum_{\mu=1}^{\nu-1} i_\mu}; \quad (1.32)$$

- $U_{i;\nu}^{(2)}$ represent the twice-stouted gauge links, which are obtained from the standard gauge links (the ones that enter Eq. 1.30) by the stouting procedure. In the isotropic formulation, stouted links are obtained from the original links by moving towards the local minimum of the action, integrating the action gradient on the field manifold in a first-order Euler fashion. The integration step size is proportional to the so-called stout strength ρ , which in our case is set to 0.15 (see [17], Eq. 1). An essential feature of the stout formulation is that the stouted links entering the Dirac operator are an analytic function of the standard links. This allows to compute derivatives of the fermion action with respect to the standard links by making use of the chain rule for differentiation, a task necessary in the molecular dynamics phase of the Montecarlo algorithm. More details on the stouting procedure will be discussed in Appendix A.
- $\mu_{f,I}$ represent the imaginary part of the chemical potential associated to quark f .

1.5.1 Line of Constant physics and scale setting

The action we use has 3 dimensionless parameters: the light quark mass am_l , the strange quark mass am_s , and the inverse square coupling β . In order to study physical QCD, we need to tune the parameters in the theory so that the values of known observables measured on the lattice (which can only be dimensionless quantities) match the physical values. In particular, quark masses must be tuned as a function of β . A part of this procedure is also scale setting, that is the mapping of the lattice spacing a in physical unit as a function of β and the quark masses. Through dimensional analysis, the appropriate powers of the lattice spacing in physical units can be recovered that represent the proportionality factors needed to convert dimensionless lattice measurements into physical values.

Scale setting and quark mass tuning has been done with a variety of techniques in [32, 55, 56, 57]. In particular, and for what concerns our work, in [32, 55] the quark masses are tuned so that the ratios m_K/f_K and m_K/m_π (where m_K and f_K are the mass and the decay constant of the kaon) measured on $T = 0$ lattices are equal to their physical values¹⁰: $f_\pi \simeq 131$ MeV, $m_\pi \simeq 134$ MeV, and $m_K \simeq 498$ MeV. For the general scale setting (the determination of a as a function of β), $f_K \simeq 160$ MeV has been used¹¹. This tuning procedure yields, for the action we use, the values of the light and strange bare quark masses shown in Fig.(1.5, left) as a function of β , which are in a ratio $m_s/m_l \simeq 28.15$. The obtained value of

¹⁰ We here refer to the lightest staggered kaon and the lightest staggered pion.

¹¹ This is the value reported in the 2008 Particle Data Book, which has actually changed by some percent in these years.

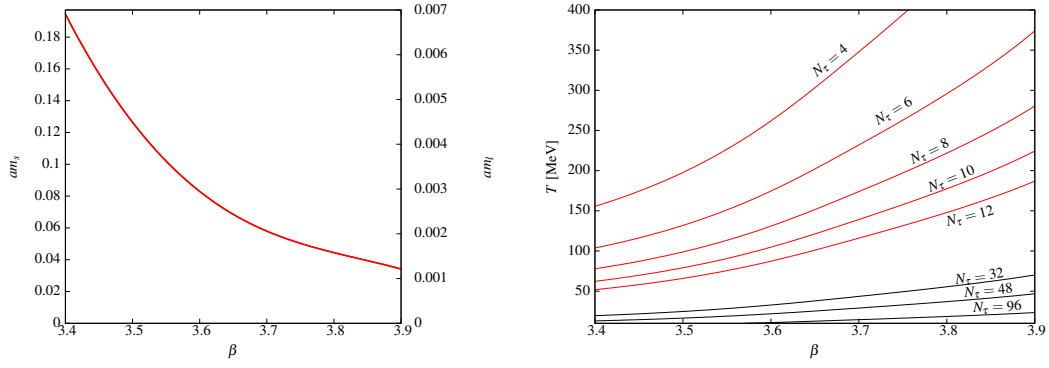


FIGURE 1.5: **Left:** The bare quark masses (strange and light quarks) as a function of the inverse coupling β on the line of constant physics for the action of our choice. **Right:** Value of the temperature $1/(aN_\tau)$ for various choices of the Euclidean time side, as a function of β for the action of our choice. Curves have been obtained with a spline interpolation of data coming from [55] and [56]. Systematic errors deriving from the scale setting procedure are not shown, and are of the order of 2-3%.

the lattice spacing a is related to the temperature by the Euclidean time size of the lattice N_t . In Fig.(1.5, right) the temperature as a function of β is reported for some values of N_t .

Notice that the scale setting procedure has a degree of arbitrariness: for example, it is possible to set the general scale making use of either m_π or m_K , or f_K . These three choices give slightly different results, which deviate less than 2-3% from the average: this can be interpreted as the systematic uncertainty in the determination of the lattice spacing a , which propagates to all dimensionful quantities.

Chapter 2

The critical line of QCD and analytic continuation

2.1 Phenomenology of the QCD phase diagram

The most prominent features of QCD are confinement and chiral symmetry breaking. Confinement, in particular, entails that baryons and mesons are the relevant degrees of freedom at low temperatures. It is expected, because of asymptotic freedom, that at high temperature and/or at high baryon chemical potential strongly interacting matter will turn into a phase where quarks and gluons are the relevant degrees of freedom instead¹.

From the theoretical point of view, the $T - \mu_B$ phase diagram of *QCD* has been studied ab initio on the lattice and with effective models. Amongst the effective models, we cite the Nambu-Jona-Lasinio model [59] (see also [60] for a review), which is an effective model for quarks with four-fermion, nonrenormalizable vertices which respect chiral symmetry (so that the chiral-symmetry breaking effect is in the mass term only). In the original formulation² gluons are absent and there is no confinement. A possible extension of the model is the Polyakov-loop extended NJL model [61, 62, 63], or PNJL, where an external background field A_0 is introduced in the Dirac term to mimic the effect of the gluon fields, plus an effective potential $U(l, \bar{l})$ which is a function of the Polyakov loop l .

Moreover, the field correlator method [64] has been also applied to the study of the Equation of state at $\mu \neq 0$ [65, 66], which is relevant for the interiors of neutron stars (see, e.g., [67]). Unfortunately, a problem with these effective approaches is that, while their predictive power can be tested against results coming from ab-initio computations, it is not clear whether they are a valid substitute for ab-initio methods when the latter fail to give reliable predictions.

The behaviour of strongly interacting matter at finite temperature, *at zero density*, has been widely studied via lattice simulations. The phase diagram can be studied by making use of two orders parameters, namely the Polyakov loop for confinement, and the chiral condensate for the chiral properties.

¹ This does not mean that physics is completely perturbative, as discussed in [58]: perturbation theory breaks down at a certain order g^n (depending on the observable), because all terms with higher order contribute anyway to that order. This is due to the fact that they are infrared divergent, and must be regularized with a cutoff which behaves as g^2 .

² The original formulation [59] dates to well before QCD was conceived, and was initially involving nucleons instead of quarks.

In the physical theory, the mass of the quark is neither infinite, nor zero: this breaks *explicitly* the $SU(3)$ center symmetry and chiral symmetry respectively. This causes both the Polyakov loop and the chiral condensate to be *approximate* order parameters, rather than proper ones. This can be put in relation to the fact that at physical quark masses, both the de-confinement and the chiral “transitions” are smooth crossovers. Of course, this entails that the definition of the critical temperature is, up to a certain level, arbitrary. Modulo these ambiguities, the locations of the two transitions are compatible, being around 155 MeV [32] for the chiral transition. We will refer to both pseudo-transitions as “the crossover” or “the transition”.

The same situation is expected to hold even for finite density, at least at small density. From the lattice, an early work with multi-parameter reweighting but no continuum limit [68] suggested a possible location for a critical endpoint, but on the existence of a critical endpoint there is no general consensus: for example, more recent studies [69, 70] seem to exclude it.

Particularly important is what happens at zero temperature with increasing μ . In particular, density is expected to remain zero until the baryon chemical potential reaches almost the nucleon mass³, where it jumps to the density of nuclear matter. For higher values of the chemical potential, a μ_B -driven deconfinement transition at zero temperature is possible. With an analysis based on renormalization group and universality arguments [71] it has been hinted that, for physical quark masses, it should be of the first order type⁴. At high enough densities and low enough temperatures, nuclear matter should become a color superconductor, in the so-called “color-flavor-locked” phase [72, 73], with a number of possible variants (like the “crystal color superconductor” [74]). This could be mostly relevant for the interior of neutron stars. In Fig.(2.1) a depiction of a possible $\mu_B - T$ phase diagram is shown.

Heavy ion collision experiments can also yield important information about the phase diagram. In the collision, a fireball of quark-gluon plasma is produced. After a thermalization phase, the fireball reaches *local* thermodynamic equilibrium, and expands and cools following a hydrodynamic evolution. When the temperature decreases enough, hadrons and mesons form. At some time after that, the “chemical” nature of the particles stops changing: the corresponding point in the phase diagram is called the “chemical freeze-out point” [75, 76, 77, 78, 79, 80, 81, 82, 83]. In this picture, the chemical freeze-out point is at a temperature which is lower than the confinement (pseudo) transition.

In this scheme, the values of the temperature and the chemical potential at the transition can be obtained by looking at the *chemical composition* of the system. Indeed, in statistical models that assume the thermalization of the quark-gluon plasma, the abundances of the various baryon species are functions of the temperature and the chemical potential [82]. These estimates are also significantly affected by other phenomena, like e.g. pion exchange between already formed hadrons [84].

The collection of the points of chemical freeze-out in the phase diagram is called the freeze-out curve. The collection of $(\mu, T(\mu))$ points at which the QCD crossover happens is called the (pseudo) critical line (it of course depends on the definition of (pseudo-)critical temperature $T_c(\mu)$, which is slightly arbitrary), and from what has just been said, the freeze-out curve should lie below the critical line. Due to the symmetry of QCD under charge conjugation, we expect $T_c(\mu)$ to be even in μ , thus for small μ we can assume

$$\frac{T_c(\mu_B)}{T_c(0)} = 1 - \kappa \left(\frac{\mu_B}{T_c(0)} \right)^2 + \mathcal{O}(\mu_B^4) \quad (2.1)$$

³ That is, the nucleon mass minus the binding energy per nucleon in nuclear matter.

⁴ The method used is to check for the existence of an infrared stable (IRS) fixed point, which is required for the transition to be of the second order kind. Lack of such an IRS fixed point entails a first order transition, with the usual caveats: there might be a nonperturbative IRS fixed point which is not detected by the analysis of the beta function, and away from the fixed point the short range interactions could cause a first order transition.

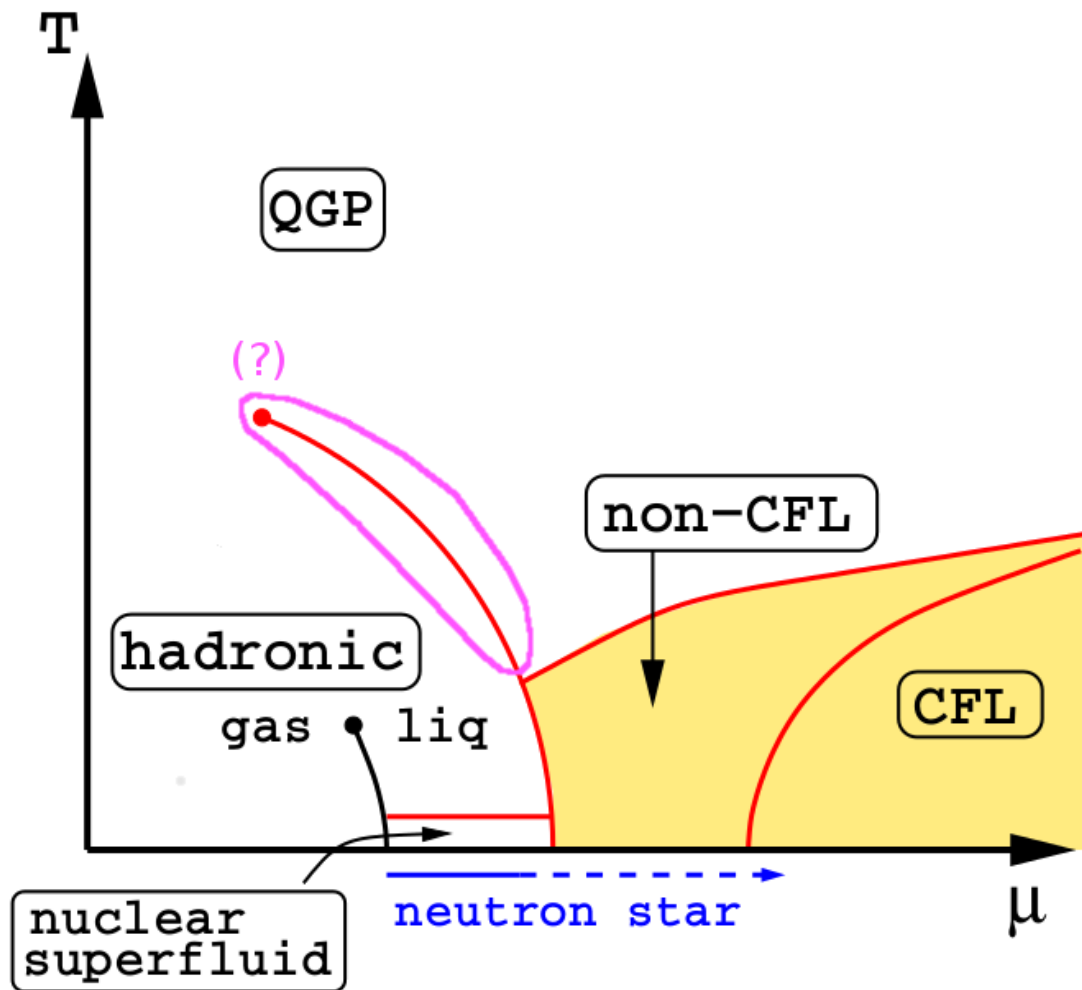


FIGURE 2.1: A possible phase diagram for QCD. In particular, on the existence of the critical point there is still not a general consensus (picture taken and modified from [73]).

where μ_B is the baryon chemical potential and κ is the *curvature of the critical line* of QCD. Our investigation will focus on κ .

2.2 Heavy Ion collision Experiments

In the following, a brief review of Heavy Ion collision physics is presented, loosely based on the introduction given in [85]. The topic is vast and is an active field of research, so the little resume presented here might not be up to date.

2.2.1 Theoretical description of Heavy Ion collision

The commonly accepted description of heavy ion collision processes is usually divided in three phases: a first, pre-thermalization phase, when so-called hard processes occur; a second, locally thermalized phase

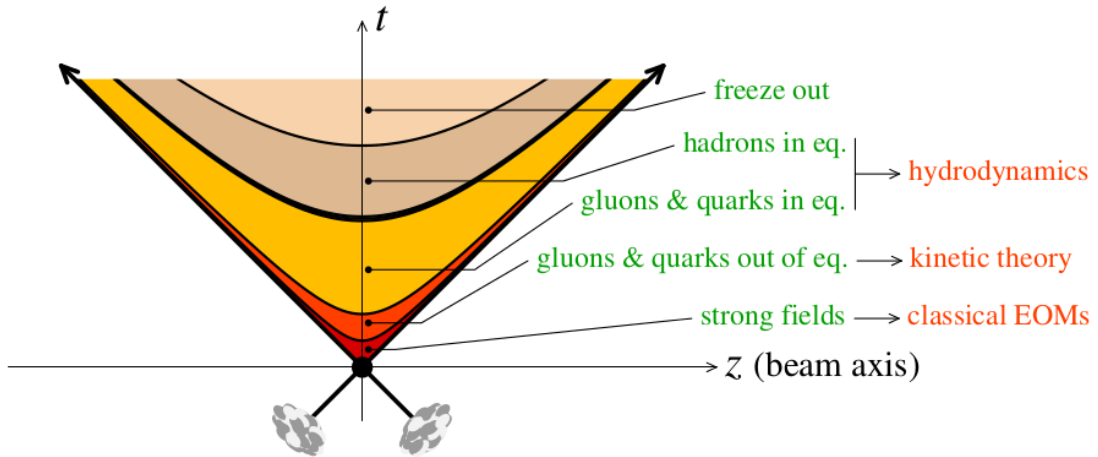


FIGURE 2.2: Stages of a heavy ion collision and a choice of the models used to describe it (Figure from [86]).

which can be described with hydrodynamic models, and a subsequent freeze-out phase, where hadrons are formed and interactions stop. In Fig.(2.2) a depiction of the stages of Heavy Ion Collisions is presented.

The geometric aspects of the impact (e.g. the number of nucleons taking part N_{part} and the impact parameter b , the differential cross section $\partial\sigma/\partial b$ *et cetera*) can be described by making use of Glauber models [87].

The behaviour of the system at the instant of the collision is described in terms of a Color Glass Condensate (CGC). In such situation, it is possible to separate the scales between the fast, high Bjorken- x partons and the slow, small Bjorken- x ones. In a Born-Oppenheimer scale separation scheme, the high x partons can be considered the classical sources of a Yang-Mills field which represents the low x partons⁵. This scheme must be intended as an effective method to explain the dynamics of soft gluons in Deep Inelastic Scattering, justified by the fact that occupation numbers are high (for more details see, e.g., [86, 88]).

The transition from the CGC to the thermalized Quark Gluon Plasma is described in terms of the so called ‘‘Glasma’’ [89], which is still governed by the classical Yang-Mills equation. Numerical studies of ‘‘classical’’ glasma dynamics show that this phase is extremely unstable due to nonlinear interactions and strong event-by-event fluctuations in momentum anisotropy are generated. While quantum fluctuations might be parametrically suppressed, next-to-leading-order effects may actually be crucial for an accurate description of the system.

It is believed that after this phase, the system becomes a quark-gluon plasma that can still be treated classically through relativistic viscous hydrodynamics (see, e.g. [90]). The underlying assumptions that justify the hydrodynamic approach are that the system is at local thermodynamic equilibrium, and that the mean free path is smaller than the size of the system. Very important ingredients entering the hydrodynamic description are, e.g. the Equation of State and the functional dependence of viscosity η on thermodynamic quantities (usually its ratio with entropy density η/s is considered).

When the quark-gluon plasma temperature decreases below a certain point, hadrons are formed. The statistical properties of the hadronization process are usually taken care of making use of the Cooper-Frye

⁵In this case, the high x partons represent the *slow* modes (the atomic nuclei in the original context of the Born-Oppenheimer approximation), while the low x partons represent the *fast* modes (the electrons in the original B.O. scheme).

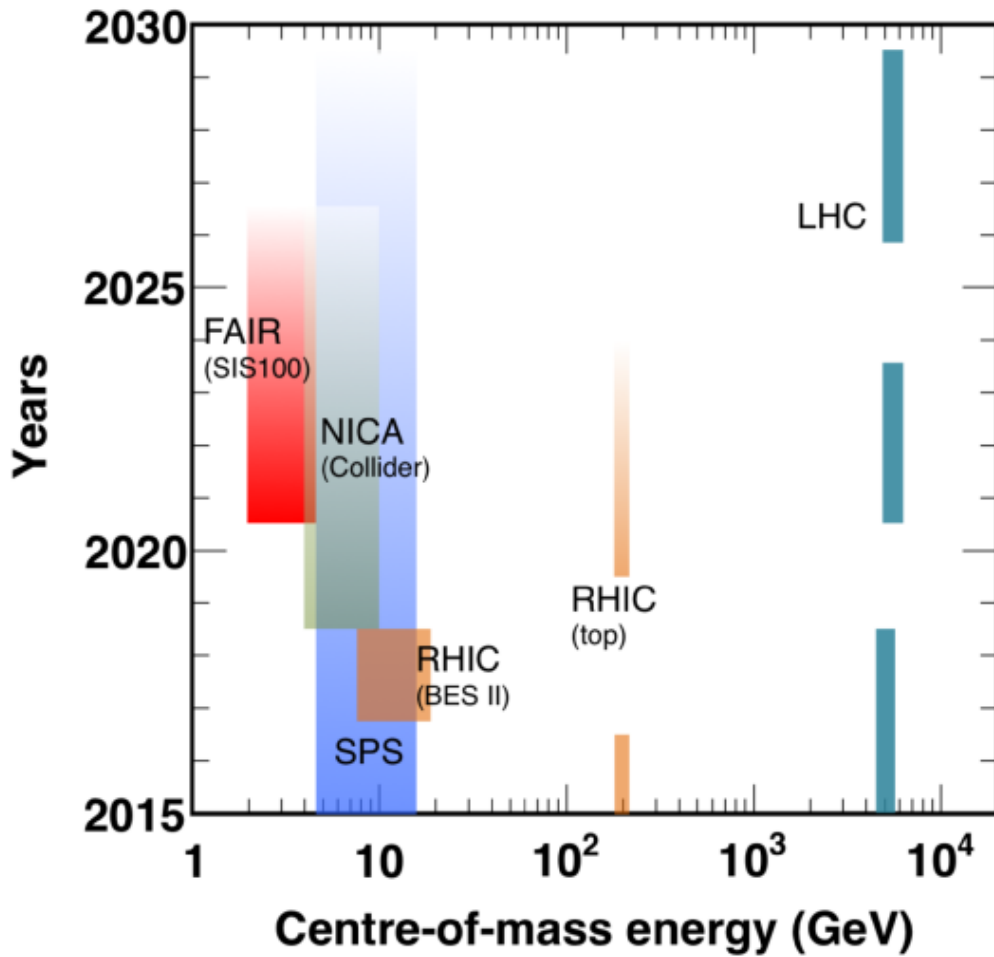


FIGURE 2.3: Center of mass energies and expected run times for heavy Ion collision physics (Figure from [85]).

prescriptions [91]. Following this phase, subsequent hadron-hadron interaction can still significantly modify the hadrochemical compositions of the collision products [84].

Numerical tools have been created to describe the space-time evolution of the system from the beginning of the collision to the eventual hadronization, with different approaches and taking care of the different phases of the collision with different formalisms (e.g. [90, 92]).

2.2.2 Experiments probing the phase diagram of QCD

Heavy ion collision experiments have been performed on various machines, in colliders (RHIC, and LHC at higher center-of-mass energies) and fixed-target configurations (SPS). In general, the higher the \sqrt{s} per nucleon in the collision, the smaller the chemical potential at hadronization. This can be explained by the fact that the higher \sqrt{s} , the more the product of the collision will be spread in rapidity. So, for a given rapidity interval - let's say, at central rapidity - the number of observed particles will decrease as \sqrt{s} increases. For the future, machines with lower \sqrt{s} have been devised in order to better study the high- μ_B regions of the phase diagram (see Fig. 2.3).

There are two classes of possible experimental signatures of the quark gluon plasma [93]: evidences for bulk behaviour in agreement with QGP formation and evidences for changes in the properties of particles traversing it (e.g., heavy quarks, quarkonia systems and jets).

A striking feature of RHIC data were the strong event-by-event anisotropies in momentum distribution. The main effect of these anisotropies is described in terms of the so-called elliptic flow v_2 , which is the first non-constant term in the Fourier expansion of the distribution of produced particles:

$$v_2 = \langle \cos[2(\phi - \psi_{RP})] \rangle , \quad (2.2)$$

where $\phi - \psi_{RP}$ is the angle between the impulse of the particle and the reaction plane defined by the impact parameter and the beam direction. Higher harmonics have also been measured, and compared with hydrodynamics simulations with different level of success[92]. The explanation for a nonzero v_2 is natural in an hydrodynamic description of the system: the elongated shape of the overlap region of the two nuclei in a non-central collision causes a larger pressure gradient along the reaction plane, which consequently causes a stronger flow in this direction [94]. This is usually seen as the most important experimental evidence of a thermalized quark gluon plasma.

Another class of observables in heavy ion collisions is related to the so-called hard probes, consisting of quarkonium systems and “open heavy flavor” [95]. Due to their mass, these particles can be produced only at the early stages of the collision, and propagate in the medium which evolves thereafter; this dynamics is usually described with transport calculations based on the Boltzmann equation. A possible sign for the onset of deconfinement is the suppression of charmonium [96]: in the plasma, color screening prevents the binding of the $\bar{q}q$ pairs, when the Debye mass (which is approximately proportional to T) is larger than the inverse of typical radius of the $\bar{q}q$ system. Experimentally, suppression is quantified with R_{AA} , the ratio between the measured yield in nucleus-nucleus collision and the yield in proton-proton collision multiplied by the number of expected nucleon-nucleon collisions in the nucleus-nucleus collision. The situation is more complicated than imagined at first, because there can be also mechanisms which regenerate charmonium, like $\bar{q}q$ recombination (an effect that grows with energy), as well as other mechanisms that suppress it (e.g. cold nuclear matter [CNM] effects, like nuclear absorption). The dynamics seem to be cleaner for bottomonium systems, whose signal should be less affected by these phenomena. At LHC, given the increase in collision energy, it was finally possible to study these observables.

Also, jets can be considered hard probes. A suppression of jets (called *jet quenching*) was expected and has as well been observed, in agreement with some theoretical estimates [85]. Other information comes also from photon and dilepton production (at the beginning of the collision, or thermally, in the QGP).

Heavy ion collisions can also provide data more specifically on the transition between QGP and hadronic matter, through *hadrochemistry* studies. Assuming hadrochemical equilibrium at hadronization, it is possible to calculate the statistical abundances of different hadron species as a function of, e.g., T and μ_B . Conversely, from hadron abundances it is possible to estimate T and μ_B at the point of chemical freeze-out [82]. The subsequent interactions between hadrons can, however, have a significant impact on the results and must be taken into account [84].

2.3 Lattice QCD and Analytic Continuation

As already discussed, a direct lattice determination of T_c at $\mu_B \neq 0$ is presently hindered by the well known sign problem, but various methods have been proposed so far to partially circumvent it and to obtain reliable results in the regime of small μ_B . A natural parametrization of $T_c(\mu_B)$ for small chemical potentials, which exploits the symmetry under charge conjugation at $\mu_B = 0$ and assumes analyticity around this point is ⁶

$$\frac{T_c(\mu_B)}{T_c} = 1 - \kappa \left(\frac{\mu_B}{T_c} \right)^2 + O(\mu_B^4), \quad (2.3)$$

where the coefficient κ defines the curvature of the pseudo-critical line $T_c(\mu_B)$. The curvature can be obtained in lattice QCD simulations in various ways.

In the so-called Taylor expansion method [69, 97, 98, 99, 100]) it is recovered by suitable combinations of expectation values computed at $\mu_B = 0$. Another option is determining the pseudo-critical line for purely imaginary values of μ_B , for which numerical simulations are feasible since the sign problem is absent, then fixing the behavior for small and real μ_B by analytic continuation⁷. Reweighting techniques have also been used, in which the oscillating complex behavior is shifted from the path integral measure to the physical observables [68, 116], and also approaches via a reconstruction of the canonical partition function [117, 118].

A natural candidate for a comparison with QCD predictions is the chemical freeze-out curve in the $T - \mu_B$ plane, determined by heavy ion collision experiments, which is obtained so as to describe the particle multiplicities according to a thermal-statistical model (see Section 2.2 for context). In general, one can only assume that chemical freeze-out takes place after re-hadronization, i.e. that the freeze-out curve lies below the pseudo-critical line in the $T - \mu_B$ plane. However, as a working hypothesis it is also reasonable to assume that chemical freeze-out is reached shortly after re-hadronization, so that the two lines may lie close to each other. Actually, a comparison with early lattice determinations of $T_c(\mu_B)$ does not show a good agreement. In particular, most early lattice determinations of κ turn out to be a factor 2-3 smaller than the corresponding curvature of the freeze-out curve [82], even if a recent reanalysis of experimental data, which takes into account inelastic collisions after freeze-out, seems to bring to a significant reduction of such a discrepancy [84].

On the side of lattice QCD simulations, a complete control over all possible systematics is also desirable. That requires a proper continuum extrapolation and a comparison among different methods adopted to partially overcome the sign problem. Most determinations available at or around the physical point (i.e. by adopting quark masses tuned so as to yield a physical hadron spectrum) have been obtained by the Taylor expansion method, see Ref. [98] (p4-improved action for staggered quarks) and Refs. [69, 99] (stout-smearred improved action for staggered quarks). A recent determination [113, 115], obtained by the method of analytic continuation and adopting a HISQ/tree action discretization of $N_f = 2 + 1$ QCD, has provided a value of the curvature which is somewhat larger with respect to previous lattice determinations.

Apart from possible systematics lying behind either the Taylor expansion method or analytic continuation, one should consider other standard sources of systematic errors, among which the different possible definitions of T_c , the approach to the thermodynamical limit (finite size effects), to the continuum limit and to the physical point, and the different setup of chemical potentials, μ_u , μ_d and μ_s , coupled respectively

⁶We note that a possible ambiguity in the denominator of the quadratic term, i.e. whether we take $\mu_B/T_c(\mu_B)$ or $\mu_B/T_c(0)$ as an expansion variable, is irrelevant as long as just the quadratic term is considered, since it only affects higher order terms.

⁷As a possible list of references see, e.g., [101, 102, 103, 104, 105, 106, 107, 108, 109, 110, 111, 112, 113, 114, 115].

to the up, down and strange quark numbers. For instance, the choice in Ref. [113] has been to fix them to equal values ($\mu_u = \mu_d = \mu_s = \mu_B/3$), while in previous determinations the choice has typically been $\mu_u = \mu_d = \mu_B/3$ and $\mu_s = 0$, which is thought to better reproduce the thermal medium in accordance with the initial conditions of heavy ion collisions, which correspond to strangeness neutrality⁸.

In this work we have considered both the case $\mu_s = 0$ and $\mu_s \neq 0$ and have monitored two different physical quantities, namely the renormalized chiral condensate and its susceptibility, in order to locate the pseudo-critical temperature for different values of the chemical potentials.

Various purposes have been accomplished in this way:

1. we compared determinations of the curvature obtained by different methods but with the same lattice discretization [69];
2. we compared determinations of the curvature obtained by the same method (analytic continuation) but with different discretizations [113, 115] (HISQ vs stout smeared staggered quarks)⁹;
3. we studied the effects on the critical line of the inclusion of a strange quark chemical potential. In fact, the setup with $\mu_s = \mu_l$ is the same studied in [113, 115];
4. making use of the data from lattices with aspect ratio $N_s/N_t = 4$, we obtained a continuum extrapolated value of κ , using two different procedures in order to assess the systematic uncertainties in the continuum extrapolation procedure. As a byproduct of this analysis, the strength of the transition as a function of μ_B can also be assessed: this information is relevant to the possible existence of a critical endpoint in the $T - \mu_B$ plane.

The following sections are organized as follows: in Section 2.4 we elaborate on the relations between the chemical potentials, describe the observables chosen to locate T_c and their renormalization; in Section 2.5 we describe the method of analytic continuation, with a focus on the possible differences related to the inclusion (or non inclusion) of a strange chemical potential μ_s , which stem from differences in the corresponding phase diagrams at imaginary chemical potentials. In Section 2.6 we present our numerical results, which are compared to previous determinations in Section 2.8, where we also briefly review different methods to determine κ adopted in the literature. Finally, in Section 2.9, we draw our conclusions for this part of the Thesis.

2.4 Numerical setup and observables

Using the action described in Section 1.5, we performed simulations at finite temperature around the transition temperature, using lattices with temporal extensions $N_t = 6, 8, 10$ and 12. At fixed N_t , the temperature $T = 1/(aN_t)$ of the system was changed by varying the value of the bare coupling constant β . The bare quark masses m_s and m_l were accordingly rescaled with β , in order to move on a line of constant physics, with $m_\pi \simeq 135$ MeV and $m_s/m_l = 28.15$; this line is determined by a spline interpolation of the values reported in Refs. [55, 57].

⁸ The issue of strangeness neutrality is actually more complex and has been investigated in [114].

⁹ At the time of writing the present Thesis, a work using the same lattice action was published with results compatible with the ones obtained here [114].

2.4.1 Setup of chemical potentials

For $N_f = 2 + 1$ QCD one can consider, in general, three independent chemical potentials, μ_u, μ_d and μ_s , coupled respectively to N_u, N_d and N_s , i.e. the number of up, down and strange quarks. Different conventions can be adopted: for instance it is usual to make reference to the conserved charges B, Q and S (baryon number, electric charge and strangeness) and to the chemical potentials coupled to them, μ_B, μ_Q and μ_S . The conserved charges are related to the quark numbers by the well known relations

$$\begin{aligned} B &= (N_u + N_d + N_s)/3 \\ Q &= (2N_u - N_d - N_s)/3 \\ S &= -N_s \end{aligned} \tag{2.4}$$

from which the equalities involving the chemical potentials can be deduced

$$\begin{aligned} \mu_u &= \mu_B/3 + 2\mu_Q/3 \\ \mu_d &= \mu_B/3 - \mu_Q/3 \\ \mu_s &= \mu_B/3 - \mu_Q/3 - \mu_S. \end{aligned} \tag{2.5}$$

In the following we make reference to the convention in terms of μ_u, μ_d and μ_s , and translate to the other convention when necessary (e.g., to extract κ given in Eq. (2.3)). The lattice action used and the details have been described in 1.5.

The purpose of our study is to determine the dependence of the pseudocritical temperature T_c on the baryon chemical potential (which is given by $\mu_B = \mu_u + 2\mu_d$), in a setup of chemical potentials which is as close as possible to the thermal equilibrium conditions created in heavy ion collisions. We thus have to require to $S = 0$ and $Q = rB$, where r is the number of protons divided by the number of nucleons of the colliding ions, $r \equiv Z/A \approx 0.4$ typically.

These requirements can be translated into relations between μ_B, μ_S and μ_Q , which at the lowest order in μ_B read $\mu_Q \simeq q_1(T)\mu_B$ and $\mu_S \simeq s_1(T)\mu_B$, the coefficients $q_1(T)$ and $s_1(T)$ being related to derivatives of the free energy density [119, 120]. Let us consider as an example the strangeness neutrality condition: in a gas of non-interacting fermions it would imply $\mu_s = 0$ but in QCD, due to interactions, the mixed derivatives of the free energy density with respect to μ_s and μ_u, μ_d are non-vanishing, so that one needs a non-zero μ_s to ensure $S = 0$. Early lattice investigations [119, 120] showed that, for $T \sim 155$ MeV, the constraints on charge and strangeness imply $s_1 \simeq 0.25$ and $q_1 \simeq -0.025$. With a precision of a few percent, around the transition at vanishing density, we thus have $\mu_l \equiv \mu_u = \mu_d$, $\mu_l \simeq \mu_B/3$ and $\mu_s \simeq \mu_l/4$.

At the time of writing of this Thesis, a more recent investigation of the issue of strangeness neutrality has appeared [114], which is in good agreement with earlier results, especially for small baryon chemical potential (see Figure 2.4).

Our determination of the curvature κ has been obtained setting $\mu_s = 0$, which is close to the conditions described above. To quantify the impact of μ_s we have considered also the case $\mu_s = \mu_l$, in order to obtain an estimate about the effect of a non-zero μ_s in a range which covers the equilibrium conditions created in heavy ion collisions.

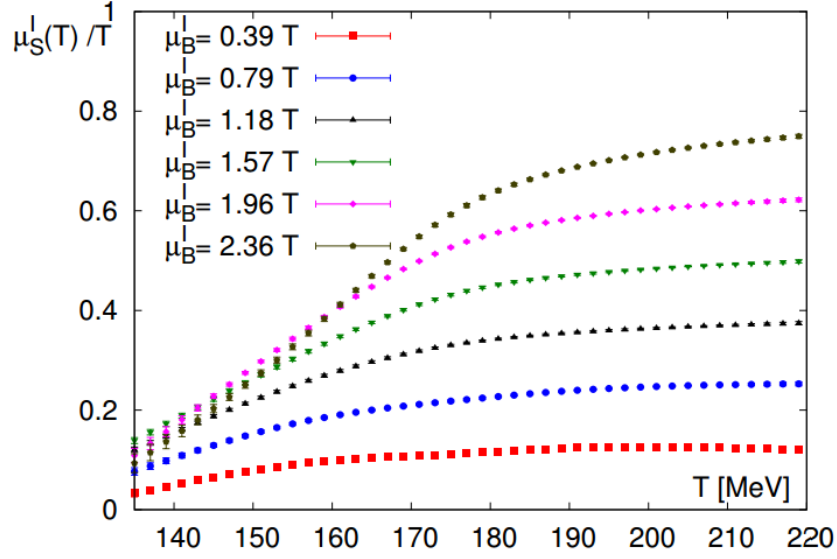


FIGURE 2.4: The value of the imaginary strangeness chemical potential μ_S^I that realizes strangeness neutrality, as a function of T and the baryon chemical potential μ_B . Figure from [114].

2.4.2 Observables on the Lattice, Renormalization and location of $T_c(\mu_B)$

In the absence of a true phase transition, the determination of the pseudo-critical line may depend on the physical observable chosen to locate it. On the other hand, chiral symmetry restoration is the leading phenomenon around T_c , with the light chiral condensate becoming an exact order parameter in limit of zero light quark masses. Therefore in the following $T_c(\mu_B)$ will be determined by monitoring the chiral properties of the system.

The chiral condensate of the flavor f is defined as

$$\langle \bar{\psi}\psi \rangle_f = \frac{T}{V} \frac{\partial \log Z}{\partial m_f}, \quad (2.6)$$

where V is the spatial volume. Since in our simulations the two light quarks are degenerate with mass $m_l \equiv m_u = m_d$, it is convenient to introduce the light quark condensate:

$$\langle \bar{\psi}\psi \rangle_l = \frac{T}{V} \frac{\partial \log Z}{\partial m_l} = \langle \bar{u}u \rangle + \langle \bar{d}d \rangle, \quad (2.7)$$

which will be renormalized by adopting the prescription introduced in Ref. [121]:

$$\langle \bar{\psi}\psi \rangle_l^r(T) \equiv \frac{\left[\langle \bar{\psi}\psi \rangle_l - \frac{2m_l}{m_s} \langle \bar{s}s \rangle \right](T)}{\left[\langle \bar{\psi}\psi \rangle_l - \frac{2m_l}{m_s} \langle \bar{s}s \rangle \right](T=0)}, \quad (2.8)$$

where m_s is the bare strange quark mass.

The light quarks chiral susceptibility is given by (M_l is the Dirac operator corresponding to a single light flavor)

$$\chi_{\bar{\psi}\psi} = \frac{\partial \langle \bar{\psi}\psi \rangle_l}{\partial m_l} = \chi_{\bar{\psi}\psi}^{disc} + \chi_{\bar{\psi}\psi}^{conn} \quad (2.9)$$

$$\chi_{\bar{\psi}\psi}^{disc} \equiv \frac{T}{V} \left(\frac{N_l}{4} \right)^2 [\langle (\text{Tr } M_l^{-1})^2 \rangle - \langle \text{Tr } M_l^{-1} \rangle^2] \quad (2.10)$$

$$\chi_{\bar{\psi}\psi}^{conn} \equiv -\frac{T}{V} \frac{N_l}{4} \langle \text{Tr } M_l^{-2} \rangle. \quad (2.11)$$

In this expression N_l is the number of degenerate light quarks, that in our case is fixed to $N_l = 2$. Traces are computed by noisy estimators, with 8 random vectors for each flavor. The renormalization of the chiral susceptibility is performed by first subtracting the $T = 0$ contribution (thus removing the additive renormalization) and then multiplying the result by the square of the bare light quark mass to fix the multiplicative UV divergence [55]:

$$\chi_{\bar{\psi}\psi}^r = m_l^2 [\chi_{\bar{\psi}\psi}(T) - \chi_{\bar{\psi}\psi}(T=0)]. \quad (2.12)$$

All the $T = 0$ quantities have been measured on a symmetric $N_t = N_s = 32$ lattice or on a $N_t = N_s = 48$ (see Section 2.7).

The renormalization prescriptions Eqs. (2.8)-(2.12) are not the only available choices: other approaches exist in the literature (see e.g. Refs. [69, 98]) and in the following sections we will also investigate the dependence of the results on the different renormalization prescriptions adopted. As an alternative, we consider the following prescription [69]

$$\langle \bar{\psi}\psi \rangle_{(2)}^r = \frac{m_l}{m_\pi^4} (\langle \bar{\psi}\psi \rangle_l - \langle \bar{\psi}\psi \rangle_l(T=0)). \quad (2.13)$$

In this case the zero T subtraction eliminates additive divergences while multiplication by the bare quark mass m_l takes care of multiplicative ones.

2.5 Analytic continuation with and without a strange quark chemical potential

Both the method of analytic continuation from imaginary chemical potentials and the Taylor expansion approach are based on the assumption that the free energy is analytic, at least in a limited region of small chemical potentials.

As it happens for other thermodynamical quantities, it is possible to make an ansatz for the dependence of the pseudo-critical temperature $T_c(\mu_u, \mu_d, \mu_s)$ which is valid for small chemical potentials. The symmetries of the theory constrain the possible form of this dependence. First of all, charge conjugation symmetry imposes that T_c , as well as the free energy itself, be invariant under a simultaneous sign change of all chemical potentials, thus a Taylor expansion of T_c must include only monomials of overall even degree in the chemical potentials.

Moreover, in the case of two degenerate flavors, isospin symmetry imposes further constraints. By rewriting the coupling to the chemical potentials of the continuum Lagrangian in the more compact

form $\bar{\psi}_f \gamma_0 M_{ff'} \psi_{f'}$, where f, f' are flavor indices and M is a 2×2 hermitian matrix, which is usually diagonal (that is, $M = \text{diag}[\mu_u, \mu_d]$), it can be shown that the theory is invariant under isospin rotations $\psi \rightarrow R\psi$, combined with $M \rightarrow RMR^\dagger$, where R denotes a generic $SU(2)$ matrix. The dependence of T_c on the chemical potentials must satisfy such invariance, that means that it can be function only of invariant quantities of the matrix M . At the leading quadratic order two independent such quantities exist, which can be chosen to be $\det(M)$ and $\text{Tr}(M^\dagger M)$ (or alternatively $[\text{Tr}(M)]^2$). To leading order we thus have (see also Ref. [122]):

$$\begin{aligned} T_c(M) &= T_c(M=0) - \alpha \text{Tr}(M^\dagger M) - \gamma \det(M) = \\ &= T_c(M=0) - \alpha(\mu_u^2 + \mu_d^2) - \gamma \mu_u \mu_d, \end{aligned} \quad (2.14)$$

where μ_u and μ_d represent the two eigenvalues of M . It is interesting that at this level the requirement of isospin invariance is in fact equivalent to the requirement of symmetry under $u \leftrightarrow d$ exchange. This is particularly relevant since in the lattice discretization of the partition function, Eq. (1.29), each quark is treated by means of a separate quartic root of a fermion determinant, so that only the symmetry under $u \leftrightarrow d$ exchange is strictly true at finite lattice spacing. It has been verified in Ref. [111] that, in the discretized $N_f = 2$ theory, the mixing term γ is small but non-zero, corresponding to a measurable difference between the curvature in terms of the baryon or the isospin chemical potential. In our $N_f = 2 + 1$ setup, the generalization of Eq. (2.14) is simply

$$\begin{aligned} T_c(\mu_u, \mu_d, \mu_s) &= T_c(0) - A(\mu_u^2 + \mu_d^2) - B\mu_s^2 \\ &- C\mu_u \mu_d - D\mu_s(\mu_u + \mu_d) + O(\mu^4). \end{aligned} \quad (2.15)$$

In this study, we are interested only in two particular setups of chemical potentials. In the first case we set $\mu_u = \mu_d \equiv \mu_l$ and $\mu_s = 0$. That coincides with the setup adopted in most studies (like e.g. in Refs. [69, 98]), which is thought to be close to the situation created in heavy ion collisions, where the initial conditions correspond to strangeness neutrality. In this case the expected parametrization is

$$T_c(\mu_l) = T_c(0) - A'\mu_l^2 + O(\mu_l^4) \quad (2.16)$$

where $A' = 2A + C$.

In the second case, we set $\mu_s = \mu_l$: that permits to estimate the effects of the inclusion of μ_s and to compare with some previous studies [112, 113]. In this case the parametrization is

$$T_c(\mu_l) = T_c(0) - (A' + B')\mu_l^2 + O(\mu_l^4) \quad (2.17)$$

where $B' = B + 2D$. An independent study with $\mu_u = \mu_d = 0$ and $\mu_s \neq 0$ would provide direct information on B and verify if the mixing term D is negligible or not: this is left for future investigations.

When the chemical potentials are purely imaginary, and if analytic continuation holds true, the following dependence is expected for T_c as a function of the quantity $\theta_l = \text{Im}(\mu_l)/T$ introduced in Section 3.3:

$$\frac{T_c(\theta_l)}{T_c(0)} = 1 + R\theta_l^2 + O(\theta_l^4) \quad (2.18)$$

where $R = A' T_c(0)$ or $R = (A' + B') T_c(0)$, depending on the different setup adopted.

Apart from the possible different values of the curvatures, the fact that $\mu_s = 0$ or $\mu_s = \mu_l$ is of course relevant also to non-linear terms in θ_l^2 , as we are going to discuss in the rest of this section. In this

respect, a substantial difference in the phase diagram in the $T - \theta_l$ plane may play a significant role. It is well known [50] that when all imaginary chemical potentials are equal, i.e. when the temporal boundary conditions of all quark fields are rotated by the same angle θ_l , a translation of θ_l by a multiple of $2\pi/3$ can be canceled by a center transformation of gauge fields, so that the partition function is periodic in θ_l with a period $2\pi/3$. Such a periodicity is smoothly realized at low T [101, 102, 103, 104, 123], while in the high T regime it is enforced by first order transitions [50], known as Roberge-Weiss (RW) transitions, which are connected with center symmetry and with the dynamics of the Polyakov loop, as explained in more details in Chapter 1.

One important consequence of the analysis that will be exposed in Section 3.2 is that, for high T , the region available for analytic continuation is larger for $\mu_s = 0$ than for $\mu_s = \mu_l$: that means that a better control on systematic effects can be attained. Since analytic continuation is actually performed in terms of θ_l^2 , going from $\pi/3$ to approximately 0.45π means that the available region is almost doubled, i.e. the increase is substantial. Moreover, one may expect that for $\mu_s = 0$ the possible effects of the critical behavior around the RW endpoint on the region of small chemical potentials should be milder, since the endpoint is moved further inside the $T - \theta_l$ plane: such effects include the possible non-linear contributions in θ_l^2 to the pseudo-critical line $T_c(\theta_l)$. This point will be discussed further in Section 2.6.4.

2.6 Numerical Results

We performed simulations for different values of the chemical potentials and $\mathcal{O}(10)$ temperatures around $T_c(\mu)$, on different lattice sizes, with N_t going from 6 to 12. We used $N_t = 6$ lattices with different spatial size N_s to study finite size effects ($16^3 \times 6$, $24^3 \times 6$ and $32^3 \times 6$). While we mainly considered the $\mu_s = 0$ setup, for the $32^3 \times 8$ lattice we also studied the case $\mu_s = \mu_l$. We have also performed simulations on lattices with $N_t = 10$ and 12 and different choices of T and of the chemical potentials, which have been used with the data from $N_t = 6, 8$ to perform the continuum extrapolation. To that purpose, we have considered only lattices with fixed aspect ratio $N_s/N_t = 4$. As shown in the following, that guarantees the absence of significant finite size effects.

Four different values of chemical potentials have been considered for $N_t = 10$ and 12, corresponding to $\mu_s = 0$ and $\text{Im}(\mu_l)/(\pi T) = 0, 0.20, 0.24$ and 0.275 (the same values but 0.20 have been considered for $N_t = 6$). These values have been chosen in order so that the expected value of $T_c(\mu)$ would be significantly different from $T_c(0)$, while at the same time staying sufficiently far from the non-analiticities related to the ‘‘Roberge-Weiss-like’’ transition which, in the $\mu_s = 0$ setup, happens for $\mu_l/(\pi T) \sim 0.45$ (see Section 3.2). However, in order to provide more information about systematics related to the choice of μ_s/μ_l and to the truncation of the Taylor expansion in Eq. (2.18), a larger set of temperatures and chemical potentials has been considered for $N_t = 8$, in which case we performed simulations also at $\mu_s \neq 0$.

The Rational Hybrid Monte-Carlo algorithm [124, 125, 126] has been used for sampling gauge configurations according to Eq. (1.29), each single run consisting of 2-5 K trajectories of unit length in molecular dynamics time, with higher statistics around the transition.

To perform the renormalization described in Sec. 3.3, one needs to compute observables also at $T = 0$ and at the same values of the bare parameters, i.e. at the same UV cutoff. At $T = 0$ observables depend smoothly on β ; moreover no dependence at all is expected on the imaginary chemical potentials, since they can be viewed as a modification in the temporal boundary conditions which, at $T = 0$ (hence for ideally infinite temporal extension), are completely irrelevant. For those reasons, we performed a set of simulations on a 32^4 lattice and on a 48^4 lattice, at zero chemical potentials and for a few values of

β on the line of constant physics. Then we estimated the observables at intermediate values of β by a suitable interpolation and adopted them to renormalize data at $T \neq 0$ and generic values of the chemical potentials. More details on the $T = 0$ measurements are reported in Section 2.7.

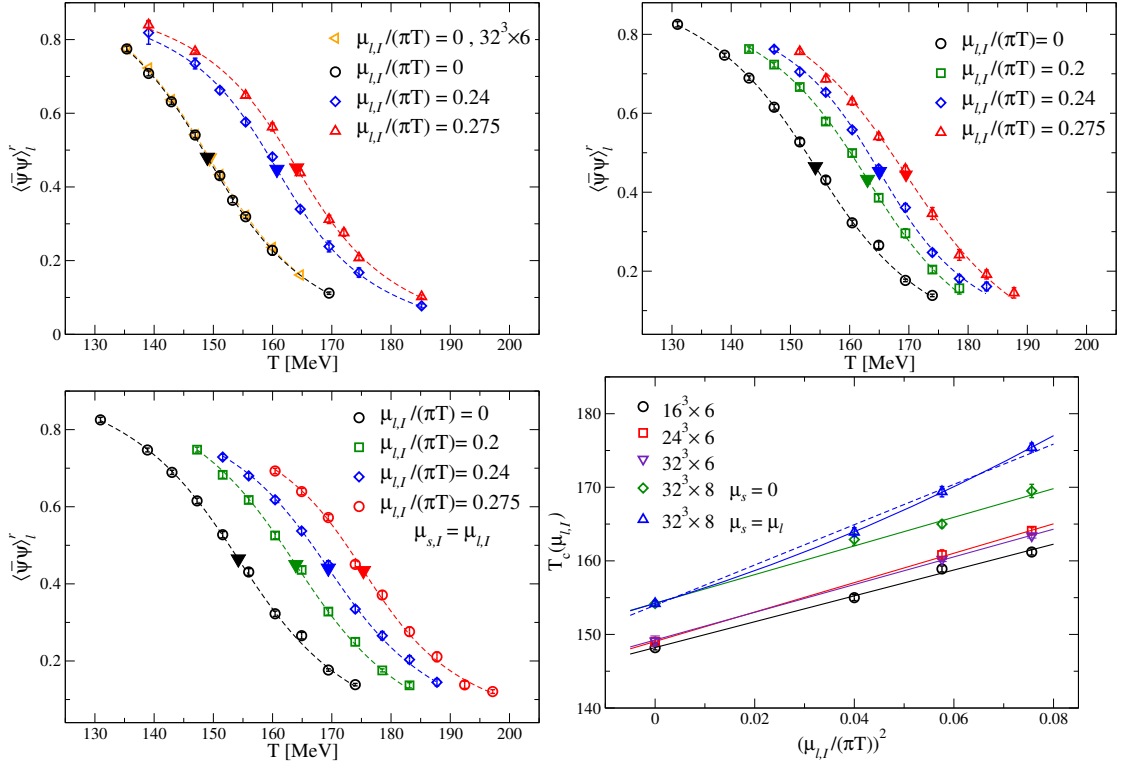


FIGURE 2.5: Renormalized light chiral condensate for various values of T and μ_l respectively on: $24^3 \times 6$ lattice with $\mu_s = 0$ (top left); $32^3 \times 8$ lattice with $\mu_s = 0$ (top right); $32^3 \times 8$ lattice with $\mu_s = \mu_l$ (bottom left). In the top figure the data from the $32^3 \times 6$ lattice at $\mu_l = 0$ are also shown for comparison. Lines correspond to the best fit described in the text and the filled triangles denote the values at the pseudo-critical temperature. Bottom Right: determinations of T_c obtained from the renormalized chiral condensate $\langle \bar{\psi}\psi \rangle_l^r$, for various values of the chemical potential and lattice sizes. The lines correspond to quadratic and quartic fits in $\mu_{l,I}$, as discussed in the text. Fit results are reported in Table 2.1.

In Figs. 2.5 and 2.6 we plot the results obtained respectively for the renormalized light chiral condensate $\langle \bar{\psi}\psi \rangle_l^r$ and for the renormalized chiral susceptibility $\chi_{\bar{\psi}\psi}^r$, which are our reference observables and have been defined in Eqs. (2.8)-(2.12). Since no real phase transition is present in the explored range of chemical potentials, before going on we have to define a prescription to locate the pseudo-critical temperature T_c (a comparison with the results obtained by other definitions and/or approaches is reported in the next section). We will adopt the two following definitions of T_c , related to the two different observables studied:

1. the temperature corresponding to the inflection point of the renormalized chiral condensate (as defined by Eq. (2.8)) ;
2. the temperature corresponding to the maximum of the renormalized chiral susceptibility (as defined by Eq. (2.12)).

Both these definitions are faithful, *i.e.* when a real phase transition is present its location is correctly identified (in the thermodynamical limit) by means of them.

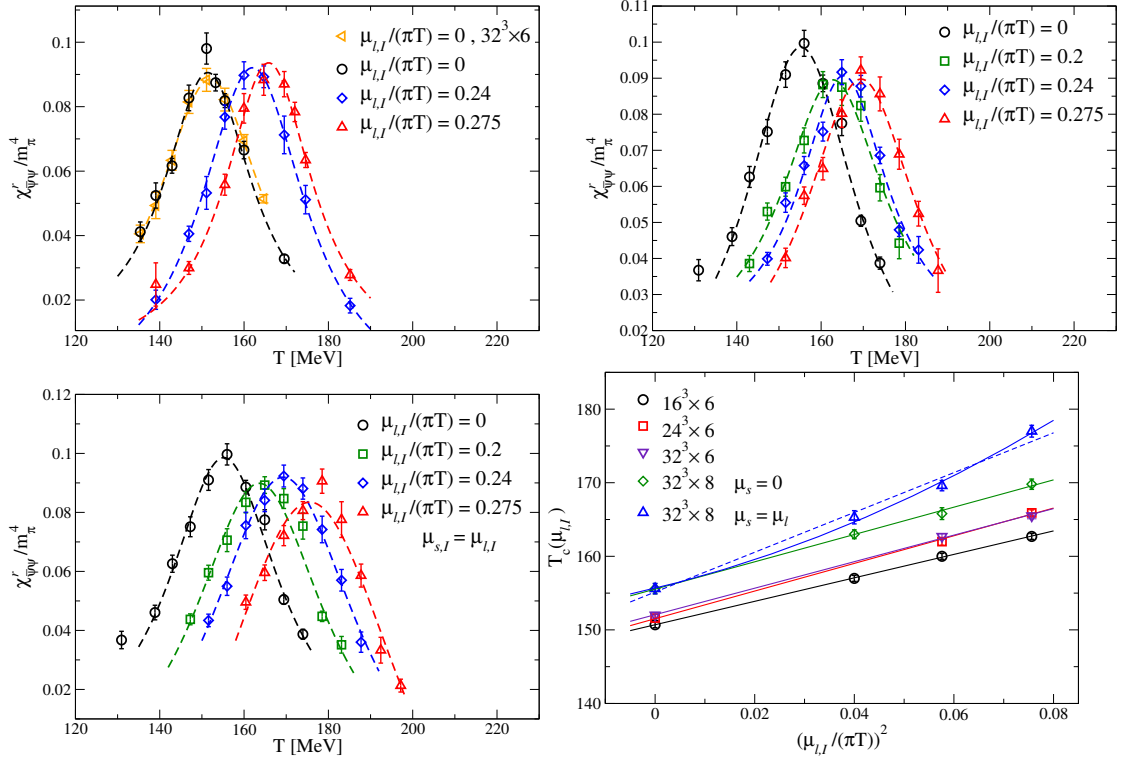


FIGURE 2.6: Renormalized light chiral susceptibility, divided by m_π^4 , for various values of T and μ_l respectively on: $24^3 \times 6$ lattice with $\mu_s = 0$ (top left); $32^3 \times 8$ lattice with $\mu_s = 0$ (top right); $32^3 \times 8$ lattice with $\mu_s = \mu_l$ (bottom left). In the top figure the data from the $32^3 \times 6$ lattice at $\mu_l = 0$ are also shown for comparison. Bottom right: determinations of T_c obtained from the renormalized chiral susceptibility $\chi_{\psi\psi}^r$, for various values of the chemical potential and lattice sizes. The lines correspond to quadratic and quartic fits in $\mu_{l,I}$, as discussed in the text. Fit results are reported in Table 2.2.

In order to determine the inflection point of the renormalized chiral condensate, we performed a best fit on the data by using the expression

$$\langle \bar{\psi}\psi \rangle_l^r(T) = A_1 + B_1 \arctan(C_1(T - T_c)), \quad (2.19)$$

with the four independent parameters A_1 , B_1 , C_1 and T_c . This function is found to well describe the behavior of $\langle \bar{\psi}\psi \rangle_l^r(T)$ in the whole range of explored temperatures. The best fits obtained by this procedure are plotted, together with the corresponding data points, in Fig. 2.5, the position of the inflection point being denoted, for each data set, by a filled triangle. The errors on the fit parameters have been estimated by means of a bootstrap analysis; results for T_c are stable, within the quoted errors, if a different interpolation (e.g., through an hyperbolic tangent) is adopted to locate the inflection point.

In the case of the renormalized chiral susceptibility, a reasonable description of the data around the peak location is provided by a Lorentzian function

$$\chi_{\psi\psi}^r = \frac{A_2}{B_2^2 + (T - T_c)^2}. \quad (2.20)$$

In both cases, statistical errors on the fitted parameters have been estimated by means of a bootstrap analysis, while systematic uncertainties have been estimated either by varying the range of fitted points around T_c or by choosing an alternative fitting function (e.g., a hyperbolic tangent for the condensate or

a parabola for its susceptibility). Statistical and systematic¹⁰ errors are both included in the collection of determinations of T_c for the various combinations of lattice sizes and chemical potentials in Table 2.6,

In Fig. 2.6 we report numerical data for the dimensionless ratio $\chi_{\bar{\psi}\psi}^r/m_\pi^4$ as a function of T , together with some of the fits performed¹¹.

The full set of determinations of $T_c(\mu_{l,I}, \mu_{s,I})$ is reported in Table 2.6. We stress that such values do not take into account the error on the determination of the physical scale, which is of the order of 2-3% [55, 57]; on the other hand, since such error affects all T_c values in the same way, its effect on the ratio of pseudo-critical temperatures, which is the quantity entering the determination of κ , is expected to be negligible.

In order to extract the curvature, we performed a fit to the values obtained for $T_c(\mu_{l,I})$, separately for each lattice size and setup of chemical potentials, according to the function

$$T_c(\mu_{l,I}) = T_c(0) \left(1 + 9\kappa \left(\frac{\mu_{l,I}}{T_c(\mu_{l,I})} \right)^2 + O(\mu_{l,I}^4) \right). \quad (2.21)$$

When quartic corrections turned out to be necessary, that is in the $\mu_s = \mu_l$ setup, we used instead the function¹²

$$T_c(\mu_{l,I}) = T_c(0) \left(1 + 9\kappa \left(\frac{\mu_{l,I}}{T_c(\mu_{l,I})} \right)^2 + 81b \left(\frac{\mu_{l,I}}{T_c(\mu_{l,I})} \right)^4 + O(\mu_{l,I}^6) \right). \quad (2.22)$$

In this way we got estimates of κ for all the lattices and the chemical potential setups adopted. The results of these fits are reported in Tables 2.1 and 2.2, for the critical temperatures obtained from the chiral condensate and for the chiral susceptibility respectively. In Figs. 2.5 and 2.6 data for $T_c(\mu_{l,I})$ are plotted together with the results of the aforementioned fits. In most cases, a simple linear fit (i.e. setting $b = 0$) works quite well; just for the $\mu_s = \mu_l$ setup (studied only on the $32^3 \times 8$ lattice) the introduction of a quartic correction is necessary in order to obtain reasonable values of the $\tilde{\chi}^2$ test. It is tempting to associate the enhancement of non-linear corrections in the $\mu_s = \mu_l$ setup to the fact that, in this case, the Roberge-Weiss endpoint is closer to the $\mu_l = 0$ axis, so that the associated critical behavior might have a stronger influence on the small μ_l region.

Traces appearing in the definition of chiral quantities (see, e.g., Eqs. (2.10) and (2.11)) have been computed by noisy estimators at the end of each molecular dynamics trajectory, using 8 random vectors for each flavor. Such a choice has appeared, after some preliminary tests, as a reasonable compromise to balance the effort spent in the stochastic estimators and in the gauge configuration production, i.e. in order to optimize the statistical error obtained for a given computational effort. A jackknife analysis with blocking has been exploited to determine the statistical errors, with blocks ranging in size from 80 (far from T_c) to 400 measurements (close to T_c).

¹⁰We do not report the systematic error on the determination of the physical scale, which is of the order of 2-3% [55, 57] and, being related to an overall scale determination, does not affect the ratio of pseudocritical temperatures entering the determination of κ , see Eqs. (2.3) and (2.18).

¹¹Notice that if T -dependent dimensionless combinations of the susceptibility are adopted, like, e.g., $\chi_{\bar{\psi}\psi}^r/T^4$, the behavior deviates significantly from a Lorentzian function. Moreover, the locations of the maxima move to lower values of T by about 5 MeV.

¹²Both κ and b are normalized as the coefficients that would appear in the expansion in terms of μ_B ; this is the reason of the factors 9 and 81 appearing in Eq. (2.21). Notice also that, going to the fourth order expansion, one needs to specify what is the temperature appearing in the ratio μ/T , as we have done in Eq. (2.22).

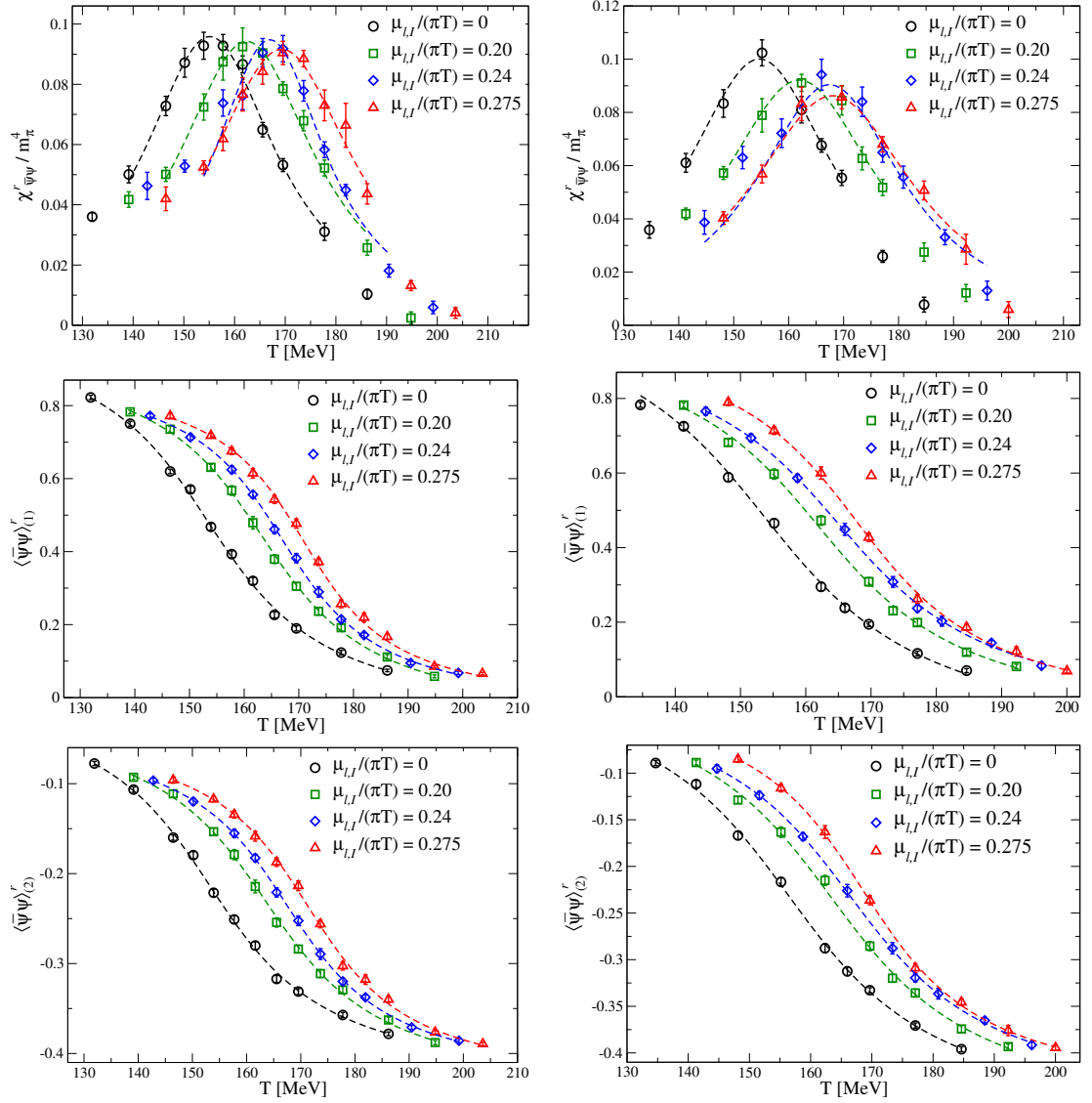


FIGURE 2.7: Renormalized susceptibility and chiral condensates for the $40^3 \times 10$ (left column) and $48^3 \times 12$ lattices (right column).

In Fig. 2.7 we report results obtained for $\chi_{\bar{\psi}\psi}^r$, $\langle \bar{\psi}\psi \rangle_{(1)}^r$ and $\langle \bar{\psi}\psi \rangle_{(2)}^r$ on the $40^3 \times 10$ and $48^3 \times 12$ lattice, together with some best fits according to Eqs. (2.19) and (2.20). In the following we will perform the continuum limit using two different methods, in order to check for systematics effects.

2.6.1 Continuum limit for $\mu_s = 0$ - First method

In order to extract the curvature of the critical line, we have performed a best fit to the values of $T_c(\mu_{l,l})$, obtained for each lattice size and setup of chemical potentials, according to the function in Eq.2.21. For all sets of chemical potentials explored for $\mu_s = 0$, the inclusion of quartic corrections has not been necessary: a more detailed discussion about the stability of the fit as the range of chemical potentials is changed is reported in Sec. 2.6.4.

Lattice	μ_s	$T_c(0)$	κ	b	χ^2/n_{dof}
$16^3 \times 6$	0.00	148.2(3)	0.0133(4)	-	1.4
$24^3 \times 6$	0.00	149.1(6)	0.0150(7)	-	0.17
$32^3 \times 6$	0.00	149.2(7)	0.0142(8)	-	0.2
$32^3 \times 8$	0.00	154.2(4)	0.0142(7)	-	1.2
$32^3 \times 8$	μ_l	154.0(4)	0.0200(6)	-	2.5
$32^3 \times 8$	μ_l	154.2(4)	0.0149(24)	0.0008(4)	0.04

TABLE 2.1: Parameters of the best fit to $T_c(\mu_{l,l})$ from the renormalized chiral condensate according to Eq. (2.21) or Eq. (2.22). Blank fields indicate that the corresponding parameter has been set to zero in that fit.

Lattice	μ_s	$T_c(0)$	κ	b	χ^2/n_{dof}
$16^3 \times 6$	0.00	150.7(4)	0.0119(6)	-	0.1
$24^3 \times 6$	0.00	151.5(5)	0.0140(7)	-	0.7
$32^3 \times 6$	0.00	152.1(3)	0.0134(5)	-	0.4
$32^3 \times 8$	0.00	155.6(6)	0.0134(9)	-	0.2
$32^3 \times 8$	μ_l	155.2(6)	0.0196(10)	-	3.3
$32^3 \times 8$	μ_l	155.6(7)	0.012(3)	0.0010(5)	1.2

TABLE 2.2: The same as in Table 2.1, but using the critical temperatures estimated from the maxima of the renormalized chiral susceptibility.

Lattice	θ_l/π	θ_s/π	C_1M_1	C_1M_2	C_2M_1	C_2M_2
$16^3 \times 6$	0.00	0.00	148.2(3)	148.2(2)	148.4(4)	148.4(2)
$16^3 \times 6$	0.20	0.00	155.0(4)	154.6(2)	155.1(5)	154.8(2)
$16^3 \times 6$	0.24	0.00	158.9(4)	157.8(2)	159.1(4)	158.1(2)
$16^3 \times 6$	0.275	0.00	161.2(4)	160.5(2)	161.5(4)	160.8(2)
$24^3 \times 6$	0.00	0.00	149.0(6)	149.0(2)	149.0(6)	149.0(2)
$24^3 \times 6$	0.24	0.00	160.8(7)	159.6(2)	160.7(5)	159.6(2)
$24^3 \times 6$	0.275	0.00	164.1(4)	163.0(2)	164.3(3)	163.1(2)
$32^3 \times 6$	0.00	0.00	149.3(3)	149.3(1)	149.4(4)	149.4(1)
$32^3 \times 6$	0.24	0.00	160.2(2)	159.5(1)	160.4(2)	159.6(1)
$32^3 \times 6$	0.275	0.00	163.5(3)	162.7(1)	163.5(3)	162.7(1)
$32^3 \times 8$	0.00	0.00	154.2(4)	154.2(2)	154.5(4)	154.5(2)
$32^3 \times 8$	0.20	0.00	162.9(8)	161.6(2)	163.0(6)	161.8(2)
$32^3 \times 8$	0.24	0.00	165.0(5)	164.5(2)	164.8(5)	164.5(2)
$32^3 \times 8$	0.275	0.00	169.5(9)	168.6(3)	168.6(7)	168.4(3)
$32^3 \times 8$	0.20	0.20	163.9(6)	163.3(2)	163.7(6)	163.4(2)
$32^3 \times 8$	0.24	0.24	169.4(7)	168.3(3)	168.6(6)	168.3(3)
$32^3 \times 8$	0.275	0.275	175.4(6)	174.1(2)	174.4(7)	174.0(3)

TABLE 2.3: Critical temperatures obtained by using different renormalization prescription and/or different definition of T_c , see text for symbol definitions.

In Fig. 2.8 we report an example of such quadratic fits to the critical temperatures obtained for $N_t = 10, 12$ and for the various explored observables. A complete collection of results, including also those already presented in Ref. [127], is reported in Table 2.7.

In a range of temperatures around T_c , the UV cutoff a^{-1} is approximately proportional to N_t . Therefore, assuming corrections proportional to a^2 , we extracted, from the curvatures obtained for different values of N_t , continuum extrapolated results according to the ansatz

$$\kappa(N_t) = \kappa_{cont} + \text{const.}/N_t^2. \quad (2.23)$$

Lattice	θ_l/π	θ_s/π	$T_c(\chi^r)$	$T_c(\chi_{disc})$
$16^3 \times 6$	0.00	0.00	150.7(4)	145.8(7)
$16^3 \times 6$	0.20	0.00	157.0(4)	151.9(9)
$16^3 \times 6$	0.24	0.00	160.0(4)	155.6(9)
$16^3 \times 6$	0.275	0.00	162.7(4)	158.0(7)
$24^3 \times 6$	0.00	0.00	151.6(5)	148.0(1.0)
$24^3 \times 6$	0.24	0.00	162.0(5)	158.3(8)
$24^3 \times 6$	0.275	0.00	165.9(4)	162.2(9)
$32^3 \times 6$	0.00	0.00	152.0(4)	147.2(1.0)
$32^3 \times 6$	0.24	0.00	162.7(4)	156.9(9)
$32^3 \times 6$	0.275	0.00	165.5(4)	161.5(1.3)
$32^3 \times 8$	0.00	0.00	155.6(7)	151.2(1.2)
$32^3 \times 8$	0.20	0.00	163.0(6)	157.2(1.0)
$32^3 \times 8$	0.24	0.00	165.8(8)	160.4(1.4)
$32^3 \times 8$	0.275	0.00	169.8(7)	166.1(1.3)
$32^3 \times 8$	0.20	0.20	165.3(9)	159.3(9)
$32^3 \times 8$	0.24	0.24	169.6(7)	164.8(1.5)
$32^3 \times 8$	0.275	0.275	177.0(8)	172.9(1.3)

TABLE 2.4: Critical temperatures obtained from the non-renormalized disconnected chiral susceptibility. The values obtained from χ^r are reported for reference.

Lattice	μ_s	Fit	$T_c(0)$	κ	b	χ^2/n_{dof}
$16^3 \times 6$	0.00	lin	145.8(7)	0.0126(10)	-	0.2
$24^3 \times 6$	0.00	lin	147.9(1.0)	0.0141(13)	-	0.2
$32^3 \times 6$	0.00	lin	147.0(1.0)	0.0138(16)	-	0.8
$32^3 \times 8$	0.00	lin	150.5(1.1)	0.0143(17)	-	1.3
$32^3 \times 8$	μ_l	lin	149.8(1.1)	0.0208(18)	-	3.8
$32^3 \times 8$	μ_l	quad	151.2(1.2)	0.008(5)	0.0020(7)	0.04

TABLE 2.5: Curvatures extracted from the data of Table 2.4.

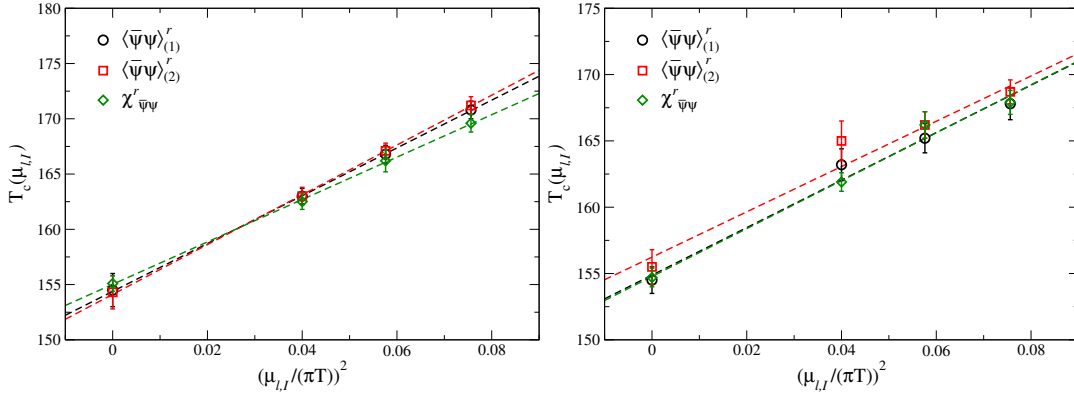


FIGURE 2.8: Critical lines for the $40^3 \times 10$ lattice (top) and for the $48^3 \times 12$ one (bottom).

Results are shown in Fig. 2.9, where we also report the extrapolated continuum values, which are $\kappa_{cont}(\langle \bar{\psi}\psi \rangle_{(1)}^r) = 0.0134(13)$, $\kappa_{cont}(\langle \bar{\psi}\psi \rangle_{(2)}^r) = 0.0127(14)$ and $\kappa_{cont}(\chi_{\bar{\psi}\psi}^r) = 0.0132(10)$.

Lattice	$\frac{\mu_{s,l}}{\pi T}$	$\frac{\mu_{s,l}}{\pi T}$	$T_c(\bar{\psi}\psi_{(1)})$	$T_c(\bar{\psi}\psi_{(2)})$	$T_c(\chi')$
$16^3 \times 6$	0.00	0.00	148.2(3)	148.4(4)	150.7(4)
$16^3 \times 6$	0.20	0.00	155.0(4)	155.1(5)	157.0(4)
$16^3 \times 6$	0.24	0.00	158.9(4)	159.1(4)	160.0(4)
$16^3 \times 6$	0.275	0.00	161.2(4)	161.5(4)	162.7(4)
$24^3 \times 6$	0.00	0.00	149.0(6)	149.0(6)	151.6(5)
$24^3 \times 6$	0.24	0.00	160.8(7)	160.7(5)	162.0(5)
$24^3 \times 6$	0.275	0.00	164.1(4)	164.3(5)	165.9(4)
$32^3 \times 6$	0.00	0.00	149.1(7)	149.4(4)	152.0(4)
$32^3 \times 6$	0.24	0.00	160.2(3)	160.4(2)	162.7(4)
$32^3 \times 6$	0.275	0.00	163.4(3)	163.5(3)	165.5(4)
$32^3 \times 8$	0.00	0.00	154.2(4)	154.5(4)	155.6(7)
$32^3 \times 8$	0.10	0.00	155.4(7)	155.2(8)	157.2(7)
$32^3 \times 8$	0.15	0.00	159.5(9)	158.9(9)	160.2(5)
$32^3 \times 8$	0.20	0.00	162.9(8)	163.0(6)	163.0(6)
$32^3 \times 8$	0.24	0.00	165.0(5)	164.8(5)	165.8(8)
$32^3 \times 8$	0.275	0.00	169.5(9)	168.6(7)	169.8(7)
$32^3 \times 8$	0.30	0.00	172.4(9)	171.8(9)	172.8(8)
$32^3 \times 8$	0.10	0.10	157.1(8)	157.0(8)	158.5(7)
$32^3 \times 8$	0.15	0.15	159.2(9)	158.8(8)	160.1(8)
$32^3 \times 8$	0.20	0.20	163.9(6)	163.7(6)	165.3(9)
$32^3 \times 8$	0.24	0.24	169.4(7)	168.6(6)	169.6(7)
$32^3 \times 8$	0.275	0.275	175.4(6)	174.4(7)	177.0(8)
$40^3 \times 10$	0.00	0.00	154.5(1.5)	154.3(1.5)	155.1(7)
$40^3 \times 10$	0.20	0.00	163.0(7)	163.0(8)	162.5(7)
$40^3 \times 10$	0.24	0.00	166.8(8)	167.1(7)	166.2(1.0)
$40^3 \times 10$	0.275	0.00	170.8(8)	171.2(8)	169.6(8)
$48^3 \times 12$	0.00	0.00	154.5(1.0)	155.5(1.3)	154.7(7)
$48^3 \times 12$	0.20	0.00	163.2(1.2)	165.0(1.5)	161.9(7)
$48^3 \times 12$	0.24	0.00	165.2(1.1)	166.2(1.0)	166.2(1.0)
$48^3 \times 12$	0.275	0.00	167.8(1.2)	168.7(9)	167.9(9)

TABLE 2.6: Critical values of T obtained from the renormalized chiral susceptibility and from the renormalized chiral condensates. Errors do not take into account the uncertainty on the physical scale, which is of the order of 2-3% [55, 57].

2.6.2 Continuum limit for $\mu_s = 0$ - Second method

Results of the previous section show that the continuum extrapolation of κ is quite smooth, with a good agreement between the results obtained with different observables and different renormalization prescriptions. This is also consistent with the preliminary evidence reported in Ref. [127].

Nevertheless, it is useful to explore different ways of performing the continuum limit, in order to check for the overall consistency of the procedure. In the previous section we first determined the value of κ at

Lattice	$\kappa(\bar{\psi}\psi_{(1)})$	$\kappa(\bar{\psi}\psi_{(2)})$	$\kappa(\chi')$
$24^3 \times 6$	0.0150(7)	0.00152(7)	0.0140(7)
$32^3 \times 8$	0.0142(7)	0.0135(7)	0.0134(9)
$40^3 \times 10$	0.0157(17)	0.0164(16)	0.0139(10)
$48^3 \times 12$	0.0130(15)	0.0123(17)	0.0131(11)

TABLE 2.7: Curvatures obtained at fixed N_t from different observables.

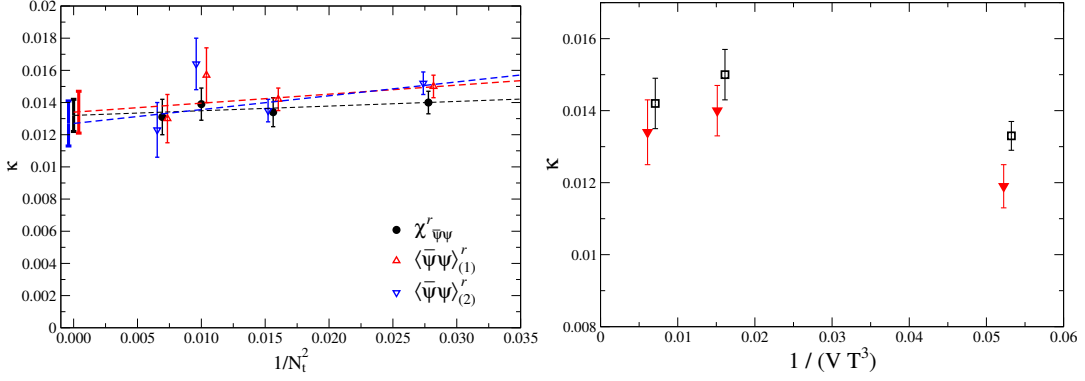


FIGURE 2.9: Left: Continuum limit of the curvatures extracted at fixed N_t (data have been slightly shifted in the horizontal direction to improve readability). Right: Fitted values of the curvature κ from the $N_t = 6$ lattices as a function of the inverse spatial volume. Squares correspond to the determinations obtained by using the chiral condensate, triangles to the chiral susceptibility estimates.

each single value of N_t , then extrapolated these results to $N_t \rightarrow \infty$ to obtain κ_{cont} . A different procedure is to first extrapolate the critical temperatures to $N_t \rightarrow \infty$ (for fixed values of the dimensionless ratio $\mu_{l,I}/T$) and then to extract the value of κ_{cont} by using the continuum extrapolated critical temperatures.

To implement the second procedure we have performed, separately for each $\mu_{l,I}/T$, a best fit to the values obtained for the renormalized condensates and for the renormalized chiral susceptibility on different values of N_t , according to modified versions of Eqs. (2.19) and (2.20). Since the cut-off dependence is more pronounced for such quantities, we have excluded $N_t = 6$ data, thus using only $N_t = 8, 10, 12$.

In detail, in the case of the renormalized susceptibility, each fit parameter appearing in Eq. (2.20) has been given an additional N_t dependence, for instance $T_c(N_t) = T_c(N_t = \infty) + \text{const}/N_t^2$. Results for the extrapolated quantities are reported in the upper plot in Fig. 2.10 where, for the sake of clarity, we report only the cases $\mu_{l,I} = 0$ and $\mu_{l,I}/(\pi T) = 0.275$. In the case of the renormalized condensates, instead, due to the larger number of parameters which are present in Eq. (2.19), we could obtain fits which are stable against the variation of the fitted range by adding an N_t -dependence to just two parameters, in particular T_c and C_1 . Results are shown in the middle and lower plot of Fig. 2.10.

Such fits provide estimates for the continuum extrapolated pseudo-critical temperatures, reported in Table 2.8 and in Fig. 2.11. Such values coincide, within errors, with the continuum pseudo-critical temperatures that one could obtain by directly fitting results reported in Table 2.6. A best fit to the extrapolated temperatures according to Eq. (2.21), with only the quadratic term included, provides

$$\begin{aligned} \kappa_{cont}(\langle\bar{\psi}\psi\rangle_{(1)}^r) &= 0.0145(11) \\ \kappa_{cont}(\langle\bar{\psi}\psi\rangle_{(2)}^r) &= 0.0138(10) \\ \kappa_{cont}(\chi_{\bar{\psi}\psi}^r) &= 0.0131(12), \end{aligned}$$

which are consistent with those found previously.

2.6.3 Strength of the transition as a function of μ_B

The width and the height of the chiral susceptibility peak, which can be obtained respectively from B_2 and A_2/B_2^2 in Eq. (2.20), are directly related to the strength of the chiral pseudo-transition. Therefore,

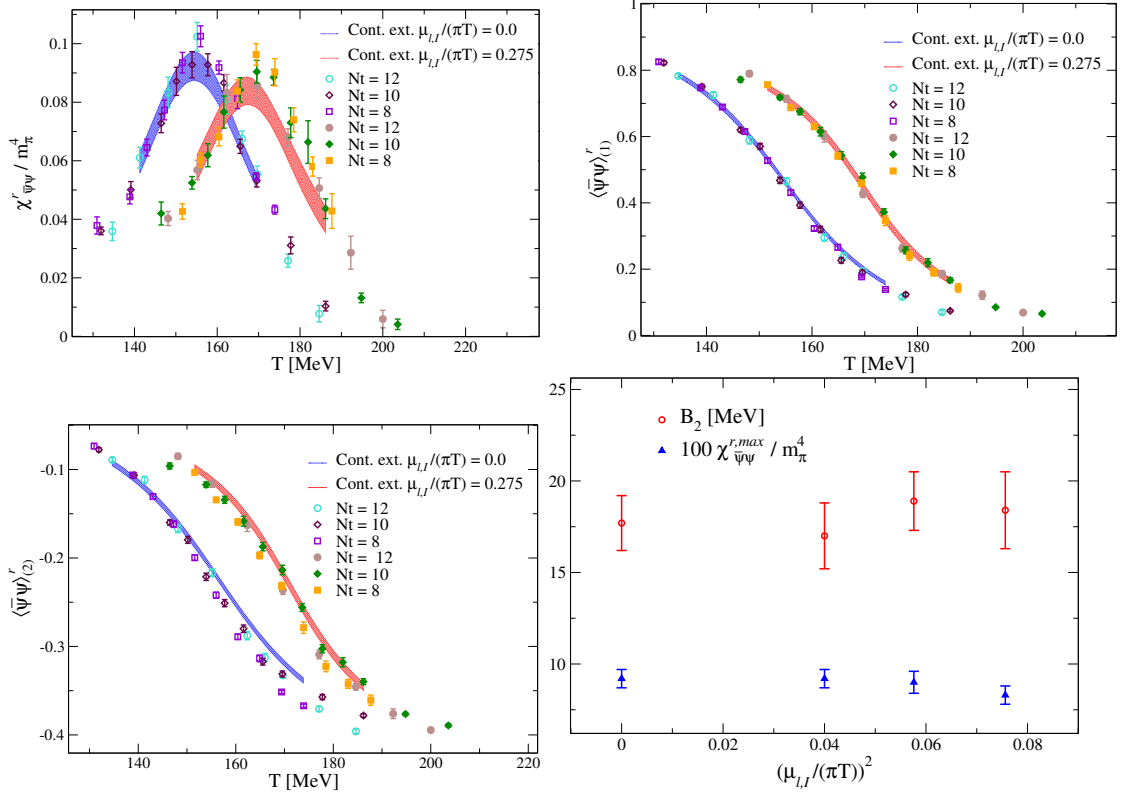


FIGURE 2.10: Top Left, top right and bottom left: Continuum limit for the renormalized susceptibility and the renormalized chiral condensates; Bottom right: Peak values ($\times 100$) and widths of the continuum extrapolated renormalized chiral susceptibility.

$\mu_{I,I}/(\pi T)$	$T_c(\bar{\psi}\psi_{(1)})$	$T_c(\bar{\psi}\psi_{(2)})$	$T_c(\chi^r)$
0.00	154.7(8)	156.5(8)	154.4(8)
0.20	163.9(8)	165.0(7)	161.0(1.1)
0.24	166.9(9)	168.5(7)	165.8(1.0)
0.275	169.7(8)	170.8(7)	167.3(1.1)

TABLE 2.8: Continuum extrapolated critical temperatures for the various $\mu_{I,I}$ values.

we have the possibility to monitor the dependence of such strength on the baryon chemical potential and, having performed a continuum extrapolation for $\chi_{\psi\psi}^r$, we can do that directly on continuum extrapolated quantities.

If a critical endpoint exists, along the pseudo-critical line, for relatively small values of real μ_B , we might expect a visible dependence of the strength parameters also for small values of imaginary μ_B . The width and the height would tend respectively to zero and infinity approaching, e.g., a critical endpoint in the Z_2 universality class.

To that purpose, in Fig. (2.10, bottom right) we plot the continuum extrapolated width B_2 and height A_2/B_2^2 as a function of $\mu_{I,I}$. No apparent change of either quantity can be appreciated, hence no dependence of the strength as a function of μ_B .

Of course, that does not exclude the presence of a critical endpoint at real μ_B : the critical region could be small enough, or the endpoint location far enough from $\mu_B = 0$, so that no influence is visible for small, imaginary μ_B . For instance, for $\mu_s = 0$, a Roberge-Weiss [50] like endpoint is expected along the

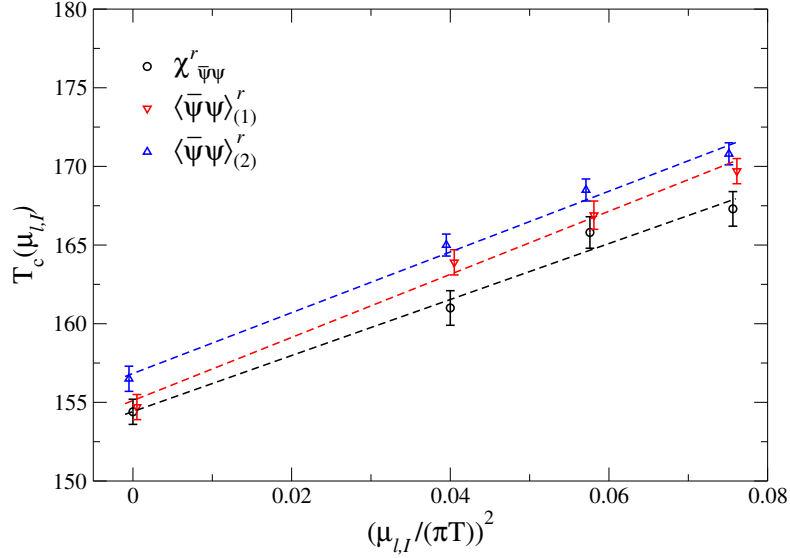


FIGURE 2.11: Critical lines obtained by using the continuum extrapolated renormalized chiral susceptibility and the continuum extrapolated chiral condensates.

pseudo-critical line at imaginary chemical potential, for $\mu_{t,I}/(\pi T) \sim 0.45$ [127]. Fig. 2.10 shows that also this endpoint has no apparent influence on the strength of the transition in the explored range.

2.6.4 Inclusion of $\mu_s \neq 0$ and systematics of analytic continuation

We have extended results for $N_t = 8$ presented in Ref. [127], performing numerical simulations for a larger range of imaginary chemical potentials, which include also the case $\mu_s = \mu_t$. That enables us to answer two important questions: what is the systematic error, in the determination of κ by analytic continuation, related to the truncation of the Taylor series in Eq. (2.21) and to the chosen range of chemical potentials? What is the impact of our effective ignorance about the actual value of μ_s corresponding to the thermal equilibrium conditions? We are going to discuss in detail only the determination of the pseudo-critical temperature from the renormalized chiral susceptibility, however we stress that similar conclusions are reached when one considers the renormalized chiral condensate. The corresponding pseudo-critical temperatures, taken from Table 2.6, are reported in Fig. 2.12 for $\mu_s = 0$ and for $\mu_s = \mu_t$. We first tried a quadratic fit in $\mu_{t,I}$: remembering the definition $\theta_t = \mu_{t,I}/T$, we used

$$T_c(\theta_t) = T_c(0)(1 + 9\kappa\theta_t^2) \quad (2.24)$$

and several fits have been performed by changing each time the maximum value $\mu_{t,I}^{(max)}$ included in the fit. Reasonable best fits are obtained in all cases, apart from the fit to the whole $\mu_s = \mu_t$ range, which yields a reduced $\tilde{\chi}^2 \sim 2.4$ and indicates the need for quartic corrections in this case. Results obtained for κ are shown in Fig. 2.12: for $\mu_s = 0$, the fitted value of κ is perfectly stable as the range of chemical potentials is changed. Instead, for $\mu_s = \mu_t$, the value of κ clearly depends on the fitted range of chemical potentials: it is larger as the range is extended and becomes compatible, within errors, with that obtained for $\mu_s = 0$ as the range is decreased. This behavior is consistent with the presence of significant quartic corrections in this case. That may be related to the different structures of the phase diagrams for imaginary chemical potential that one has in the two cases: this issue has been discussed in detail in Ref. [127].

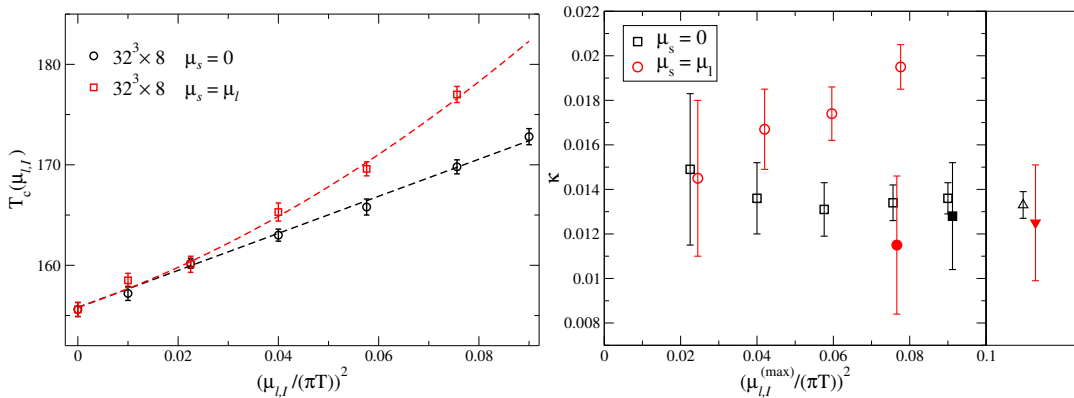


FIGURE 2.12: **Left:** Critical lines for the $32^3 \times 8$ lattices in the two different setups: $\mu_s = 0$ and $\mu_s = \mu_l$. **Right:** Stability analysis of the fit to extract the κ value for the 32×8 lattice. The value of κ is shown as a function of the maximum value of $\mu_{l,I}$ included in the fit made to obtain it. Empty (filled) symbols correspond to quadratic (quadratic plus quartic) fit; red circles (black squares) represents the $\mu_s = \mu_l$ data. The right panel shows the results for κ obtained from a combined fit (i.e. fixing a common value for $T_c(0)$) to both data sets when a quartic correction is used for the $\mu_s = \mu_l$ data: the open (filled) triangle corresponds to $\mu_s = 0$ ($\mu_s = \mu_l$).

We then tried a best fit to a function including quartic corrections,

$$T_c(\theta_l) = T_c(0)(1 + 9\kappa\theta_l^2 + b\theta_l^4), \quad (2.25)$$

to the whole range of chemical potentials explored in both cases. The corresponding results obtained for κ are reported in Fig. 2.12 as well. While for $\mu_s = 0$ the value is perfectly compatible with the one obtained without including quartic corrections (indeed, in this case one obtains $b = 0$ within errors), for $\mu_s = \mu_l$ we observe a significant change, bringing κ in good agreement with the $\mu_s = 0$ case. A similar conclusion is reached when a common fit to both sets of data (i.e. with a common value for $T_c(0)$) is performed, as shown in the right panel of Fig. (2.12, right) and in Fig.(2.12, left).

We conclude that, for $\mu_s = 0$, no evidence of quartic corrections is found in the whole explored range. As a consequence, the extracted κ is stable against variations of the fitted range and we can exclude the presence of significant systematic corrections, related to the procedure of analytic continuation, affecting the continuum extrapolated determination of κ that we have provided.

In the case $\mu_s = \mu_l$, larger values of κ are obtained when quartic corrections are neglected, however κ becomes compatible with that obtained for $\mu_s = 0$ when such corrections are included, or when the fitted range of chemical potentials is small enough. We conclude that κ is not affected by the inclusion of μ_s , at least within present errors, which however are larger than for the $\mu_s = 0$ case. In particular, a fair estimate in this case is $\kappa(\mu_s = \mu_l) = 0.013(3)$.

2.6.5 Discussion of results

Let us now analyze the main features emerging from our results. A first important point is that, as one would expect, the value of T_c at zero chemical potential is in agreement with other existing determinations in the literature [20, 31, 32, 33, 34], i.e. in a range around 155 MeV.

Comparing data at the same lattice spacing and different spatial volumes ($N_t = 6$ and $L_s = 16, 24, 32$), or

at the same physical spatial volume¹³ and different lattice spacings ($24^3 \times 6$ vs $32^3 \times 8$), one concludes that both finite size and finite lattice spacing effects are visible in the determination of the pseudo-critical temperature at zero and nonzero μ_l , both tending in general to decrease the value of T_c . It is also evident that the introduction of a non-zero $\mu_{s,l} = \mu_{l,l}$ has a significant impact, leading to a relative temperature change $T_c(\mu_{l,l})/T_c(0) - 1$ which is up to 40 % larger (at the largest value of $\mu_{l,l}$ explored), with respect to the $\mu_{s,l} = 0$ case.

On the other hand, when the dependence of T_c on $\mu_{l,l}$ is considered, in order to extract the curvature, good part of these effects boils down to a constant shift of the curves or to the introduction of quartic corrections (see Figs. 2.5 and 2.6). That means, in particular, that the curvature κ is a more stable quantity: the introduction of the strange quark chemical potential does not modify it within present errors, finite lattice spacing effects seem to be within the 10 % level. Finite size effects are of the order of 15 % when going from lattices with aspect ratio ~ 2.7 to lattices with aspect ratio 4. However they are much smaller and stay within statistical errors when going from aspect ratio 4 to aspect ratio ~ 5.3 , suggesting that they are well under control already on lattices with aspect ratio 4; all that can be appreciated from Fig. 2.9, where we report our determinations of κ for $N_t = 6$ and different spatial volumes.

2.7 Parameter sets and data at $T = 0$

The determination of the renormalized condensate and susceptibility requires the computation of the corresponding quantities at $T = 0$ and at the same UV cutoff of the finite temperature data. To that aim, we spanned a range of β on the line of constant physics, $3.5 \leq \beta \leq 3.95$. The lattice sizes have been chosen in such a way to have temperatures well below T_c , keeping at the same time finite size effects under control. This required us to perform simulations on larger lattices (going from 32^4 up to 48^4) as we decreased the value of the lattice spacing. We report results in Table 2.9.

The temperatures, which are in the range $T \sim 25 - 50$ MeV, are low enough to be considered as a good approximation of the $T = 0$ limit; indeed, as expected because of the absence of transitions in this T range, observables depend smoothly on β ; moreover no dependence at all is expected on the imaginary chemical potentials, since they can be viewed as a modification in the temporal boundary conditions which, at $T = 0$ (i.e. for infinite temporal extension), are completely irrelevant. Hence, the relatively coarse sampling of the interval is enough to permit a reliable interpolation. We adopted a cubic spline interpolation for the condensate and a linear fit for the susceptibility.

The renormalization prescription for the susceptibility that we adopted requires the subtraction of the $T = 0$ result from the $T \neq 0$ contribution. To give an idea of the relative magnitude of the two contributions, in Fig 2.13 we plot the chiral susceptibilities $\chi_{\bar{\psi}\psi}$, defined in Eq. (2.9), both at zero and at finite temperature, at zero chemical potential.

As a crosscheck, we have performed an independent determination of the pion mass on our zero temperature lattices, obtaining values in the range 133-137 MeV for the set of parameters explored: given the overall 2-3% systematic error on the determination of the lattice spacing, this is satisfactory.

¹³Lattices with the same aspect ratio L_s/N_t corresponds to approximately equal spatial volumes at the crossover, apart from the residual a -dependence of T_c .

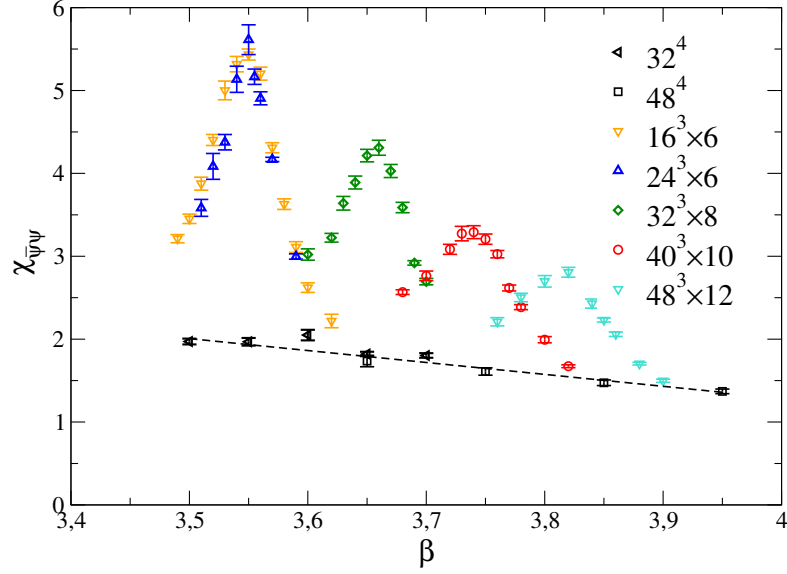


FIGURE 2.13: Comparison between the $T = 0$ and $T \neq 0$ chiral susceptibility $\mu_B = 0$. The $T = 0$ susceptibility is needed to compute the renormalized chiral susceptibility, Eq. (2.12). Data are in lattice units and a linear fit to the $T = 0$ data is shown. Looking at the data from the $N_t = 6$ lattices, the entity of finite size effects on this quantity can be assessed.

β	Lattice	$\chi_{\bar{\psi}\psi}$	$\langle \bar{\psi}\psi \rangle - 2(m_l/m_s)\langle \bar{s}s \rangle$	$\langle \bar{\psi}\psi \rangle / 2$
3.50	32^4	1.97(4)	0.07999(11)	0.04403(5)
3.55	32^4	1.97(5)	0.05680(13)	0.03164(7)
3.60	32^4	2.05(6)	0.03912(14)	0.02211(7)
3.65	32^4	1.82(3)	0.02633(2)	0.01518(9)
3.70	32^4	1.80(3)	0.01804(3)	0.01064(2)
3.65	48^4	1.74(7)	0.02638(4)	0.01521(2)
3.75	48^4	1.61(5)	0.01232(5)	0.00749(2)
3.85	48^4	1.47(4)	0.00614(2)	0.00401(1)
3.95	48^4	1.37(3)	0.00331(2)	0.00237(1)

TABLE 2.9: Determination of the observables at $T = 0$ (on the 32^4 and 48^4 lattices) needed to perform the renormalizations discussed in Section 3.3. Data are in lattice units.

2.8 Comparison with other determinations in the literature

In this section we will elaborate on how our results obtained on $N_t = 6$ and 8 lattices compare with the early ones reported by other groups. In the following subsection we analyze how the determinations of T_c and κ change if different prescriptions are adopted to renormalize observables or to locate T_c . Some of the results of this analysis can be compared more directly with some results already present in the literature. However, it must be remarked that the values we obtained with these alternative methods are not extrapolated to the continuum limit.

2.8.1 Comparison with other methods

Regarding the determination of κ from the chiral condensate we compare two different renormalization prescriptions of the condensate and two different methods to extract T_c . We set the following notation: C_1 is the chiral condensate renormalized as in Eq. (2.8), while C_2 is the one renormalized as in Eq. (2.13).

Lattice	μ_s	Fit	$T_c(0)$	κ	b	χ^2/n_{dof}
$16^3 \times 6$	0.00	lin	148.2(2)	0.0136(3)	-	0.8
$24^3 \times 6$	0.00	lin	149.0(2)	0.0139(3)	-	0.2
$32^3 \times 6$	0.00	lin	149.3(1)	0.0133(2)	-	0.1
$32^3 \times 8$	0.00	lin	154.2(2)	0.0136(3)	-	2.5
$32^3 \times 8$	μ_l	lin	154.0(2)	0.0187(3)	-	15.5
$32^3 \times 8$	μ_l	quad	154.3(2)	0.0137(9)	0.0008(2)	0.02

TABLE 2.10: Curvatures obtained by fitting the T_c s from the C_1M_2 combination of Table 2.3.

Lattice	μ_s	Fit	$T_c(0)$	κ	b	χ^2/n_{dof}
$16^3 \times 6$	0.00	lin	148.5(3)	0.0133(5)	-	1.1
$24^3 \times 6$	0.00	lin	149.1(5)	0.0152(7)	-	0.0
$32^3 \times 6$	0.00	lin	149.5(3)	0.0141(5)	-	0.4
$32^3 \times 8$	0.00	lin	154.7(4)	0.0135(7)	-	2.5
$32^3 \times 8$	μ_l	lin	154.3(3)	0.0186(5)	-	4.5
$32^3 \times 8$	μ_l	quad	154.3(3)	0.0138(11)	0.0008(3)	0.0

TABLE 2.11: Curvatures obtained by fitting the T_c s from the C_2M_1 combination of Table 2.3.

Lattice	μ_s	Fit	$T_c(0)$	κ	b	χ^2/n_{dof}
$16^3 \times 6$	0.00	lin	148.33(16)	0.0124(3)	-	12.5
$24^3 \times 6$	0.00	lin	148.49(23)	0.0147(3)	-	0.0
$32^3 \times 6$	0.00	lin	149.4(1)	0.0133(2)	-	0.0
$32^3 \times 8$	0.00	lin	154.55(17)	0.0131(3)	-	1.7
$32^3 \times 8$	μ_l	lin	154.23(18)	0.0181(3)	-	14.6
$32^3 \times 6$	μ_l	quad	154.56(19)	0.0133(10)	0.0006(8)	0.0

TABLE 2.12: Curvatures obtained by fitting the T_c s from the C_2M_2 combination (*i.e.* the same method adopted in Ref. [69]) of Table 2.3.

For what concerns the method we define M_1 as the determination of T_c obtained from the inflection point of $\langle \bar{\psi}\psi \rangle'_l$, which is the one adopted in this work. A different procedure, which we will denote as M_2 , was put forward in Ref. [69]: for each observable $\phi(T, \mu_B)$ that is monotonic in the neighborhood of the $\mu_B = 0$ transition, the authors define the critical temperature at finite chemical potential (denoted by $T_c(\mu_B)$) as the solution of the equation

$$\phi(T_c(\mu_B), \mu_B) = \phi(T_c(0), 0). \quad (2.26)$$

With this definition, along the $(T_c(\mu_B), \mu_B)$ curve we have $d\phi \equiv 0$, thus we obtain

$$\begin{aligned} \kappa &\equiv -T_c(0) \left. \frac{dT_c(\mu_B)}{d\mu_B^2} \right|_{\mu_B=0} = \\ &= T_c(0) \left. \frac{\partial \phi / \partial \mu_B^2}{\partial \phi / \partial T} \right|_{\mu_B=0; T=T_c}. \end{aligned} \quad (2.27)$$

In the latter case, we have taken the value of the condensate at the inflection point at zero chemical potential as the reference value which is kept constant at nonzero μ_B .

According to these definitions, the method that we adopted can be addressed as C_1M_1 . In Table 2.3 we show the results for T_c obtained by taking all different combinations. As we did in Section 2.6, we compute the curvature of the pseudo-critical line by fitting the extracted values of T_c by Eq. (2.21). The

results of these fits are reported in Table 2.10, 2.11 and 2.12 respectively for the combinations C_1M_2 , C_2M_1 and C_2M_2 .

Regarding the determination of κ from the chiral susceptibility, in Table 2.4 we report the results for the pseudo-critical temperature as a function of the chemical potential obtained from the non-renormalized disconnected chiral susceptibility $\chi_{\psi\psi}^{disc}$, defined in Eq. (2.10). The disconnected susceptibility is measured in lattice spacing units: that leads to an additional $T = 1/(N_t a)$ dependence, which can account for the generally lower values of T_c obtained. Again, as we did in Section 2.6, we compute the curvature of the pseudo-critical line by fitting T_c with Eq. (2.21): we report the results in Table 2.5.

We also report that a recent work has appeared, where analytic continuation is used [114]. One of the methods used to locate T_c is similar to the one we denoted here as C_2M_1 (it differs for the function used for fitting chiral condensate data).

2.8.2 The curvature of the critical line in the literature

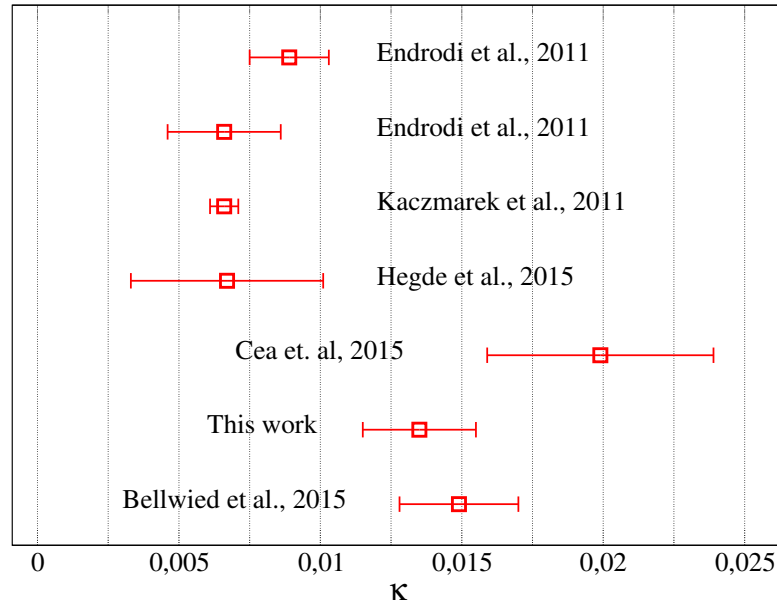


FIGURE 2.14: Determinations of the critical line curvature κ in different works. From bottom to top: *i)* Analytic continuation, strange quark number susceptibility [114]; *ii)* Analytic continuation, this work; *iii)* Analytic continuation, disconnected chiral susceptibility with $\mu_s = \mu_l$, Ref. [113]; *iv)* Taylor expansion, chiral susceptibility, Ref. [100]; *v)* Taylor expansion, chiral susceptibility, Ref. [98]; *vi)* Taylor expansion, chiral condensate (renormalization “ C_2 ”), Ref. [69]; *vii)* Taylor expansion, strange quark number susceptibility, Ref. [69].

In Fig. 2.14 we compare our present results with previous ones in the literature. We do not report many early determinations and consider only a collection of recent ones, which look at the chiral transition and have been obtained by discretizations of $N_f = 2 + 1$ QCD at or close to the physical point [69, 98, 113]. Our results seem generally larger than results obtained by the Taylor expansion [69, 98] and in marginal agreement with results obtained by analytic continuation and a different discretization [113]. However, the correct assessment of possible discrepancies or agreement requires a careful analysis of the possible sources of systematic differences between the various determinations, a task that we try to accomplish in this Section.

Part of the effects are related to the different lattice discretizations adopted and should disappear as one approaches the continuum limit. Moreover, since no real transition takes place, the result depends on the particular physical quantity and on the prescription chosen to locate the crossover at zero and non-zero μ_B . In this work, we have considered either the chiral condensate (renormalized as in Eq. (2.8)) and its inflection point, or the full chiral susceptibility (renormalized as in Eq. (2.12)) and its maximum: as we have already discussed, both are faithful, in the sense that provide a correct location of T_c in the case of a real transition.

The determinations in Ref. [98] and [100] develop on previous studies carried on by the same group about the chiral transition at $m_l = 0$ with physical m_s [128]. The basic idea is that, if for physical m_s and $m_l = 0$ the chiral transition is second order, the neighborhood of the critical point can be described by two scaling variables, t and h . To leading order only h depends on the chiral symmetry breaking parameter, *i.e.* m_l , and we thus have the relations

$$t \simeq \frac{1}{t_0} \left(\frac{T - T_c(0)}{T_c(0)} + \kappa \left(\frac{\mu_B}{T_c(0)} \right)^2 \right) \quad h \simeq \frac{1}{h_0} \frac{m_l}{m_s}, \quad (2.28)$$

where t_0 and h_0 are dimensionless factors. These can be fixed by imposing appropriate normalization conditions to the scaling functions (see [98, 128] for more details).

In Eq. (2.28) we denoted by $T_c(0)$ the critical temperature at vanishing chemical potential and, since the transition for generic μ_B is located at $t = 0$, it follows that κ is the curvature of the critical line as previously defined in Eq. (2.3). To extract the value of κ one can study an observable φ directly related to the critical behavior, like the chiral condensate, which plays a role analogous to the magnetization and, in the scaling regime, is governed by a well known scaling behavior $\varphi \equiv \varphi(t, h)$, which is fixed according to the $O(4)$ universality class and was checked at $\mu_B = 0$ in Ref. [128]. It is easy then to prove, by means of Eq. (2.28), that

$$\kappa = \frac{t_0}{\partial_t \varphi} \frac{\partial \varphi}{\partial (\mu_B/T)^2}. \quad (2.29)$$

In Ref. [98], $\partial \varphi / \partial (\mu_B/T)^2$ was measured directly in terms of a mixed susceptibility computed at $\mu_B = 0$, while $t_0 / \partial_t \varphi$ was fixed by the $O(4)$ scaling function. In this way the value of κ was inferred by imposing a scaling behavior for the mixed susceptibility computed for different values of the light quark mass.

In Ref. [112] a variant of this approach was proposed, which makes use of simulations performed at imaginary chemical potential (with $\mu_l = \mu_s$). Having at disposal data obtained at $\mu_B \neq 0$, Eq. (2.28) can be used without the need of computing derivatives of observables: results are compatible with those of Ref. [98].

In this case, a direct comparison with our determination is not easy, since one has different lattice discretizations (p4 staggered action vs stout smeared staggered action) and no proper continuum extrapolation from both sides (Ref. [98] has lattices with $N_t = 4, 8$, Ref. [112] has lattices with $N_t = 4$). Moreover, one should notice that the value of κ obtained in this way is actually the curvature of the second order line in the chiral limit $m_l = 0$, assuming $O(4)$ critical behavior; the expectation is that the dependence of κ on the light quark mass is very mild.

The strangeness susceptibility and the chiral condensate were used as the ϕ observable in Ref. [69], with the renormalization prescription in Eq.(2.13) for the chiral condensate:

$$\langle \bar{\psi}\psi \rangle'_{(2)} = \frac{m_l}{m_\pi^4} (\langle \bar{\psi}\psi \rangle_l - \langle \bar{\psi}\psi \rangle_l(T=0)). \quad (2.30)$$

In Eq. (2.27), the derivative with respect to μ_B^2 is given in terms of a susceptibility computed at $\mu_B = 0$, as for Eq. (2.28), while $\partial\phi/\partial T$ is obtained directly by numerical differentiation of data at various temperatures. Notice that this prescription for locating T_c might not be faithful in the particular case of a real transition and if the chosen observable is not an order parameter vanishing at T_c : indeed, in general, the value taken by the observable at T_c could change as the transition changes with μ_B .

In this case, a detailed comparison with our determination makes sense, since we adopt the same lattice discretization and the same physical observable (chiral condensate), even if with a different renormalization prescription. In particular we can understand, making use of our data, what is the influence on the curvature of adopting a different prescription for locating T_c and/or of adopting a different renormalization prescription for the chiral condensate (Eq. (2.8) vs Eq. (2.13)).

In Fig. 2.5 we can see that, if we use the inflection points (marked with filled triangles in the plots) as a definition of $T_c(\mu_B)$, Eq. (2.26) is only approximately satisfied, in particular at these points the condensate assumes values $\langle \bar{\psi}\psi \rangle'_l(T_c(\mu_{l,I}), \mu_{l,I})$ that decreases as $\mu_{l,I}$ is increased. Therefore, adopting the prescription of Ref. [69] and defining $T_c(\mu_{l,I})$ as the temperature for which the condensate takes the same value as for $T_c(0)$, we would obtain lower estimates of $T_c(\mu_{l,I})$ and of κ . This is indeed what happens, as shown in Section 2.8.1. Despite this consideration, however, the continuum extrapolated value of κ does not differ within the statistical errors.

A more substantial difference is obtained if, in addition, one also adopts the renormalization prescription of Ref. [69], i.e. Eq. (2.13) (see Section 2.8.1 for details). In this case our continuum extrapolated value would go from $\kappa = 0.0132(18)$ to $\kappa = 0.0110(18)$, i.e. an effect of around 20%. Therefore, about one third of the discrepancy with respect to Ref. [69], claiming $\kappa = 0.0066(20)$, can be attributed to systematic effects connected to different prescriptions for renormalization or location of T_c : this is not unexpected, in view of the fact that there is no real phase transition in the range of chemical potentials under study. Taking that into account, the remaining discrepancy between the two determinations goes below 2 standard deviations. In the future, a more rigorous continuum extrapolation of our data could better clarify the issue.

Finally, we compare with the results published in Ref. [113], in which the authors adopt the method of analytic continuation, with the setup $\mu_l = \mu_s$, and locate T_c by looking for the maximum of the disconnected part of the unrenormalized chiral susceptibility. The outcome of such analysis is in marginal agreement with our determination. One should also take into account that, as illustrated in Section 2.8.1, adopting the unrenormalized disconnected susceptibility in place of the full renormalized one leads to an increased curvature: in our case the continuum extrapolated value goes from $\kappa = 0.0126(22)$ to $\kappa = 0.0146(41)$, hence in better agreement with the outcome of Ref. [113]. That, taking into account that a different discretization was used in Ref. [113] (HISQ action), is compatible with the absence of significant lattice artifacts in both cases.

Regarding the different setup of chemical potentials, we have already verified on our results that the introduction of a non-zero μ_s does not influence the value of κ significantly, but on the other hand it

introduces larger non-linear corrections in $\mu_{l,I}^2$. In Ref. [113] there was no evidence of such non-linear corrections, even if only on the smallest lattice, namely $16^3 \times 6$, multiple values of $\mu_{l,I}$ were explored.

2.9 Conclusions

We determined the curvature κ of the pseudo-critical line of $N_f = 2 + 1$ QCD with physical quark masses with the method of analytic continuation from imaginary chemical potentials. We considered a stout smeared staggered discretization and performed simulations on lattices with $N_t = 6, 8, 10$ and 12 . In order to obtain a continuum extrapolated estimate, we used data from all the lattices we simulated having aspect ratio 4. We also enlarged the range of chemical potentials explored for $N_t = 8$: that allowed us to better estimate possible systematics related to analytic continuation.

Regarding the case $\mu_s = 0$, we have obtained continuum extrapolated values of κ from different observables (chiral susceptibility and the chiral condensate with two different renormalization prescriptions) and by two different extrapolation procedures (extrapolating κ_{cont} from $\kappa(N_t)$ or extracting κ_{cont} from continuum extrapolated temperatures). The comparison of the two different procedures permits us to give an estimate of the systematic uncertainties related to the continuum extrapolation. In the case of the renormalized chiral susceptibility ($\kappa = 0.0132(10)$ vs $\kappa = 0.0131(12)$) the systematic error is negligible in comparison to the statistical one. In the case of $\langle \bar{\psi}\psi \rangle_{(1)}^r$ ($\kappa = 0.0134(13)$ vs $\kappa = 0.0145(11)$) and of $\langle \bar{\psi}\psi \rangle_{(2)}^r$ ($\kappa = 0.0127(14)$ vs $\kappa = 0.0138(10)$) the systematic and statistical uncertainties are clearly comparable in size. The extended analysis performed on $N_t = 8$ has permitted us to state also that, within present errors, systematic effects connected to the range of μ_l chosen to extract the curvature are not significant.

Regarding finite size effects, we have shown that they are negligible within the present precision on lattices with aspect ratio 4. Taking into account the obtained results and the contributions from the systematic effects mentioned above, we quote $\kappa = 0.0135(15)$ as our final continuum estimate for the case $\mu_s = 0$.

Such a result confirms, even after continuum extrapolation, a discrepancy with previous determinations obtained by Taylor expansion [69, 98, 99], reporting $\kappa \sim 0.006$.

This is in marginal agreement with recent results obtained by the method of analytic continuation [113, 115], and larger than previous lattice determinations obtained by the Taylor expansion technique [69, 98] (notice however that larger values of the curvature have been obtained when considering different observables, like the strange quark number susceptibility or thermodynamical quantities [69, 99]). At the time of writing, another work has appeared estimating the curvature of the critical line, using analytic continuation, and a lattice action very similar to the one used by us [114]. The results are compatible with ours.

To better assess the discrepancies between our results and the ones obtained by other groups, we have analyzed various possible systematic effects. Adopting the same conventions for renormalizing the chiral condensate and for locating T_c used in Ref. [69], our estimate from the condensate would go down to $\kappa = 0.0110(18)$; hence, taking into account such systematics, the discrepancy with respect to results with the same lattice discretization appears to be below the 2σ level. Adopting the disconnected chiral susceptibility in place of the full renormalized one, as in Ref. [113, 115], our estimate from this observable would go up to $\kappa = 0.0146(41)$, in better agreement with Ref. [113, 115]. Notice that the results of this analysis are not extrapolated to the continuum limit.

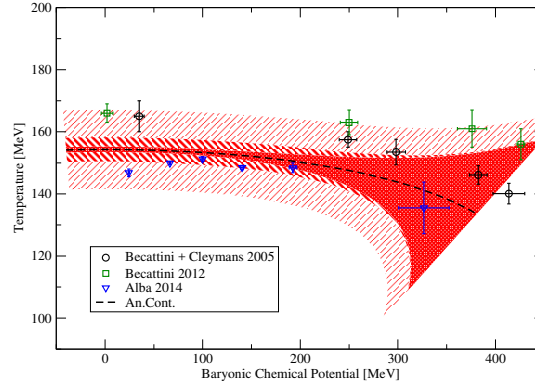


FIGURE 2.15: Tentative Analytic continuation from the data obtained by us compared with the data from heavy ion collisions [82, 83, 84].

The remaining part of the discrepancy could be possibly attributed to the systematic uncertainties related to the continuum extrapolation of previous studies. However, we stress that updated investigations by the same groups lead to results which are consistent with our estimate (see, e.g., Ref. [100]).

We have also considered the effects of the introduction of a nonzero strange quark chemical potential $\mu_s = \mu_l$, finding that the curvature stays unchanged within the present accuracy.

However, there is evidence for the presence of quartic contributions in the dependence of T_c on the imaginary μ_B in this case. The origin of this difference could be related to the different phase structure which is found, for imaginary chemical potentials, at the different values of μ_s . In particular, the so-called Roberge-Weiss line and the associated non-analytic behavior moves further from the $\mu_l = 0$ axis when $\mu_s = 0$. Anyway, when such contributions are taken into account, or when the range of fitted chemical potentials around $\mu_B = 0$ is small enough, the curvature becomes compatible, even if within larger errors, with that obtained for $\mu_s = 0$. That means that also for the equilibrium conditions created in heavy ion collisions, corresponding to $\mu_s \sim 0.25 \mu_l$ around T_c , one does not expect significant deviations from the results obtained for $\mu_s = 0$: a prudent estimate for the curvature in this case is¹⁴ $\kappa = 0.0135(20)$. That is obtained based on the estimate for $\mu_s = 0$, with an increased error determined on the basis of the uncertainty that we have for the curvature extracted at $\mu_s = \mu_l$.

Finally, the analysis of the continuum extrapolated peak of the chiral susceptibility as a function of imaginary μ_B shows no significant variations of the strength of the transition, which could be associated to a possible nearby critical endpoint present along the pseudo-critical line.

As an addition, in Fig.(2.15) a tentative extrapolation to real μ_B is presented. The systematic errors are estimated - quite arbitrarily - assuming that the possible term of order six is comparable with the quartic term in magnitude at the upper end of the range in μ_B/T . In the same figure the data for the freeze-out point determined in [82] is reported, along with the result of a refined analysis [84] and of another recent determination of the chemical freeze-out point [83]. The black line is the extrapolated critical line, the darkest red band is the statistical error, the lightest red band is the width of the transition found performing the continuum limit with method 2, and the intermediate band is the sum of the systematic error and the error on the scale (which is assumed to be 2.5% [55, 56]). It must be remarked that this assumption is arbitrary and the value of the analytic continuation to real chemical potentials is only qualitative.

¹⁴After completion of this work, Ref. [114] has appeared, reporting the consistent result $\kappa = 0.0149(21)$.

Chapter 3

At Large $\text{Im}\mu_B$: the Roberge-Weiss phase transition

3.1 The Roberge-Weiss transition

In the case of QCD with a purely imaginary baryon chemical potential [30, 101, 102, 103, 104, 129], the partition function is

$$Z(T, \theta_B) = \text{Tr} \left(e^{-\frac{H}{T}} e^{i\theta_B B} \right) \quad (3.1)$$

where H is the QCD Hamiltonian, B is the baryon charge and $\theta_B = \text{Im}(\mu_B)/T$. All physical states of the theory, over which the trace is taken, are globally color neutral and carry an integer valued baryon charge B , hence Z is 2π -periodic in θ_B , or alternatively $2\pi/N_c$ -periodic in $\theta_q = \text{Im}(\mu_q)/T$, where $\mu_q = \mu_B/N_c$ is the quark chemical potential and N_c is the number of colors. That can also be proven by making use of center transformations in the path-integral formulation of the partition function, as we review in Section 3.3.

Due to the parity and the 2π -periodicity of Z in θ_B , $\langle B \rangle$ will be an odd function of θ_B with the same period 2π . This implies that either $\langle B \rangle$ is null for $\theta_B = \pm\pi$, or Z has a non-analytic behavior, associated with first order phase transition lines present for $\theta_B = \pi$ (or odd multiples of it). These are known as Roberge-Weiss (RW) transitions [50] and have been widely studied by lattice QCD simulations [42, 54, 101, 102, 103, 104, 108, 111, 123, 130, 131, 132, 133, 134, 135, 136, 137, 138, 139].

In correspondence with such points, analogously to what happens when θ_B is a multiple of 2π , the theory is invariant under charge conjugation, but contrary to that case charge conjugation is spontaneously broken at high T , where the system develops a non-zero expectation value for the imaginary part of the baryon number density: the temperature T_{RW} where the spontaneous breaking takes place is precisely the endpoint of the Roberge-Weiss first order transition lines. An alternative point of view about the same transition is to look at it as a quantum (i.e. zero temperature) transition, with an associated spontaneous breaking of charge conjugation, driven by the compactification of one of the spatial directions below a critical size $L_C = 1/T_{\text{RW}}$ (finite size transition [140, 141]). Since charge conjugation is a Z_2 symmetry, one expects a $3d$ -Ising universality class if the transition is second order, or alternatively a first order transition with the development of a latent heat.

The temperature T_{RW} and the critical behavior to which it is related represent universal properties of strong interactions, directly related to the change in the effective degrees of freedom propagating in the thermal medium, hence to deconfinement. They can be carefully studied by lattice QCD simulations, since the path integral measure is real and positive for imaginary chemical potentials. Despite being related to a critical point located in an unphysical region of the QCD phase diagram, their importance and relevance to a full understanding of strong interactions stems from various considerations:

- The RW endpoint may influence physics in a critical region around it. Moreover, if at the RW endpoint a first order transition is present, the endpoint is actually a triple point, with further departing first order lines, the endpoints of which may be even closer to the $\mu_B = 0$ axis, with more interesting consequences.
- Early studies have shown that the RW endpoint transition is first order for small quark masses, second order for intermediate masses, and again first order for large masses; the three regions are separated by two tricritical points [130, 131, 132]. The emergence of this interesting structure has induced many further studies in effective models [142, 143, 144, 145, 146, 147, 148, 149, 150, 151, 152, 153, 154] which try to reproduce the essential features of QCD. Moreover, interesting proposals have been made on the connection of this phase structure with that present at $\mu_B = 0$ (the so-called Columbia plot) and on the possibility to exploit the whole phase structure at imaginary chemical potential in order to clarify currently open issues on the phase structure at $\mu_B = 0$, like the order of the chiral transition for $N_f = 2$ [42, 139].
- Once the RW endpoint has been precisely located, it can be taken as a test ground to compare the lattice techniques presently used to locate the critical point at real μ_B , so as to assess their reliability and guide future research on the subject.
- The relation of the RW endpoint to the other symmetries of QCD, which are present at least in well defined limits of strong interactions, is an interesting issue by itself, which can help elucidate some fundamental non-perturbative properties of the theory.

In what follows we study the properties of the RW endpoint by lattice simulations of QCD with physical quark masses. In Section 3.2 we determine, without continuum limit extrapolation, the location of the RW-like transition happening in $N_f = 2 + 1$ QCD when the strange quark chemical potential is set to zero. In Section 3.4 the location T_{RW} of the proper RW transition (that is, the one that happens when $\mu_l = \mu_s = i\frac{\pi}{3}T$) is determined for various lattice spacings, corresponding to temporal extensions $N_t = 4, 6, 8, 10$, and then extrapolated to the continuum limit. Moreover we are able to determine its universality class, through a finite size scaling analysis, at two different lattice spacings, namely $N_t = 4, 6$. Moreover, in order to approach the issue of the interconnection between chiral symmetry and the RW endpoint, we consider the relation of the endpoint location to the analytic continuation of the pseudocritical chiral transition temperature $T_c(\mu_B)$ to imaginary chemical potentials. Finally, we show some preliminary results about the RW transition towards the chiral limit.

3.1.1 The Roberge Weiss transition in the literature

The Roberge-Weiss $N_f = 2$ transition was recently studied with unimproved staggered fermions on $N_t = 4$ lattices in [130, 131]. A picture emerged, where in the chiral and infinite mass limits the Roberge-Weiss

transition would be first order, while it would be second order for intermediate masses (see Fig.1.4 and the discussion in Chapter 1 for a description of the two situations). For the values of the quark mass where the transition is first order, the critical point $T = T_c$, $\mu = i\pi T/3$ (or, equivalently, $\mu = i\pi T$) is actually a triple point, where the two high-temperature phases (which differ in the sign of the imaginary part of P) coexist with the low temperature phase, where $\langle \text{Im } P \rangle = 0$. On this triple point three first order lines join: the line of the $\mu_{I,q}$ -driven Z_2 transition at high temperature, and the two chiral/deconfinement transition lines for $\mu_{I,q} < \pi T/3$ and for $\mu_{I,q} > \pi T/3$, one of which is related to the critical line of QCD studied in the first part of this Thesis ¹. These two latter ones may end at a further critical point, or continue until $\mu_{I,q} = 0$: in that case, we would have a first order chiral/deconfining phase transition even at $\mu_{I,q} = 0$.

An example of why studying QCD at imaginary chemical potential can be relevant to the $\mu_{I,q} = 0$ case is [42]. In that work the relation between $m_{tric;l}$ (the value of m_l below which the chiral transition becomes first order) and $\mu_{I,q}$ was studied for $N_f = 2$, taking advantage of the fact that for larger $\mu_{I,q}$ the value $m_{tric;l}$ increases, thus reducing the computational cost of the simulations. Assuming that the point where $m_{tric;l}(\mu_q^2)$ vanishes is a tricritical point [155, 156], data on the $m_{tric;l}(\mu_{I,q})$ dependence were interpolated with a tricritical scaling ansatz, and extrapolated to $\mu = 0$, finding that $m_{tric;l}(0)$ is greater than zero, thus suggesting that for $N_f = 2$, the chiral phase transition is first order for $m_l = 0$, at least for the $N_t = 4$ lattice. Anyway, as pointed out in [37], lattice artifacts seem to heavily affect quantitative predictions, in the sense that transitions are generally weakened towards the continuum limit.

The two values $m_\pi^{tric;l}$ and $m_\pi^{tric;h}$ of the pion mass for which the transition becomes first order indicate two tricritical points (see the bottom plane in Fig.1.2, right). While the fact that at large mass the transition would be first order is expected, since in that limit quarks decouple and we recover the deconfining transition in pure gauge $SU(3)$, which has been found to be first order in [41], the fact that it is first order also in the chiral limit is non trivial. The $N_f = 3$ case was studied in [132], where the Authors came to similar conclusions. This picture for $N_f = 2$ has been more recently confirmed by simulations with Wilson fermions on lattices with temporal extension N_t equal to 4 and 6 [54, 138]. Unfortunately, as already suggested in [132], $m_\pi^{tric;l}$ and $m_\pi^{tric;h}$ seem to be heavily affected by UV cutoff effects: in particular, $m_\pi^{tric;l}$ decreases as the lattice spacing is decreased. There is no compelling reason why it should not go to zero in the continuum limit: in that case, the first order region would disappear.

The order of the Roberge-Weiss transition for physical quark masses was studied, in [157], where the Authors found that on $N_t = 4$ and $N_t = 6$ lattices the transition was of the second order type. There is no direct proof that the transition is second order in the continuum limit, but the fact that $m_\pi^{tric;l}$ decreases towards the continuum limit while $m_\pi^{tric;h}$ is much larger than the physical value, as suggested in [54, 138]² suggests that the transition for physical quark masses keeps being of the second order kind even in such limit.

3.1.2 Our goals

Our goal is to study the nature of the Roberge-Weiss transition as a function of mass, keeping the ratio m_s/m_l constant, and equal to the physical value ~ 28.15 . For each value of the masses, we aim to discriminate between the two possible scenarios: either the transition is first order or it is second order.

¹Notice that in the first part of this thesis the theory $N_f = 2 + 1$ was studied, with (mainly) $\mu_s = 0$.

²Scale setting in these works (which study non-physical theories) is performed using the method described in [158], based on the so-called Wilson Flow [159].

Since the system exhibits a Z_2 global symmetry in the order parameter $|\text{Im}P(\vec{x})|$, this means that it falls in the Ising 3D universality class. The values of the critical exponents can thus either be the first order ones, or the Ising 3D ones. The critical exponents for a first order transition can be found analytically, while the ones for a second order transition for the Ising 3D universality class have been found with great accuracy with numerical simulations [160]. Another way of discriminating between these two possibilities is to look at the Binder cumulant crossing for various volumes [161, 162]: in this case there is as well a large literature where the crossing values have been calculated accurately [163].

It must be noted that we are approaching the same kind of chiral limit as in $N_f = 3$, for which in the case $\mu = 0$ the *chiral* phase transition has been proven to be first order [36]. If the usual picture holds, where the critical line ends up at the Roberge-Weiss endpoint and the effect of an imaginary chemical potential is to strengthen the transition, this means that in such limit the RW endpoint should be a triple point, and the RW transition should be of the first order kind.

3.1.3 Determination of the order of the transition: Finite size scaling

A commonly used tool in computational statistical physics to find the properties of a phase transition (e.g. computing the critical exponents or determining precisely the critical point) is finite size scaling. Here our aim is much simpler: we already know that only two cases are possible, and the critical exponents for the two cases are already known. We first focus on the second order case. In the following, we just need to recall the meaning of the ν and γ critical exponents³, which hold in the neighborhood of a critical point:

- The behaviour of the correlation length as a function of the reduced temperature is

$$\xi \propto |t|^{-\nu} \quad (3.2)$$

- The behaviour of the susceptibility as a function of the reduced temperature $t = |T - T_c|$ is

$$\chi \propto |t|^{-\gamma} \quad (3.3)$$

Of course, these relations are valid only in an infinite system or where the size of the system L is much larger than the correlation length ξ . When the condition $\xi \ll L$ is not true any more, the fact that the system has a finite size causes the following effects:

1. The susceptibility of the order parameter will not diverge, but have a maximum, which will be proportional to L^ζ ;
2. The temperature at which the susceptibility of the order parameter is maximal will be different from the one in the thermodynamic limit. The difference between the finite size maximum temperature and the transition temperature in the thermodynamic limit will be proportional to $L^{-\lambda}$;
3. At finite system size *true* phase transitions cannot happen, because the partition function will *always* be analytic. This means that any transition will always manifest itself, in a finite-size

³ For a general review on the subject of critical exponents and the scaling relations between them, the reader can refer e.g. to [164, 165]. The following reminder of finite size scaling is based on [166].

system, as a crossover which will sharpen more and more as the thermodynamic limit is approached. The width of this analytical crossover will be proportional to $L^{-\theta}$;

As we shall immediately see, there is a relation between ζ , λ and θ and the critical exponents γ and ν . A measure of the violation of the condition $\xi \ll L$ is given by the ratio ξ/L , which according to Eq.3.2 should be proportional to $1/(L^{1/\nu}|t|)$ elevated to the ν -th power. Following this line of reasoning, we expect that the minimum value of $|t|$ for which the behaviour of the system will differ significantly from the infinite volume limit will be proportional to $L^{-1/\nu}$.

As far as χ is concerned, we can assume that the scaling relation 3.3 will be modified as follows:

$$\chi = \xi^{\gamma/\nu} \chi_0(L/\xi) \quad (3.4)$$

where the function χ_0 contains the finite size effects; χ_0 is defined to be constant for large x , and so that when ξ becomes large, χ will saturate: for this it is necessary that $\chi_0(L/\xi) \propto (L/\xi)^{\gamma/\nu}$ when $L/\xi \ll 1$. Making use of Eq.3.2 to get rid of the unknown ξ , Equation 3.4 can be recast in a more convenient form⁴:

$$\chi = L^{\gamma/\nu} \tilde{\chi}_0(L^{1/\nu}t) \quad (3.5)$$

where $\tilde{\chi}_0(x) = x^{-\gamma} \chi_0(x^\nu)$ has the property that it tends to a constant for $x \rightarrow 0$. From this relation we can promptly see the effects of the finite size of the system on the behaviour of χ : moreover, the function

$$\tilde{\chi}_0(x) = L^{-\gamma/\nu} \chi(xL^{-1/\nu}) \quad (3.6)$$

does not depend on L , as long as we are in the critical region, where the scaling relations 3.2 and 3.3 hold. Testing this claim is the idea behind the collapse plot method: the possible values of γ and ν are known a priori, depending on the order of the transition, and we can test the hypothesis that the quantity $L^{-\gamma/\nu} \chi(xL^{-1/\nu})$ is independent of L in the two cases, that is second order or first order. In the case of a second order transition, the critical exponents depend on the universality class (in our case, the one of the three-dimensional Ising model). In the first order case it is possible to calculate the exponents to use for finite size scaling in a general way, making use of a simple model.

3.1.3.1 The case of a tricritical point

The transition may also take place at a tricritical point, which can be defined as the end point of a three-phase coexistence line (as a critical point is the end point of a two-phase coexistence line), or as the point where a first order phase transition becomes of the second order kind. Such a situation can be described by a Landau-Ginzburg effective theory, where the fourth-order coefficient changes sign in the correspondence of the tricritical point. Of course, in that case a sixth-order term is necessary to stabilize the theory. Interestingly enough, the fact that the fourth order term vanishes at the tricritical point makes the Ginzburg criterion more and more valid the closer to the tricritical point, and this makes the mean field description more and more valid⁵. Anyway, the case in which the pion mass coincides with $m_\pi^{\text{tric};l}$

⁴Actually, we should have two different functions, depending on $|t|$, for $t > 0$ and $t < 0$ respectively, but they can eventually be combined into one.

⁵Apart from logarithmic corrections to scaling, which are not shown by the critical indices.

or $m_\pi^{tric;h}$ requires a fine tuning of the quark mass, and for this reason the probability of being in this case is rather low and that situation will not be analyzed here⁶(for details, refer e.g. to [167], §150).

3.1.3.2 The first order case

In the case of a first order transition, the argument to be used in the study of finite size scaling differs; in particular, we do not expect the correlation length to diverge. The divergences in thermodynamic quantities do not arise from the divergence in the correlation length, but from phase coexistence. Nonetheless, in the case of symmetric first order transitions⁷ it is possible to obtain an universal function like in the second order case, and more in general it is possible to assess the most important finite-size effects. Let us take the example of a field-driven first order transition. We can describe finite size scaling around such transition between two phases with a simple model, the “double Gaussian approximation” [168]. In the following, we will restrict the discussion to a symmetric transition, since the generalization is trivial. In this case, the order parameter will be distributed as

$$P_L(s) = \mathcal{N}(\beta, H) \left(\exp \left[-\beta L^d \frac{(s - M_{sp})^2}{2\chi} \right] + \exp \left[-\beta L^d \frac{(s + M_{sp})^2}{2\chi} \right] \right) \exp \left[\beta L^d s H \right], \quad (3.7)$$

where $\pm M_{sp}$ is the average value of the order parameter in the two phases, while χ represents the *intensive* susceptibility in each phase and \mathcal{N} is the appropriate normalization factor. Notice that s represents the spatial average over a region of size L^d of a local observable (e.g., the magnetization in the Ising model). A remark on Eq.(3.7) is in order. Here, the size L^d of the region where s is averaged over must be small enough so that it contains mostly just one phase, otherwise $P_L(s)$ cannot be double peaked. On the other hand, looking at this model from a Landau-Ginzburg viewpoint, it must be large enough so that the derivative terms in the Landau free energy can be neglected. Working out the calculations, it is possible to obtain the mean value $\langle s \rangle_{P_L}$ and the fluctuation of the order parameter, $\langle s^2 \rangle_{P_L} - \langle s \rangle_{P_L}^2$. Of course, for the *intensive* susceptibility of the finite system, from Eq.(3.7) we have⁸

$$\chi = \frac{\partial \langle s \rangle_{P_L}}{\partial H} = \beta L^d [\langle s^2 \rangle_{P_L} - \langle s \rangle_{P_L}^2] \propto L^d \quad (3.8)$$

It can be expected that the maximum of the fluctuations at the phase transition (in this case when $H = 0$) will be dominated by the distance between the peaks in the order parameter distribution, while the contribution of χ is a correction that decreases as L^{-d} . Moreover, since in Eq.3.7 the dependence on the field H appears only through the quantity $L^d H$, it is natural to write

$$\chi = L^d \tilde{\chi}_0(L^d H), \quad (3.9)$$

and taking the analogy with Eq. 3.5 we obtain $\nu = 1/d$, $\gamma = 1$. The case of temperature-driven first order transitions has been studied with an approach similar to [168] in [169]. In [169] it is stated that at the transition the *height* of the two Gaussians must be equal, instead of the *area*, which is the assumption

⁶ If we are close to a tricritical point, we may expect corrections to finite size scaling (which may be significant for small lattice volumes).

⁷ That is, where the partition function is symmetric in a scaling variable, e.g., the external field $Z(t, h) = Z(t, -h)$.

⁸ When the size L of the system becomes large enough that different phases can coexist, the situation could be different, but the configurations where this happens are actually suppressed by interface energy (in $d \geq 1$). See also [161] for a discussion about the effect on P_L of phase coexistence.

made instead in [168]. This last statement was proven to lead to slightly incorrect results in [170, 171]⁹ by justifying a generalization of [168]. In order to describe temperature-driven first order transitions, we follow a more general and rigorous approach to finite size scaling for first order transitions which has been proposed in [170, 171]. The idea is that close to a first order transition¹⁰, the partition function can be written as

$$Z(h, L) \simeq \sum_{q=1}^N \exp(-f'_q L^d) \quad (3.10)$$

where f'_q is a “metastable” energy density associated to the phase q (which depends on the external fields and temperature). When q is a stable phase, f'_q is equal to the actual free energy density βf , while for unstable phases $f'_q > \beta f$. The consequences of this assumption can be worked out in the case of two phases, with a parameter h driving the transition (which can also be the reduced temperature t , and the generalization to a higher number of phases is straightforward). It is reasonable to assume that near the transition (which we assume to happen at $h = 0$) f'_q can be expanded in powers of h :

$$f'_q(h) = f'_q + m_q h + \frac{1}{2} \chi_q h^2 + O(h^3). \quad (3.11)$$

The value of an observable M can be computed as

$$M(h, L) = \sum_{q=1}^N P_q(h) M_q(h) \quad (3.12)$$

where

$$M_q(h, L) = -\frac{\partial f'_q(h)}{\partial h}, P_q(h, L) = \frac{\exp(f'_q(h) L^d)}{Z(h, L)} \quad (3.13)$$

From this expression it is easy to work out the results. As an example, we take the case of the q -state Potts model. As proven in [172], for $2 \leq q \leq 4$ the model has a second order phase transition, while for $q \geq 5$ the temperature-driven transition is of the first order kind. In this second situation, where the system has q ordered phases and one disordered phase, Eq. 3.10 becomes

$$Z(h, L) \simeq q \exp(-\beta f_o L^d) + \exp(-\beta f_d L^d). \quad (3.14)$$

Working out the elementary calculations, it is possible to assess the finite size effects affecting thermodynamic quantities. In particular, it can be seen that for any kind of first order transition the peak shrinks in width as $\propto L^{-d}$, it grows as $\propto L^d$, it is shifted by $\propto L^{-2d}$ (but for symmetrical phase transition the shift is proportional to L^{-3d}). For more details, refer to the Theorems and other references in [170, 171].

⁹ The hypothesis of the two Gaussians having the same height leads to the conclusion that the deviation of the susceptibility peak position from its infinite-volume value scales as L^{-d} (see [169], Eq.20), while it turns out that, at least in the case of only two phases coexisting, the right behaviour is L^{-2d} ([170], Eq 3.15).

¹⁰It must be reported that, as stated in [171], the results of [170] have been rigorously proven only for a class of models at low temperature. The conjecture of [171] is that they are valid also at higher temperature where multiple phases coexist with a finite correlation length.

3.1.3.3 The Binder cumulant and finite size scaling

Let us consider a system with an order parameter s and close to a second order transition. The order parameter s follows a probability distribution $P_L(s)$. We can define the Binder cumulant as

$$B_4 = \frac{\langle (s - \langle s \rangle)^4 \rangle}{\langle (s - \langle s \rangle)^2 \rangle^2}. \quad (3.15)$$

In the case where $P_L(s)$ is Gaussian (above T_c) we have $B_4 = 3$, while when $P_L(s)$ is double peaked (and peaks have infinitesimal width, like in the $T \rightarrow 0$ limit) $B_4 = 1$ instead. Let us follow the analysis of [161]. We assume the probability distribution $P_L(s)$ to satisfy a scaling relation ¹¹

$$P_L(s) = L^x \hat{P}(asL^y, \xi/L) \quad (3.16)$$

where \hat{P} is an universal scaling function, while \hat{P} and a are constants. From the normalization constraint one obtains easily $x = y$, and note that

$$\int_{-\infty}^{+\infty} dz \hat{P}(z, \xi/L) = a/\hat{P} = C_0, \quad (3.17)$$

for all ξ/L . It is possible to calculate the moments using the same expression for $P_L(s)$:

$$\begin{aligned} \langle s^k \rangle_L &= L^x \hat{P} \int_{-\infty}^{+\infty} ds s^k \hat{P}(asL^x, \xi/L) = \\ &= L^{-kx} \frac{\hat{P}}{a^{k+1}} \int_{-\infty}^{+\infty} dz z^k \hat{P}(z, \xi/L) = \\ &= L^{-kx} \frac{\hat{P}}{a^{k+1}} f_k(\xi/L), \end{aligned} \quad (3.18)$$

where the functions f_k are universal as well. We thus can express B_4 as

$$B_4(\xi/L) = \frac{a f_4(\xi/L)}{\hat{P} f_2(\xi/L)^2}. \quad (3.19)$$

Since ξ diverges at the critical point, the value of B_4 at T_c will be independent of L , and it will depend only on the universality class.

3.2 Location of the Roberge-Weiss-like transition for $\mu_s = 0$

The presence of the RW transitions places a limitation on the region of imaginary chemical potentials available to analytic continuation: for high T , only chemical potentials such that $\theta_l < \pi/3$ can be used to investigate the dependence of the free energy for small values of μ_l , since for $\theta_l > \pi/3$ one is exploring a different analyticity sheet of the free energy, corresponding to a different center sector, even if with identical and periodically repeated physical properties. The pseudo-critical line itself, in particular, develops a non-analyticity at $\theta_l = \pi/3$: numerical evidence is that it touches the RW endpoint, where it forms a cusp, and then repeats periodically; such a situation is depicted schematically in Fig.(3.2, bottom left).

¹¹In [161] P_L is actually the probability distribution of s averaged on a L^d cell of the system.

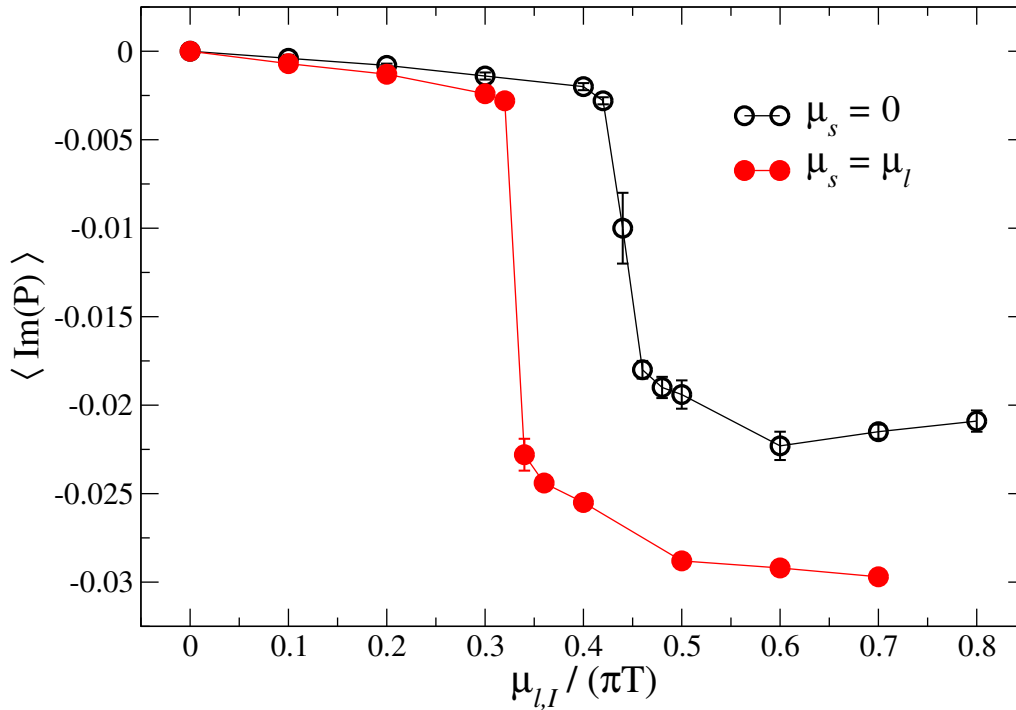


FIGURE 3.1: Imaginary part of the Polyakov loop as a function of θ_l at fixed $T \approx 208 \text{ MeV}$ for $\mu_s = \mu_l$ and for $\mu_s = 0$.

When one adopts the setup in which $\mu_d = \mu_u \equiv \mu_l \neq 0$ and $\mu_s = 0$, the phase diagram in the $T - \theta_l$ plane looks different. The strange quark determinant is independent of θ_l and that breaks the $\pi/3$ periodicity in θ_l . In particular, as θ_l is increased, the effective coupling of the up and down quark determinants to the Polyakov loop will rotate by an angle $-\theta_l$, while that of the strange quark will stay oriented along the positive real axis. As a consequence, the critical value of θ_l at which, in the high T regime, the Polyakov loop jumps from one sector to the other, will be higher than $\pi/3$. Given the residual 2π periodicity in θ_l and the symmetry under inversion of θ_l , the expected phase diagram is depicted schematically in Fig. (3.2, bottom right): we still have RW-like transition lines at high T , which however take place for different values of θ_l (apart from the one at $\theta_l = \pi$) and separate sectors of the theory which are not equivalent to each other.

We have verified this expectation explicitly by monitoring the Polyakov loop as a function of θ_l in the two different setups: results are reported in Fig. 3.1, where we plot the imaginary part of the Polyakov loop (which jumps when the boundary between two different center sectors is crossed) as a function of θ_l . While for $\mu_s = \mu_l$ the jump takes place at $\theta_l = \pi/3$, as expected, when $\mu_s = 0$ the jump moves forward and takes place approximately at $\theta_l \simeq 0.45\pi$, for $T = 208 \text{ MeV}$. In the regime of asymptotically high temperatures instead, a perturbative computation performed making use of the one loop effective potential for the Polyakov loop in the presence of massless quarks, gives $\theta_c \approx 0.482933\pi$.

3.2.1 One loop Polyakov effective potential

As already discussed in Section 1.4.3, the effective potential for the Polyakov loop can be computed in perturbation theory, obtaining results valid in the limit of very high temperature. Formulas 1.25 and 1.24 can be modified to take the chemical potentials into consideration.

As noted in Section 2.5, one expects the position of these transitions to change when $\mu_u = \mu_d$ but $\mu_s = 0$. This can be explicitly seen by using Eq. (1.25). The potential evaluated on the three cubic roots of the identity is plotted in Fig. (3.2, upper panel), where $\theta_l = \text{Im}(\mu_l)/T$: the level crossings (corresponding to sector changes) move with respect to the $\mu_l = \mu_s$ setup, the first one being located at $\theta_c \approx 0.482933\pi$. For comparison, we report also the analysis for the standard RW case ($\mu_s = \mu_u = \mu_d$) in Fig. 3.2.

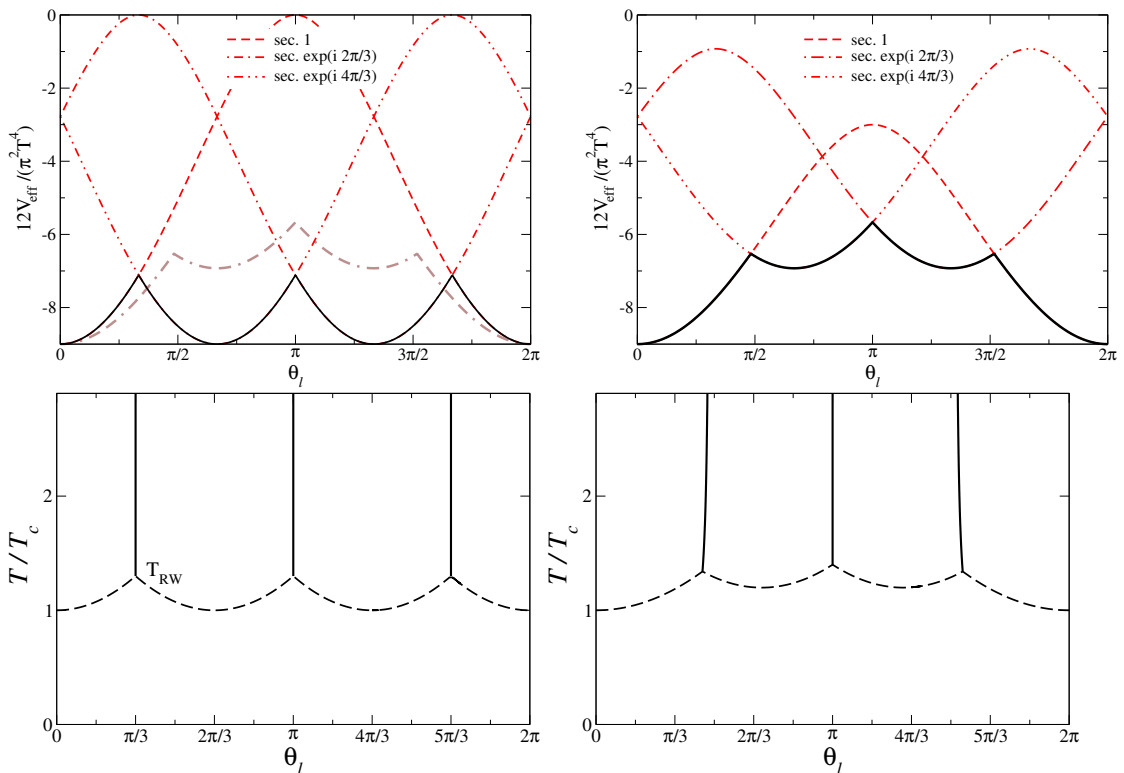


FIGURE 3.2: Top Left: Effective Polyakov loop potential computed from Eq. (1.26) for $\mu_u = \mu_d = \mu_s$. This is actually the same as Fig. 2 of Ref. [50] (or Fig.1.3). Top Right: the same for $\mu_u = \mu_d$ and $\mu_s = 0$. The true vacuum potential (plotted on the right) is also reported to allow for a direct comparison of the two cases. Bottom Row: Sketched phase diagram in the $T - \theta_l$ plane for $\mu_s = \mu_l$ (left) and for $\mu_s = 0$ (right). Solid lines indicate the RW lines, while the dashed lines corresponds to the analytic continuation of the pseudo-critical line. In the $\mu_s = 0$ case the exact location of the RW-like lines, apart from the one at $\theta_l = \pi$, is temperature dependent and known analytically only in the high T limit.

3.3 General framework and numerical setup

Let us now sketch the structure of the phase diagram at imaginary μ_B . This has already been done in the introduction, by considering the effective degrees of freedom at work in the different regimes; now we will proceed through an analysis of the properties of the path integral. In the presence of a purely baryon chemical potential (i.e. $\mu_Q = 0$ and $\mu_S = 0$), one has $\mu_u = \mu_d = \mu_s \equiv \mu_q = \mu_B/3$. When μ_q is purely imaginary, its introduction is equivalent to a global rotation of fermionic boundary conditions in the temporal direction by an angle $\theta_q = \text{Im}(\mu_q)/T$, therefore one expects at least a 2π -periodicity in θ_q ($2\pi N_c$ in θ_B). However, the actual periodicity is $2\pi/N_c$, since a rotation of the fermionic boundary conditions by that angle is equivalent to a center transformation on the gauge fields, hence it can be reabsorbed without modifying the path integral [50].

Numerical simulations show that such a periodicity is smoothly realized at low temperatures [101, 102, 103, 104]. At high T , instead, since the Polyakov loop P (trace of the temporal Wilson line normalized by N_c , averaged in space) enters the fermionic determinant expansion multiplied by $\exp(i\theta_q)$, the value of θ_q selects the true vacuum among the three different minima of the Polyakov loop effective potential, which are related to each other by center transformations. Hence, phase transitions occur as θ_q crosses the boundary between two different center sectors, i.e. for $\theta_q = (2k+1)\pi/N_c$ and k integer (in which case θ_B is an odd multiple of π), where $\langle P \rangle$ jumps from one center sector to the other [50]; the phase of P can serve as a possible order parameter in this case. The T - θ_q phase diagram then consists of a periodic repetition of first order lines (RW lines) in the high- T regime, which disappear at low T . Therefore they have an endpoint, or a triple point, at some temperature T_{RW} , where an exact Z_2 symmetry breaks spontaneously. A schematic view of the diagram is reported in Fig. (3.2, lower panel).

An alternative order parameter is represented by any of the quark number densities (where $q = u, d, s$)

$$\langle n_q \rangle \equiv \frac{1}{V_4} \frac{\partial \log Z}{\partial \mu_q} \quad (3.20)$$

where V_4 is the four dimensional lattice volume. Since Z is an even function of μ_B , each $\langle n_q \rangle$ is odd and, for purely imaginary μ_B , it is purely imaginary as well. Invariance under charge conjugation, or alternatively oddness and the required 2π periodicity in θ_B , implies that $\langle n_q \rangle$ vanishes for $\theta_B = \pi$ or integer multiples of it, unless a discontinuity takes place at such points, in correspondence of a spontaneous breaking of charge conjugation invariance. This is exactly what happens at the RW lines, so that a non-zero $\langle n_q \rangle$ signals the onset of the RW transition.

In the following, it will be convenient to consider one particular RW line, corresponding to $\theta_q = \pi$, for which the imaginary part of the Polyakov loop, together with the imaginary part of the quark number density, can be taken as an order parameter. We could in principle define the susceptibility of the imaginary part of the Polyakov loop as

$$\tilde{\chi}_{\text{Im } P} \equiv N_t N_s^3 (\langle (\text{Im} P)^2 \rangle - \langle \text{Im} P \rangle^2), \quad (3.21)$$

but this definition has a couple of shortcomings. First of all, the autocorrelation time of $\text{Im } P$ above the transition T_{RW} is very large, because at high temperature the probability of tunnelling between the configurations where $\text{Im } P > 0$ and $\text{Im } P < 0$ becomes extremely low. This can of course be fixed by exploiting the Z_2 symmetry of the system, imposing the correct result $\langle \text{Im } P \rangle = 0$ in Eq. 3.21. But of course, the susceptibility of the order parameter as defined in this way would not show a peak at T_{RW} : the issue here is exactly the same as the problem that one faces when studying the Ising model at low temperature.

A way out is to consider $|\text{Im } P|$ as the order parameter. Noting that $\langle |\text{Im } P| \rangle \sim |\langle \text{Im } P \rangle|$ both in the high temperature and in the low temperature phase¹², it is reasonable to conclude that the susceptibility of $|\text{Im } P|$ will have a peak at the transition.¹³ The order parameter susceptibility is then defined as

$$\chi_{|\text{Im } P|} \equiv N_t N_s^3 (\langle (\text{Im} P)^2 \rangle - \langle |\text{Im} P| \rangle^2), \quad (3.22)$$

¹² Actually, when $\text{Im } P \sim 0$ (for $T < T_{RW}$) we have $\langle \text{Im } P \rangle = 0$, while $\langle |\text{Im } P| \rangle > 0$. This is actually a finite size effect (the smaller the spatial volume of the lattice, the larger the fluctuations of P). Note that P represents the value averaged in space and $\langle \dots \rangle$ represents the Montecarlo average.

¹³ This would be actually equivalent to use Eq.3.21 in an infinite volume with our current Montecarlo algorithm: then, ergodicity would be lost and we would end up with $\langle |\text{Im } P| \rangle = |\langle \text{Im } P \rangle|$ even at high temperature.

	ν	γ	γ/ν	$1/\nu$
3D Ising	0.6301(4)	1.2372(5)	~ 1.963	~ 1.587
1 st Order	1/3	1	3	3
Tricritical	1/2	1	2	2

TABLE 3.1: The critical exponents relevant for this study (see e.g. [156, 163, 175])^a.

where N_s (N_t) is the spatial (temporal) size in lattice units. The susceptibility $\chi_{|\text{Im } P|}$ is expected to scale, moving around the endpoint at fixed N_t and θ_q , as

$$\chi_{|\text{Im } P|} = N_s^{\gamma/\nu} \phi(tN_s^{1/\nu}), \quad (3.23)$$

where $t = (T - T_{\text{RW}})/T_{\text{RW}}$ is the reduced temperature, which is proportional to $(\beta - \beta_{\text{RW}})$ close enough to the critical point. That means that the quantity $\chi_{|\text{Im } P|}/N_s^{\gamma/\nu}$, measured on different spatial sizes, should lie on the same curve when plotted against $(\beta - \beta_{\text{RW}})N_s^{1/\nu}$. Alternatively, repeating the same reasoning exposed above for the Polyakov loop, we will consider also the susceptibility of the absolute value of the imaginary part of the quark number density, which is defined, for every flavor q , by

$$\chi_q \equiv N_t N_s^3 (\langle |\text{Im}(n_q)|^2 \rangle - \langle |\text{Im}(n_q)| \rangle^2), \quad (3.24)$$

and is expected to show a scaling behavior as in Eq. (3.23).

3.4 Numerical Results for physical quark masses

In this Section we present our numerical results, starting from an analysis of the critical behavior around the RW endpoint transition, in order to assess its order and universality class on lattices with $N_t = 4, 6$. Then we will consider also lattices with $N_t = 8, 10$ in order to provide a continuum extrapolated value for T_{RW} .

Since we are interested in studying the behavior near the phase transition, long time histories are required, to cope with the critical slowing down (see Fig. 3.3); for the couplings around the critical value, we used $\sim 40 - 50K$ unit-length trajectories for each run when performing the finite size analysis.

3.4.1 Finite size scaling and universality class of the transition

The effective theory associated with the spontaneous breaking of the charge conjugation at finite temperature is a three dimensional theory with Z_2 symmetry, so the transition can be either first order or second order in the three-dimensional Ising universality class. A tricritical scaling is in principle possible as well; however the tricritical point is just a single point at the boundary of first and second order regions. As a consequence (apart from the unlikely case of being exactly on it) tricritical indices can be observed only as scaling corrections, the ultimate large volume behavior being either first order or Ising 3d [131, 156, 173, 174]. The critical indices that will be used in the following are reported for convenience in Table 3.1.

We will now present the finite size scaling analysis performed to identify the nature of the transition on lattices with temporal extent $N_t = 4$ and 6. As previously discussed, we adopt two different order

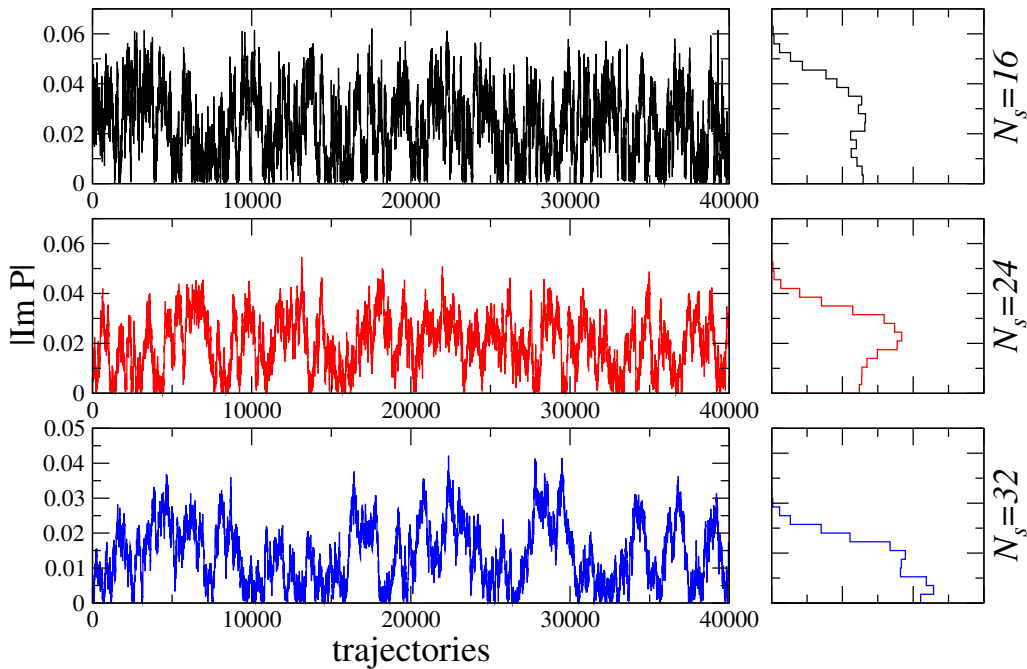


FIGURE 3.3: Monte Carlo histories of $|\text{Im } P|$ for $N_t = 4$ and the β values closest to the peak of $\chi_{|\text{Im } P|}$, showing the peculiar features expected near a second order transition: the increase of the autocorrelation time and the absence of a double peak structure in the histogram.

parameters, namely the imaginary part of the average Polyakov loop and the quark number density; the former turned out to have smaller corrections to scaling, so we will start our analysis from the study of the susceptibility $\chi_{|\text{Im } P|}$ defined in Eq. (3.22).

Fig. 3.4 shows $\chi_{|\text{Im } P|}$ obtained on $N_t = 4$ lattices and rescaled according to Eq. (3.23), using alternatively the critical indices of the $3d$ Ising universality class or those corresponding to a first order transition (the values used for the critical coupling are the ones reported in Table 3.2). Using $3d$ Ising indices the results on different volumes collapse on top of each other, whereas this is not the case using first order indices, which strongly indicates that the transition is second order for $N_t = 4$. Note that, since we are performing simulations on a line of constant physics, the mass parameters change with β ; it is thus not possible to use standard reweighting methods [176, 177]. In Fig. 3.5 we repeat the same analysis using the Polyakov loop measured on lattices with temporal extent $N_t = 6$. Again, the $3d$ -Ising universality class appears to describe the scaling of the susceptibility of the Polyakov loop significantly better than a first order, although larger corrections to scaling are present with respect to the $N_t = 4$ case.

A confirmation of the previous analysis comes from the study of the fourth-order Binder ratio, which in our case is defined as

$$B_4 = \frac{\langle (\text{Im } P)^4 \rangle}{\langle (\text{Im } P)^2 \rangle^2}. \quad (3.25)$$

It is easy to show that, in the thermodynamical limit, $B_4 \rightarrow 3$ in the absence of a phase transition, while $B_4 \rightarrow 1$ if a first order transition is present. At second order transitions B_4 assumes non-trivial values, which are characteristic of the universal critical behavior associated with the transition [161, 162, 163]. For the particular case of the three-dimensional Ising universality class the critical value is $B_4 = 1.604(1)$, see Ref. [175]. From these general properties the following simple procedure follows to locate the critical endpoint of a line of first order transition: study the behavior of B_4 as a function of the coupling for

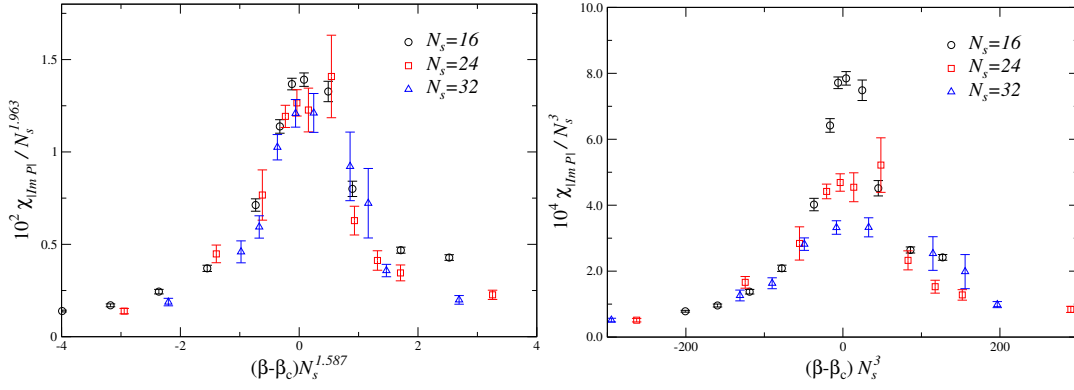


FIGURE 3.4: Susceptibility of the imaginary part of the Polyakov loop on $N_t = 4$ lattices rescaled using the 3d Ising critical indices (left) or the first order ones (right).

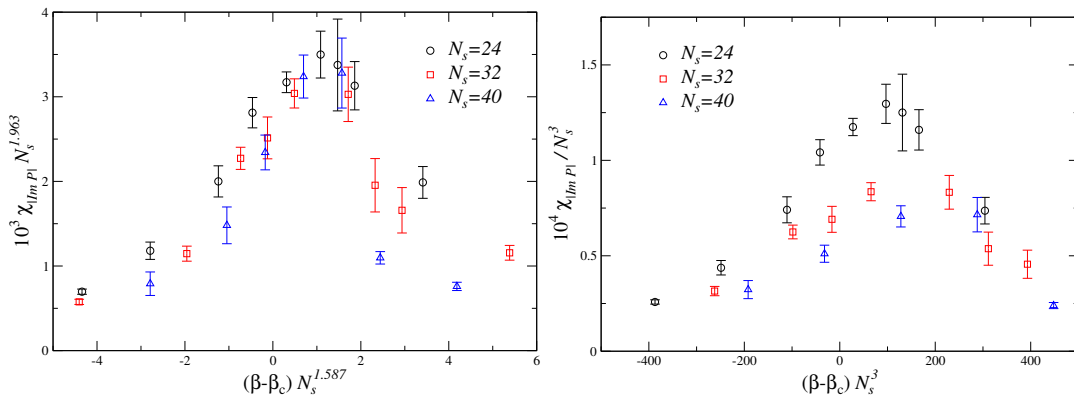


FIGURE 3.5: Susceptibility of the imaginary part of the Polyakov loop on $N_t = 6$ lattices rescaled using the 3d Ising critical indices (left) or the first order ones (right).

different values of the lattice size; the endpoint coupling value will correspond (up to scaling corrections) to the crossing point of these curves.

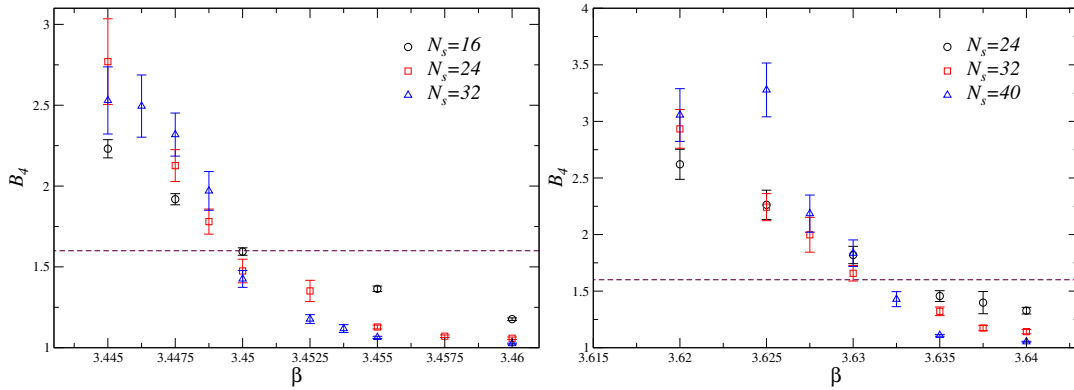


FIGURE 3.6: Binder fourth order ratio of the Polyakov loop imaginary part computed on $N_t = 4$ lattices (left) and $N_t = 6$ lattices (right). The horizontal line denotes the value expected for a second order transition of the 3d Ising universality class.

In Fig. 3.6 we show the values of B_4 in a neighborhood of the critical coupling at three different volumes both on $N_t = 4$ and $N_t = 6$ temporal extent. The behavior of the Binder ratio as a function of β is clearly the one expected at a critical endpoint and the value at the crossing point is in reasonable agreement with that expected for a transition of the 3d Ising universality class, while a first order is clearly excluded.

The same conclusions are obtained by studying the susceptibility of the u quark number density defined in Eq. (3.24), although in this case the scaling corrections appear to be larger. As an example in Fig. 3.7 we show the behavior of χ_u on $N_t = 4$ lattices, rescaled according to Eq. (3.23): again, the 3d-Ising critical indices are favored. The case of the strange susceptibility χ_s is similar, as well as the $N_t = 6$ case.

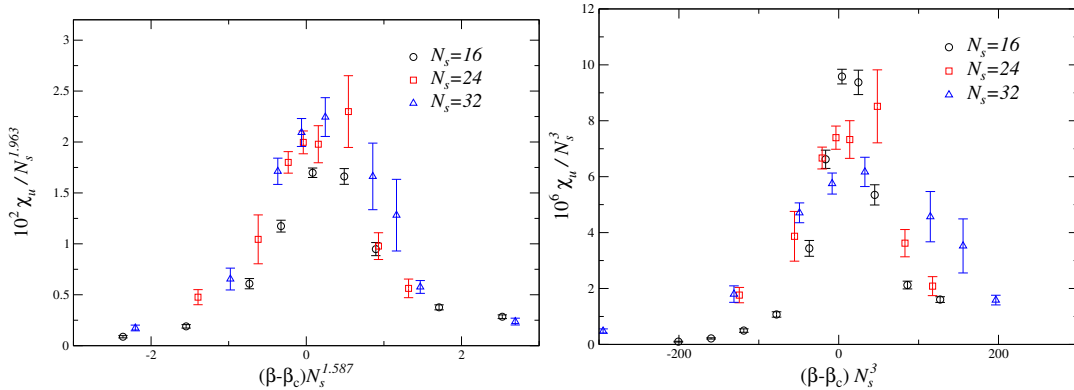


FIGURE 3.7: Disconnected susceptibility of the light baryon number computed on $N_t = 4$ lattices and rescaled with the critical exponents of the 3d Ising universality class (left) or corresponding to a first order transition (right).

3.4.2 Critical temperature: continuum extrapolated value

Having established that the RW-transition is second order for physical quark masses and for lattices with temporal extent $N_t = 4$ and 6, we now proceed to estimate the continuum value of T_{RW} . To this purpose, simulations have been performed also on lattices with $N_t = 8$ and 10, considering a limited number of spatial volumes (one or two) per simulation setup.

The pseudocritical value of the coupling has been determined for each lattice size by estimating the position of the maximum of $\chi_{|\text{Im } P|}$ and χ_u . To this purpose, we have fitted the peak with a Lorentzian function:

$$f(\beta) = \frac{a}{1 + (\beta - \beta_{pc})^2 / c^2}. \quad (3.26)$$

The results for the large volume limit of β_{pc} , denoted by β_c , are reported in Table 3.2; the error also takes into account the systematics related to the choice of the fit range. The volume dependence of the pseudocritical coupling is very mild for lattices with aspect ratio 4 or larger, with variations at the level of 0.1% in terms of β (which become 0.5% in terms of temperature), as can be seen in Fig. 3.8 for the case of the $N_t = 4$ lattices. The pseudocritical couplings determined by using $\chi_{|\text{Im } P|}$ or χ_u have *a priori* to coincide only in the thermodynamical limit, however in all the cases the differences between the two determinations are well below 0.1% and, with the exception of the lattice 4×16^3 , they are compatible with each other at one standard deviation.

In order to convert the critical temperatures to physical units we used the lattice spacings values reported in Tab. 3.2, which are obtained by a spline interpolation of the results presented in [55, 56, 57]. The systematic uncertainty on these lattice spacings is 2–3% [55, 56, 57] and this is by far the largest source of error in the final temperature estimates. The results obtained at the different N_t are plotted in Fig. 3.8 together with the linear fit in $1/N_t^2$, which describes well the approach to the continuum limit and from which we extract the value 208(4) MeV for the continuum limit of the RW endpoint temperature. Using

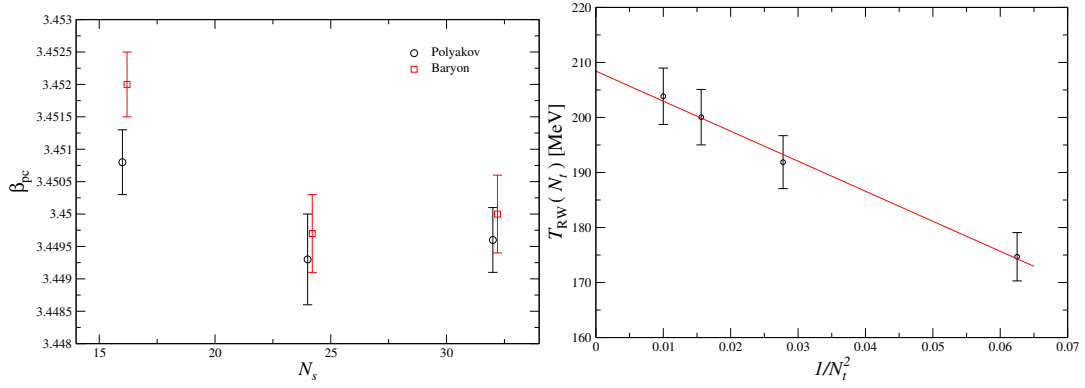


FIGURE 3.8: **Left:** Thermodynamical limit of the pseudocritical coupling determined on $N_t = 4$ lattices from the maxima of $\chi_{|\text{Im } P|}$ and χ_B . **Right:** Continuum extrapolation of the critical temperature.

N_t	β_c	N_s	a (fm)
4	3.4498(7)	16, 24, 32	0.2424(6)
6	3.6310(15)	24, 32, 40	0.1714(3)
8	3.7540(25)	32, 40	0.1233(3)
10	3.8600(25)	40	0.0968(2)

TABLE 3.2: Critical values of the coupling for different lattice temporal extents N_t and corresponding values of the lattice spacing. The reported value of β_c is obtained taking into consideration only the largest value of the lattice spatial extent N_s , and the systematic uncertainties in both the polyakov loop susceptibility and the baryon number susceptibility maxima for $N_t = 4$, while for higher values of N_t only the maximum of the baryon number susceptibility at largest spatial volume has been considered. Only the statistical error of the lattice spacing is reported in the table, the systematic error is about 2 – 3% [55, 56, 57].

as systematical error the difference between this value and the one obtained using just the three finer lattices, we get our final estimate $T_{\text{RW}} = 208(5) \text{ MeV}$.

3.4.3 Relation with the pseudocritical chiral transition line

An interesting issue that remains to be investigated is the relation between the RW endpoint and the chiral transition. In particular, the question can be posed in the following way: does the pseudocritical line really get to the RW endpoint, as assumed in Fig. 3.2 and as suggested by early studies on the subject?

A number of investigations appeared recently, reproducing the pseudocritical line for imaginary chemical potentials at or close to the physical point and with the setup of chemical potentials relevant to the RW endpoint, i.e. $\mu_s = \mu_l = \mu_B/3$, see Refs. [113, 115] and also Chapter 2. A possible way to approach the question is to try extrapolating the location of the pseudocritical line up to $\theta_B = \pi$ on the basis of those determinations. To this aim we considered results for $T_c(\theta_B)$ obtained in the first part of this Thesis on $N_t = 8$ lattices and adopting the same discretization used in the present study. In Fig. 3.9, we present two different extrapolations of such data, corresponding to the fit ansatz

$$T_c(\theta_B) = T_c(1 + \kappa \theta_B^2 + b \theta_B^4 + c \theta_B^6) \quad (3.27)$$

with or without the sixth order term included (a simple linear dependence on θ_B^2 has already been excluded, see the previous Chapter). In both cases one gets reasonably close, within errors, to the RW endpoint.

Of course, the issue can be checked also directly, by determining the location of the pseudocritical line exactly at $\theta_B = \pi$. To that aim, in Fig. 3.9 we plot the renormalized light chiral susceptibility, defined in Eq. (2.12) for lattices with temporal extent $N_t = 6, 8$, together with the positions of the RW endpoint as previously determined on the same lattices. It is clearly seen that the location of the maxima of the chiral susceptibility is compatible with the position of the RW endpoints. For instance for $N_t = 8$ and $N_s = 32$ we obtain, by fitting the chiral susceptibility to a Lorentzian peak, $\beta_c = 3.749(3)$, which is at just one standard deviation from the RW endpoint coupling reported in Table 3.2.

We can thus confirm, within present errors, evidence that the RW endpoint is located at a point where the analytic continuation of the pseudocritical line and the RW first order line meet each other. To conclude, based on this evidence, we have performed a final fit, including terms up to the sixth order in θ_B^2 , which includes the RW endpoint as a part of the pseudocritical line. The result is the dashed line reported in Fig. 3.9, which has been continued also to the other center sectors, so as to reproduce a realistic version (i.e. for $N_f = 2 + 1$ QCD with physical quark masses, even if just for $N_t = 8$) of the phase diagram sketched in Fig. 3.2.

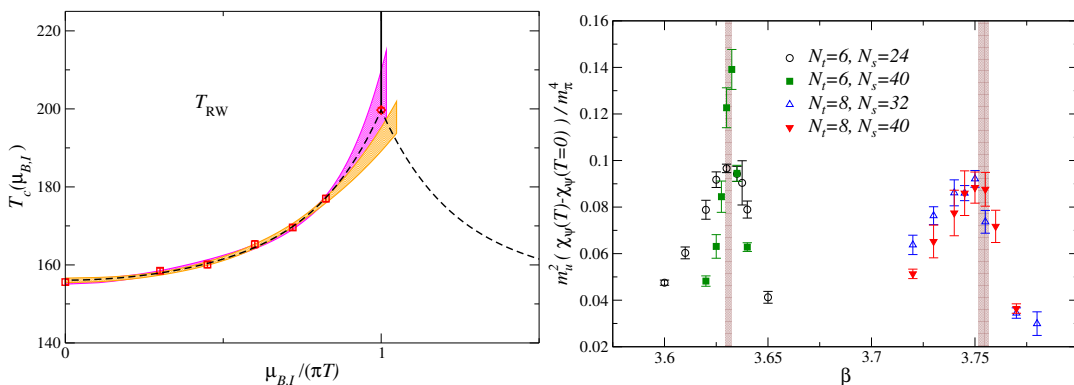


FIGURE 3.9: **Left:** Phase diagram of QCD in the presence of an imaginary baryon chemical potential obtained from numerical simulations on $N_t = 8$ lattices alone. Bands denote fits to polynomials in μ_B^2 : the orange (longer) band is obtained using terms up to order μ_B^4 , the violet (shorter) one using up to μ_B^6 terms. **Right:** Renormalized light chiral susceptibility on $N_t = 6$ and 8 lattices. The vertical bands denote the position of the RW endpoint on lattices of the corresponding temporal extent.

3.4.4 Conclusions

We have investigated the properties of the RW endpoint by lattice simulations of $N_f = 2 + 1$ QCD with physical quark masses and making use of two different order parameters for the transition, namely the imaginary part of the Polyakov line and the imaginary part of the quark number density, which have led to consistent results.

The temperature of the endpoint, T_{RW} , has been determined at four different values of the lattice temporal extent, $N_t = 4, 6, 8, 10$, from which we have obtained a continuum extrapolated value $T_{RW} = 208(5)$ MeV, where the error includes both statistical and systematic contributions, stemming mostly from the determination of the physical scale. That leads to the estimate $T_{RW}/T_c = 1.34(7)$, where the error also takes into account

the systematics involved in the determination of T_c , originating both from the scale setting and from the difficulties in defining a critical temperature when no real transition is present. This ratio is significantly larger than the ones obtained in previous studies; indeed, with unimproved actions, unphysical quark masses and no extrapolation to the continuum limit, T_{RW} was typically found to be only about 10% larger than T_c . The larger value is partially due to the larger curvature κ , and partially to the more significant contribution from non-linear terms in μ_B^2 (see Eq. (3.27)) which are present in the case $\mu_u = \mu_d = \mu_s$ (see previous Chapter).

Regarding the order of the transition, our finite size scaling analysis provides evidence that a second order transition of the $3d$ -Ising universality class takes place, rather than a first order one, at least for $N_t = 4$ and $N_t = 6$ lattices. Our investigation has been performed at a fixed value of the pion mass, corresponding to its physical value $m_\pi \simeq 135$ MeV.

Previous studies on the subject, performed in the $N_f = 2$ theory with both staggered and Wilson fermions, have shown that the order of the transition changes as a function of m_π ; in particular, there are two tricritical pion masses, $m_\pi^{\text{tric.light}}$ and $m_\pi^{\text{tric.heavy}}$, and the transition is second order for $m_\pi^{\text{tric.light}} < m_\pi < m_\pi^{\text{tric.heavy}}$ and first order for lighter or heavier pion masses. The value of the heavy tricritical mass is typically well above the GeV scale. The lighter critical pion mass has been found to be $m_\pi^{\text{tric.light}} \sim 400$ MeV for standard staggered fermions on $N_t = 4$ lattices [131], and around 930 and 680 MeV for standard Wilson fermions on respectively $N_t = 4$ [54] and $N_t = 6$ [138] lattices. Given these results, even if we have studied just the physical value of the pion mass, we can conclude the following: for stout improved staggered fermions, one has $m_\pi^{\text{tric.light}} < 135$ MeV on both the $N_t = 4$ and $N_t = 6$ lattices. When compared to previous results, that demonstrates the presence of significant cut-off effects on the values of this tricritical mass, even when working at fixed N_t but with a different action. Moreover, based on the observed tendency of the tricritical mass to decrease with the increase of N_t , we suggest that $m_\pi^{\text{tric.light}}$ will be smaller than $m_\pi^{\text{phys}} = 135$ MeV in the continuum limit, so that the RW endpoint should be a second order transition in the continuum limit at the physical pion mass.

We must however remark that the mechanism driving the change of nature of RW endpoint transition, from second to first order as the pion mass decreases, is still unknown. If such a mechanism is related to the chiral properties of quarks, unexpected behaviors could occur as the continuum chiral symmetry group is fully recovered. This is known to happen, at least for staggered fermions, for lattice spacings well below those explored in the present study (see Ref. [178] for a recent investigation about this issue).

Let us spend a few words about what, in our opinion, future studies should clarify. First of all, one would like to check the second order nature of the RW endpoint at the physical point on finer lattices, i.e. for $N_t > 6$. Then, our study with stout improved staggered fermions should be extended to different values of the pion mass, in order to locate the values of the tricritical masses $m_\pi^{\text{tric.light}}$ and $m_\pi^{\text{tric.heavy}}$ and possibly extrapolate them to the continuum limit. Such a program would clarify the universal properties of the only critical point of strong interactions (in the presence of finite quark masses) that one can predict *a priori*, based on the known symmetries of QCD. Preliminary results concerning the chiral limit will be presented in the next section.

Finally, another open issue regards the relation of the RW critical point to those predicted in well defined limits of QCD. The relation to the deconfinement transition present in the quenched case is obvious, since the two transitions trivially coincide in this case and are both related to center symmetry. The relation to the chiral transition in the limit of massless quarks is far less trivial. Suppose to move (varying the temperature) along the line $\theta_B = \pi$ in the presence of massless quarks; in principle one expects two

am_l	0.003	0.0015	0.00075
N_s	16, 20, 24, (32)	16, 20, 24, (32)	16, 20, 24, 28
N_t	4 (48)	4 (48)	4

TABLE 3.3: The combination of the value of the light quark mass m_l and number of lattice sites along the spatial direction N_s that have been used in the simulations towards the chiral limit. We also have run simulations on large lattices for $T = 0$ simulations ($32^3 \times 48$). The value of am_l for physical m_π range from $am_l \simeq 0.007$ for $\beta = 3.40$ to $am_l \simeq 0.004$ for $\beta = 3.50$.

different critical temperatures, one at which chiral symmetry is restored, T_χ , and one at which the Z_2 charge conjugation symmetry spontaneously breaks, T_{RW} . What is the relation between T_χ and T_{RW} ? Our present results at finite quark masses prove that the location of the peak of the renormalized chiral susceptibility coincides, within errors, with T_{RW} , see Fig. 3.9, so that the analytic continuation of the pseudocritical line meets the RW line at its endpoint. However, in order to obtain a definite answer, the issue should be explored while approaching the chiral limit.

3.5 Towards the chiral limit

In this section we present some preliminary work on the Roberge-Weiss transition in the $N_f = 3$ chiral limit, which is approached by keeping the ratio between the light and strange bare quark masses fixed to the physical value ~ 28.15 . Data reported here has been produced with the program briefly described in Appendix A. Our numerical setup is similar to the one described in the first part of this Thesis, but while in that case our exploration was carried out for physical quark masses with a scan in $\mu_{I,B}$, we here aim to do a parameter scan in the mass while keeping the chemical potential for all quarks fixed to $i\pi T$. The starting point of this work are the results obtained for physical quark masses in the previous Section, where it was determined that for the same action used here, for physical values of the quark masses, at $N_t = 4$ and 6, the Roberge-Weiss transition is of the second order kind. We decrease the quark mass, and for each value of the quark masses we do a parameter scan in the inverse coupling β , which allows us to locate the transition temperature looking at the order parameter $|ImP|$. For the same values of the quark masses we repeat these steps on larger lattices in order to perform a finite size scaling analysis. Since we are approaching the $N_f = 3$ chiral limit and in that limit the chiral phase transition is expected to be first order, and the Roberge-Weiss has been empirically found to be stronger than the chiral one, it can be expected that below a certain value of m_l the Roberge-Weiss transition will become first order. A significant achievement here would be to locate such value of m_l , which is related to the tricritical pion mass $m_\pi^{tric:l}$. At the time of writing, only data for $N_t = 4$ are available.

3.5.1 Results for finite size scaling

In the following figures (Figs.3.10, 3.11 and 3.12) the quantity $\chi_{|ImP|}$ (See Eq. 3.22) is shown, which is a measure of the fluctuation of the order parameter ImP . In the figures this quantity, and the inverse coupling β , are rescaled according to the critical exponents of first order (left figure) or second order in the Ising 3D universality class (right figure). Rescaling according to tricritical indices is not reported, for the simple reason that with the precision given we are not able to distinguish between the tricritical and second order 3D Ising cases. The results for the 3 different mass setups are displayed. The continuous bands have been produced by making use of the multi-histogram reweighting method [177], and the error

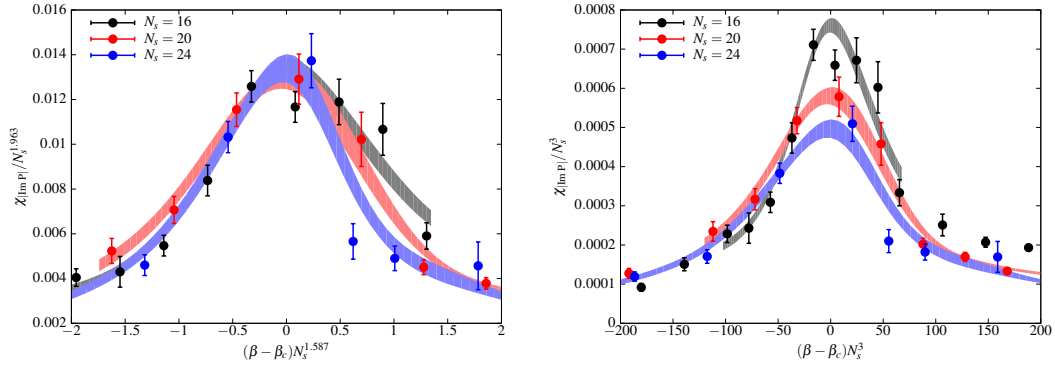


FIGURE 3.10: Collapse plots for the Polyakov loop susceptibility, at $m_l a = 0.003$. **Left** : Second order Ising 3D scaling. **Right** : First order scaling.

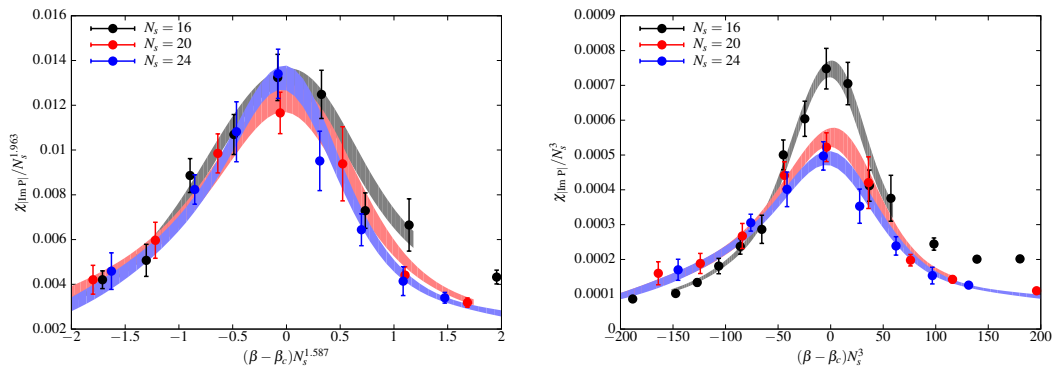


FIGURE 3.11: Collapse plots for the Polyakov loop susceptibility, at $m_l a = 0.0015$. **Left** : Second order Ising 3D scaling. **Right** : First order scaling.

bands have been obtained by making use of the jackknife technique associated to the multi-histogram reweighting. It must be noted that, while for $am_l = 0.003$ and $am_l = 0.0015$ the scaling seems to be consistent with the second order hypothesis, in the $am_l = 0.00075$ case the $L = 24$ and $L = 28$ might agree better with a first order hypothesis. The whole picture for $am_l = 0.00075$ could also be explained by the hypothesis that, for this value of the quark mass, we are close to the tricritical point, on the first order side: a tricritical scaling would indeed fit the data on the smaller lattices, but at larger lattices the true first order scaling would become evident. However, more data and possibly data coming from larger lattices are needed to clarify this issue.

A second order of considerations is also related to the rooting procedure. It has indeed been shown that the chiral limit and the continuum limit may not commute when rooting is used. Besides the evidences of large cutoff effects, seen e.g. in [54, 138] (but also in [37]), this fact stresses the need to study finer lattices. Nonetheless, comparing with the results obtained with unimproved staggered fermions on $N_t = 4$ lattices for $N_f = 2$ [131], it is already clear that in the current setup the light tricritical mass is much smaller.

The results for the Binder cumulant B_4 are shown in Fig. 3.13. Data for the Binder cumulant should respect the scaling law

$$B_4(\beta) = 1.604 + c_1 x + O(x^2) \quad (3.28)$$

where $x = (\beta - \beta_c) N_s^{1/\nu}$ and 1.604 is the expected value of B_4 at crossing for the Ising 3D universality class. A fit to Eq. (3.28) does not give completely satisfactory results: maybe lattices with larger spatial

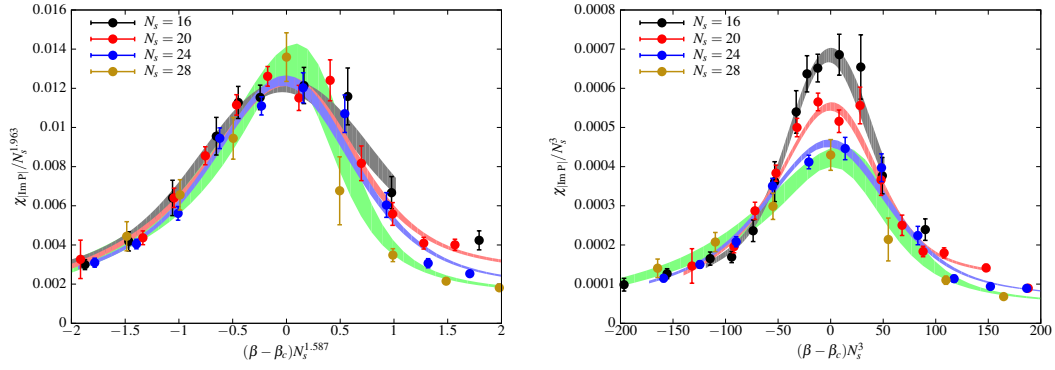


FIGURE 3.12: Collapse plots for the Polyakov loop susceptibility, at $m_l a = 0.00075$. **Left** : Second order Ising 3D scaling. **Right** : First order scaling.

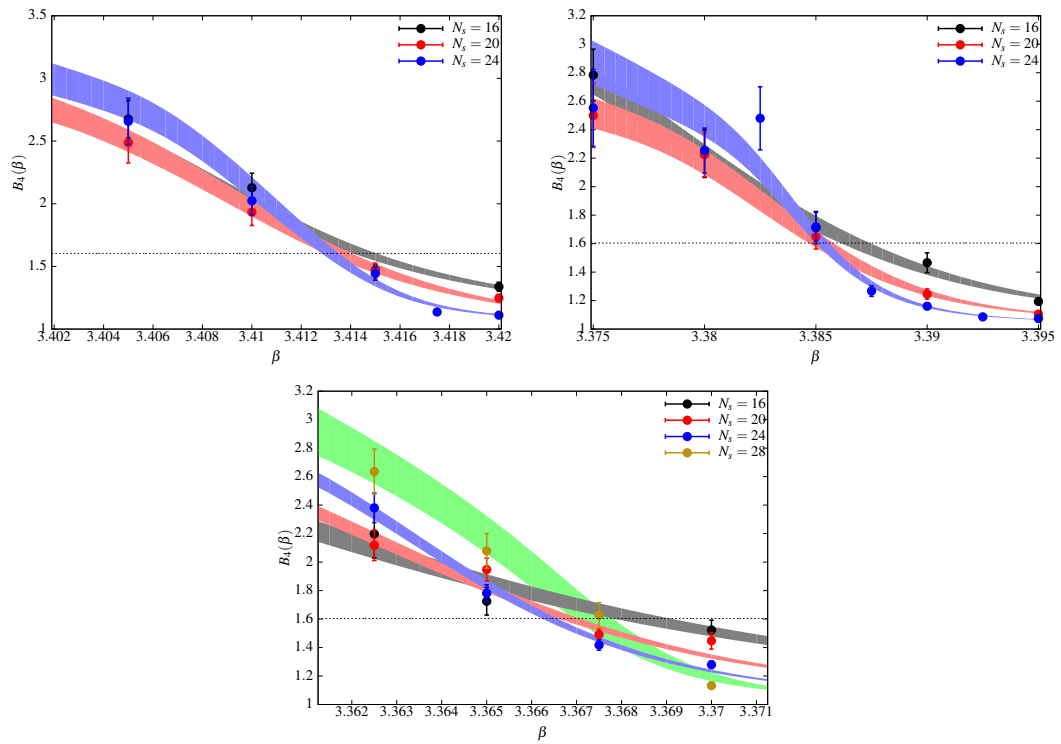


FIGURE 3.13: Binder cumulant for the imaginary part of the Polyakov loop. Top left: $m_l a = 0.003$. Top Right: $m_l a = 0.0015$. Bottom left: $m_l a = 0.00075$. In the case of a second order transition, if the spatial volume is large enough so that the scaling region is reached, the bands should cross at the universal value $B_4(\beta_c) \sim 1.604$.

dimension N_s are still needed, likely because of the very small quark masses adopted.

3.5.2 The light chiral susceptibility at the RW transition

It is also interesting to look at the chiral properties in the correspondence of the transition. At the time of writing it is not possible to perform a proper renormalization for the chiral susceptibility as it has been done for the data at physical mass, because part of the necessary data is missing. In Fig. 3.14 the maximum values of the chiral susceptibility are shown. Even if the order parameter of the Roberge-Weiss transition has no clear relation with chiral symmetry, it can be worth noting that the finite size scaling of

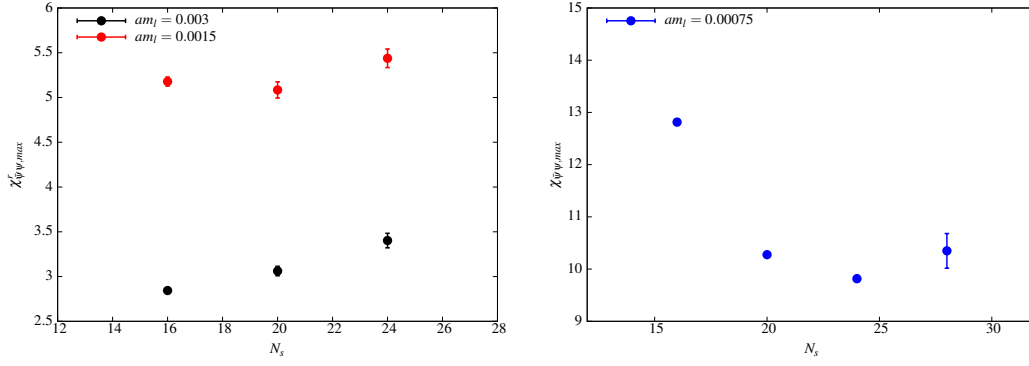


FIGURE 3.14: Left: Maxima of the additively renormalized chiral susceptibility for $am_l = 0.003$ and $m_l = 0.0015$. Right: Maxima of the bare chiral susceptibility for $am_l = 0.00075$. Both these quantities are in lattice units.

the chiral susceptibility maxima seems at the time more compatible with a first order transition than with a second order transition, at least for large volumes. Indeed, speaking of the bulk susceptibility, defined as in Eq. 2.12, in the case of a second order transition in the 3D Ising universality class the maxima should decrease as $N_s^{\gamma/\nu-3} \sim N_s^{-1.03}$, while in the first order case the maxima should remain constant.

We also report that the values of the inverse coupling β at the maxima of the chiral susceptibility are also largely compatible with the corresponding maxima of the Polyakov loop susceptibility.

Chapter 4

Conclusions and Outlooks

In this Thesis the phase diagram of QCD for imaginary chemical potential has been studied. By making use of analytic continuation, we finally managed to give a reliable estimate of the curvature of the (pseudo) critical line of QCD at *real* baryon chemical potential, keeping under control most of the systematics involved, coming from the definition of the critical line (i.e., the definition of the pseudocritical temperature as a function of the chemical potential), from the effect of the strange quark chemical potential and from the continuum limit procedure. We obtained the value $\kappa = 0.0135(15)$. While it is reassuring that the results are compatible with the ones from the latest works appeared in literature (which use as well the method of analytic continuation from imaginary chemical potential), it must be noted that there appears to be a discrepancy with older determinations obtained with the Taylor expansion method. As the work presented here suggests, this discrepancy could be partially explained by methodological differences in the choice of the observables and in the definition of the critical temperature used in those works. It must be noted, though, that the recent works based on analytic continuation are quite more “mature” than the previous ones based on Taylor expansion, so it would be reasonable to carry over a study of the subject with Taylor expansion the same level of accuracy reached with analytic continuation. This would allow to have yet another confirmation of these results, excluding unforeseen systematic issues in analytic continuation.

Of course, the general structure of the QCD phase diagram at *large* finite density remains unknown and theoretically not understood. From the experimental side, a number of facilities have been planned and are becoming operational to study different regions of the phase diagram, especially at very large baryon chemical potential. Unfortunately, at the moment the theoretical tools to study that region of the phase diagram are not mature enough to provide reliable results, but many techniques are being developed that could eventually be used to tame the sign problem. It must be also noted that the bridge connecting equilibrium physics with the experimental observables is extremely complex, and still deserves more study and development.

The second part of this Thesis concerned the Roberge-Weiss transition. We have studied it for physical quark masses, locating the critical temperature in the continuum limit ($T_{RW} = 208(5)$ MeV) and determining the order of the transition, which appears to be of the second order kind. An interesting issue is the determination of the properties of the Roberge-Weiss transition as a function of the quark masses. This topic has been studied recently by making use of different discretizations and on $N_f = 4$ and 6 lattices. In the case of unimproved Wilson fermions, a large cutoff dependence of both the upper and lower tricritical

mass has been found by other groups. We decided to approach the chiral limit keeping the ratio between the light and the strange bare quark masses constant and equal to the one at the physical point. Our preliminary results for $N_t = 4$ do not show any clear evidence that the tricritical mass is contained in the mass interval we have explored. However, we established that the tricritical mass is much smaller than the one found in previous works with two flavors of unimproved staggered fermions on lattices with the same temporal extension N_t . It is anyway expected that cutoff effects will be important: for this reason, a natural and necessary next step is to study lattices with larger temporal extensions, besides increasing statistics in the existing datasets.

Appendix A

Implementation of a full dynamical fermions Monte Carlo with Hybrid parallelism (OpenAcc and MPI)

A.1 Numerical challenges of Lattice QCD

LQCD uses the Feynman path-integral quantization and approximates the infinite dimensional path-integral by a finite dimensional integral: continuous space-time is replaced by a finite lattice of sizes L_t, L_x, L_y, L_z and lattice spacing a . In order to maintain gauge invariance, the variables $U_\mu(n)$ associated with the gauge fields are elements of the $SU(3)$ group and live on the links of the lattice; the quark fields $\psi(n)$ live on the lattice sites and transform under the gauge group as 3-dimensional complex vectors[179]. The fundamental problem of LQCD is the evaluation of expectation values of given functions of the fields, $O[U]$, that is integrals of the form

$$\langle \hat{O} \rangle = \frac{1}{Z} \int \mathcal{D}U O[U] \det(M[U]) e^{-S_g[U]}, \quad Z = \int \mathcal{D}U \det(M[U]) e^{-S_g[U]}; \quad (\text{A.1})$$

the exponent S_g is the discretization of the action of the gauge fields (usually written as a sum of traces of products of $U_\mu(n)$ along closed loops) and $\det(M)$ describes the gluon-quark interaction. Here, $M[U]$ is a large and sparse structured matrix (i.e. containing both space-time and color indexes) which is the discretization of the continuum fermion operator $M \sim mI + D$ where m is the fermion mass, multiplying the identity operator, and D is the Dirac operator, which is constructed in terms of covariant derivatives. The integral in $\mathcal{D}U$ extends over all the $U_\mu(n)$ variables on the lattice using the Haar measure of $SU(3)$. Eq. (A.1) refers to a single quark species (flavor); in the realistic case of multiple flavors¹, one has to introduce a separate determinant for each flavor.

This formulation makes contact with a standard problem in statistical mechanics: importance sampling of the distribution $\det(M[U]) e^{-S_g[U]}$. What is non-standard is the form of this distribution and in particular

¹At present, we have experimental evidence of 6 different flavors in Nature, usually named with the letters u, d, s, c, b, t and ordered by increasing quark mass. In a realistic simulation, one usually takes into account the first 3 (or 4, at most) flavors, since the heaviest species give a negligible contribution to the low-energy dynamics of the theory.

the presence of the determinant. The best strategy devised so far to cope with this problem is to introduce the so called pseudo fermion fields[180] ϕ and rewrite the integral as follows:

$$\int \mathcal{D}U O[U] \det(M[U]) e^{-S_g[U]} \propto \int \mathcal{D}U \mathcal{D}\phi O[U] \exp(-S_g[U] - \phi^\dagger M[U]^{-1} \phi) ; \quad (\text{A.2})$$

the action is still a non-local function of the field variables, but the computational burden required for the solution of a large sparse linear system is much lower than the one needed for the computation of its determinant.

The explicit form of $S_g[U]$ and $M[U]$ is not fully determined, as these functions only have the constraint to go over to the correct continuum limit as the lattice spacing goes to zero. Much in the same way as several discretization schemes exist for the numerical solution of a partial differential equation, several discretization schemes of the QCD action exist. Here, we consider a specific state-of-the-art discretization, the tree-level Symanzik improved action[5, 6] for the gauge part and the stout-improved[17] ‘‘staggered’’ action for the fermion part. Staggered actions have a residual degeneracy, that has to be removed by taking the 4–th root of the determinant. So, Eq. (A.2) becomes in the staggered case

$$\int \mathcal{D}U \mathcal{D}\phi O[U] \exp(-S_g[U] - \phi^\dagger M[U]^{-1/4} \phi) . \quad (\text{A.3})$$

A.1.1 Why LQCD is a computational grand challenge

The physical system that one would like to simulate by the lattice box has a characteristic physical length ξ , which is of the order of 10^{-15} m (the size of a hadron). In order to reduce systematic effects related to discretization and to the finite box size, one would like that, at the same time, the lattice spacing a be much smaller, and the box size La much larger than ξ , i.e. $a \ll \xi \ll La$. Making the reasonable approximation that \ll translates into one order of magnitude means that the number of sites in each direction should be $\simeq 10^2$; the corresponding fermion matrix, considering also internal (e.g., color) indexes, has a dimension slightly exceeding $10^8 \times 10^8$; note that it is a sparse matrix, since the discretization of the Dirac operator D connects only neighbor lattice sites. In finite temperature simulations the size of the lattice is typically smaller, since in that case the temporal direction is shortened and equal to the inverse of the temperature, $1/T$.

The most computationally demanding task in the typical LQCD algorithm is the solution of a linear system involving the fermion matrix M . The numerical difficulty of this problem is fixed by the condition number of M , hence, since the highest eigenvalue is typically $O(1)$, by the smallest eigenvalue of M . Here the physical properties of QCD play a significant role: the eigenvalues of the Dirac operator are dense around zero, a property related to the so-called *spontaneous breaking of chiral symmetry*, so the smallest eigenvalue is set by am where m is quark mass. Since Nature provides us with two quark flavors (u and d quarks) whose mass is significantly lower (by two orders of magnitude) than other energy scales of the theory, typical values of am are very small, resulting in a bad condition number ($\kappa \gtrsim 10^5$ being a typical value). Also regarding this aspect, the situation becomes better when one is interested in the regime of very high temperatures, since in that case the spontaneous breaking of chiral symmetry disappears, the minimum eigenvalue of D is non-zero, and the condition number significantly improves.

A.1.2 Numerical algorithms for LQCD

In LQCD, the usual local updates adopted in statistical mechanics scale badly with the volume, as the action of Eq. (A.2) is non-local. This problem is partly solved by the Hybrid Monte Carlo (HMC) algorithm[181]; in HMC we associate fake conjugate momenta – entering quadratically in the action – to each degree of freedom of the system. For an $SU(3)$ gauge theory, momenta conjugate to the link variable are again 3×3 matrices $H_\mu(n)$ associated to each link of the lattice, this time living in the group algebra (hence Hermitian and traceless). Eq. (A.3) is rewritten as

$$\int \mathcal{D}U \mathcal{D}\phi \mathcal{D}H O[U] \exp\left(-\frac{1}{2}H^2 - S_g[U] - \phi^\dagger M[U]^{-1/4} \phi\right), \quad (\text{A.4})$$

where the momenta term is a shorthand to indicate the sum of $-\text{Tr}(H_\mu(n)^2)/2$ over the whole lattice. The update then proceeds as follows:

1. random Gaussian initial momenta H and pseudo fermions ϕ are generated;
2. starting from the initial configuration and momenta (U, H) , a new state (U', H') is generated by integrating the equations of motion (to some accuracy: precision is not paramount, but reversibility is);
3. the new state (U', H') is accepted with probability $e^{-\Delta S}$, where ΔS is the change of the total (i.e. included the momenta) action.

Step 2 is an unphysical evolution in a fictitious time and, under mild conditions on the numerical integration of the equations of motion, it can be shown to satisfy the detailed balance principle[181, 182], so it provides a stochastically exact way to estimate the integral in Eq. (A.2). The more time consuming steps of the update are the ones that involve the non-local term in the exponent of Eq. (A.2). In particular, the most time consuming single step of the whole algorithm is the solution of a linear system

$$M[U]\phi = b. \quad (\text{A.5})$$

This calculation is needed to compute the forces appearing in the equations of motion and also to evaluate ΔS , and one usually resorts to Krylov solvers. In the case of staggered fermions, corresponding to Eq. (A.3), it is customary to use the so-called Rational HMC (RHMC) algorithm[124, 125, 126], in which the algebraic matrix function appearing in Eq. (A.3) is approximated to machine precision by a rational function. In this case one replaces Eq. (A.5) by r equations (r is the order of the approximation adopted)

$$(M[U] + \sigma_i)\phi_i = b, \quad i \in \{1, \dots, r\}, \quad (\text{A.6})$$

where the real numbers σ_i are the poles of the rational approximations. These equations can again be solved by using Krylov methods: by exploiting the shift-invariance of the Krylov subspace it is possible to write efficient algorithms that solve all the equations appearing in (A.6) at the same time, using at each iteration only one matrix-vector product[183].

For most of the discretizations adopted in QCD (and in particular for the one we use), the matrix $M[U]$ can be written in block form

$$M = mI + \begin{pmatrix} 0 & D_{oe} \\ D_{eo} & 0 \end{pmatrix}, \quad D_{oe}^\dagger = -D_{eo}; \quad (\text{A.7})$$

matrices D_{oe} and D_{eo} connect only even and odd sites. It is thus convenient to use an even/odd preconditioning[184, 185]; in this case, Eq. (A.5) is replaced by:

$$(m^2 I - D_{eo}D_{oe})\varphi_e = b_e; \quad (\text{A.8})$$

φ_e is defined only on even sites and the matrix is positive definite (because of Eq. (A.7)), so we can use the simplest of the Krylov solvers: the conjugate gradient (or its shifted counterpart).

Over the years, many improvements of this basic scheme have been developed; these are instrumental in reducing the computational cost of actual simulations but their implementation is straightforward, once the basic steps of the “naive” code are ready. For this reason we will not discuss in the following the details of multi-step integrators[186, 187], improved integrators[188, 189, 190], multiple pseudo fermions[126] or the use of different rational approximations and stopping residuals in different parts of the HMC[125], even if our code uses all these improvements.

A.1.3 Data structures and computational challenges

Our most important data structures are the collection of all gauge variables $U_\mu(n)$ (elements of the group of $SU(3)$ matrices, one for each link of the four-dimensional lattice) and of the pseudo fermion fields $\phi(n)$ (3–dimensional complex vectors, one for each even site of the lattice when using the even/odd preconditioning). We also need many derived and temporary data structures, such as:

1. the configurations corresponding to different stout levels ($U_\mu^{(k)}(n)$, again $SU(3)$ matrices), used in the computation of the force (typically less than five stout levels are used) and the momenta configuration (which are 3×3 Hermitian traceless matrices);
2. some auxiliary structures needed to compute the force acting on the gauge variables, like the so called “staples” $\Sigma_\mu^{(k)}(n)$ and the $\Gamma_\mu(n)$ and $\Lambda_\mu(n)$ matrices[17]; $\Sigma_\mu^{(k)}(n)$ and $\Gamma_\mu(n)$ are generic 3×3 complex matrices and $\Lambda_\mu(n)$ are 3×3 Hermitian traceless matrices;
3. the solutions φ_i of Eq. (A.6) and some auxiliary pseudo fermion-like structure needed in the Krylov solver.

At the lowest level, almost all functions repeatedly multiply two 3×3 complex matrices (e.g., in the update of the gauge part), or a 3×3 complex matrix and a 3–dimensional complex vector (e.g., in the Krylov solver) or compute dot products and linear combinations of complex 3–vectors. All these operations have low computational intensity, so it is convenient to compress as much as possible all basic structures by exploiting their algebraic properties. The prototypical example is $U_\mu(n)$: one only stores the first two rows of the matrix and recovers the third one on the fly as the complex conjugate of the wedge product of the first two rows[191]. This overhead is negligible with respect to the gain induced, at least for GPUs, by the reduction of the memory transfer[192, 193]².

At a higher level the single most time consuming function is the Krylov solver, which may take 40...80% of the total execution time of a realistic simulation (depending e.g. on the value of the temperature) and consists basically of repeated applications³ of the D_{oe} and D_{eo} matrices defined in Eq. (A.7), together

²A priori it would be possible to do even better, i.e. to store just 8 real numbers, but in this case the reconstruction algorithm presents some instabilities[192].

³typically $10^2 \div 10^3$ iterations are needed to reach convergence, depending on the temperature.

with some linear algebra on the pseudo fermion vectors (basically *zaxpy*-like functions). An efficient implementation of D_{eo} and D_{oe} multiplies is then of paramount importance, the effectiveness of this operation being often taken as a key figure of merit in the LQCD community.

A.2 Gauge and Fermion improvements

A.2.1 Stout Fermions

In this section we will just recall the basics of the stouting procedure (for a full discussion, the reader can refer to [17] and also look into the MILC code [194]). Stouting is a way to smooth the gauge configuration. This aim, as in the case of cooling and in the so-called Wilson flow, is reached by a procedure to reduce the value of the action. In the case of cooling, the new link is chosen as the one which minimizes the local contribution to the action⁴: the new link is in principle independent from the old one. In the case of Wilson flow (or Symanzik flow) and stouting, the derivative of the Wilson (or Symanzik) gauge action with respect to the link is computed, and the link is modified in the “direction” opposite to the gradient in order to approach the local minimum of the action. While Wilson flow is a continuous process, stouting happens in finite steps. The stouted links are related to the standard links through the equation

$$U_{i;v}^{(n+1)} = \exp\left(iQ_{i;v}^{(n)}\right) U_{i;v}^{(n)}, \quad (\text{A.9})$$

where $Q_{i;v}^{(n)}$ is a matrix which is linearly dependent on the staples $C_{i;v}^{(n)}$, which depend linearly on a parameter ρ that in our case is equal for all staples in all directions. For small enough values of ρ , stouting is also an “accurate” integrator of Wilson Flow, while for too large values of ρ the stouting procedure does not converge. The maximum value of ρ by which stouting is stable is 0.15, which is also the one we have used in our simulations.

While the links entering the Dirac operator are the stouted ones, we need to compute the force on the original links. Since the stouted links are an analytic function of the original ones, it is possible to use the chain rule to obtain the force acting on the original links. The algorithm to do that is quite involved and it has to cope with some numerical instabilities, some of which are solved in the original paper [17], and some of which have instead been pointed out and solved in the MILC code [194] and in the Nissa code [195].

A.2.2 Tree Level Symanzik improvement

The Symanzik improvement program for the Gauge part of the action can be carried out. In addition to the 4-link loop Gauge-invariant term represented by the plaquettes, 6-link loop terms can be included in the action. There are 3 of such terms, inequivalent from the point of view of lattice symmetries. In our choice, only the planar loops are considered [5, 6]. In the molecular dynamics equations, this entails having new terms - not only the usual 3-link staples, but also two geometrically inequivalent kinds of 5-link staples (which actually result in 3 stencil-wise inequivalent staples, and thus 3 different functions).

⁴Actually, this is what is done with $SU(2)$ links. With $SU(3)$ links, the procedure is iterated over the 3 subgroups.

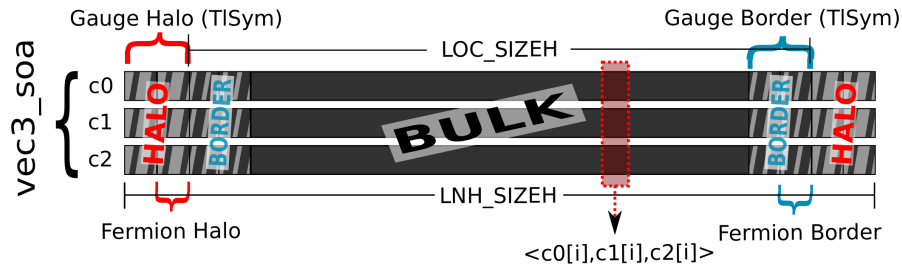


FIGURE A.1: Memory data layout for vectors, in the multi rank setup (in the single process case, the *halo* and *border* sections are missing). When using the tree level Symanzik (“TISym”) improvement for the gauge part of the action, the gauge halos and borders have to be twice as big w.r.t. the fermion one. Notice that each component is a complex value. See sections A.3.1 and A.3.3 for details.

A.3 OpenAcc implementation of the Lattice QCD code

The advantage of the OpenAcc framework over CUDA is the promise that a code written in the plain C language can be compiled and run in a multi threaded fashion on a variety of architectures just by annotating it with `#pragma` constructs. In this regard, the idea is very similar to OpenMP, but at the moment a difference still exists in the sense that OpenAcc supports GPUs, while OpenMP targets either multi-core CPUs or many-core devices, like Intel MICs. It is expected that either the two standards will converge in the future, or the OpenMP standard will incorporate OpenAcc constructs (or at least their logic).

In this section we describe the implementation of our LQCD code. Two implementations of the same algorithm were already available [196]: a C++ version targeting single-core CPUs and a C/CUDA for Nvidia GPUs. The two implementations shared only a negligible part of the code, also because the C/CUDA version had been aggressively optimized making also use of CUDA-specific features. Another implementation written in C++ and making use of OpenMP and MPI have been used for running on large clusters of CPUs [195].

In the following we describe another implementation using OpenAcc framework target to run on a cluster of GPUs. We first describe the data-structures used, then the implementation target to run on single rank, and finally that for a multi rank machine.

A.3.1 Memory allocation structure

Data structures plays an important role on performances [197] and are a key choice in implementation of a new code. In [198], we have analyzed the impact of data-structures for LQCD code, and we have shown that on GPUs a Structure of Arrays (SoA) memory data layout gives the best performances. This because the SoA format allow to process in parallel many sites of application domain (the lattice, in our case). This is also becoming more and more relevant also on CPUs, given the increase in the length of vector instructions. For this reason all data structures are implemented following the SoA paradigm.

In our implementation, we use the C99 double complex as basic data-type of application data-domain: this allows us to make use of built-in complex operators of the C library without loss of performance and making coding easier and more readable without loss of performance. The pseudo-fermion variables, which are defined only on the even half of the lattice sites, have been implemented with the `vec3_soa` as shown in figure A.1. The fact that all the sides of the lattice are even assures that the number of even

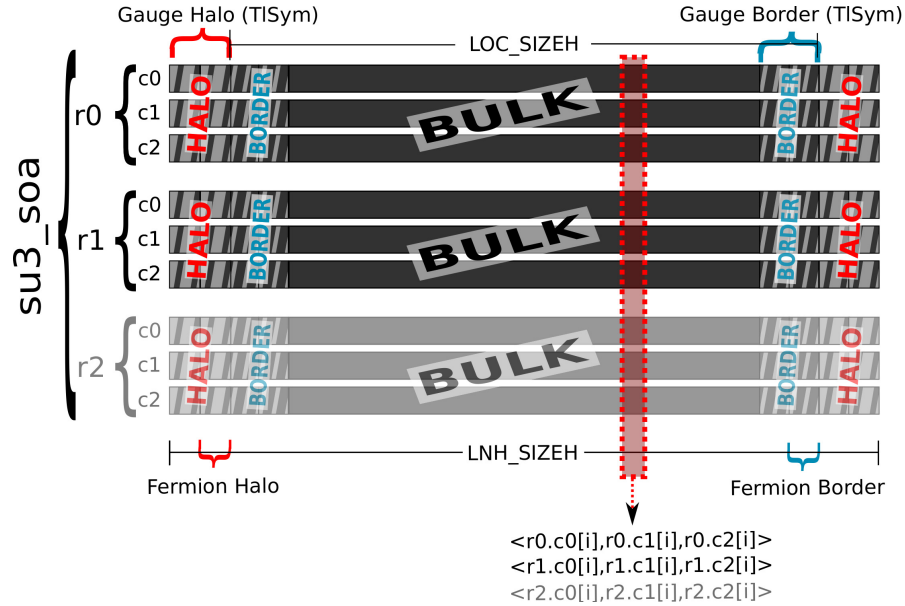


FIGURE A.2: Memory data layout for the data structures of $SU(3)$, which is implemented “as a structure containing 3 vectors. On architectures where the algorithm is severely memory bound one can avoid reading and writing the r2 member, when the unitarity constraint is satisfied.

lattice sites is half of the sites in the local lattice (i.e. the part of the lattice which will be processed by the present rank), that is LNH_SIZEH . For each even lattice site the pseudo fermion field has three complex components (the r, g and b “colors” of QCD). We implemented this data structure using the SoA approach, adopting a lexicographical ordering of the even sites. The index $idxh$ in the lexicographical ordering is calculated as

$$idxh = (\text{int}) \frac{x_0 + LNH_N0[x_1 + LNH_N1(x_2 + LNH_N2x_3)]}{2}. \quad (\text{A.10})$$

For several reasons which will be clear in the following, we decided to allow for all possible freedom in the mapping of the physical directions x, y, z and τ to the logical directions x_0, x_1, x_2 and x_3 .

The data structures representing the “staples” and the Γ_μ (a field that is necessary in the stouting procedure, see [17]), which are $GL(3)$ matrices, are stored in memory making use of the `su3_soa` data type⁵ a collection of 3 `vec3_soa` structures. The number of matrices that must be stored in memory is equal to the number of links in the lattice, which is equal to $8 LNH_SIZEH$: this means that an array of 8 `su3_soa` elements is required.

The gauge links configurations, i.e. the set of all gauge links U and necessary copies or stouted versions of it, are stored in memory as an array of 8 `su3_soa` structures. It must be remarked that the gauge links are $SU(3)$ matrices with unitarity property implying that $r2 = (r0 \wedge r1)^*$. This property can be used to reduce the bandwidth needed by a factor of $1/3$ on architectures where the algorithm is severely memory bound.

Other data structures are needed to store in memory traceless Hermitian matrices or traceless anti-Hermitian 3×3 matrices. In order to store these, only 8 real numbers per matrix are needed: the 3 complex numbers above the diagonal and the first two elements of the diagonal, which are simple real (imaginary) numbers for (anti) Hermitian traceless matrices. These data structures have been implemented according to the

⁵Here the name of the data type is slightly misleading, since this data structure is used to store $GL(3)$ matrices, while actual $SU(3)$ matrices require in principle less memory.

SoA scheme: the structures `thmat_soa` and `tamat_soa` are made of 3 vectors of double complex numbers and of 2 vectors of double numbers, in a similar fashion to `vec3_soa`.

In the single rank implementation the data movements between device and host are negligible, with significant transfers happening only at the beginning and at the end of the program, and managed with the `enter data` and `exit data` directives.

A.3.2 Implementation of the full algorithm

First, to assess the level of performance achievable with OpenAcc, we implemented a benchmark containing an OpenAcc version of the Dirac Operator, which in some cases (e.g., low temperature simulations) can account for up to 80% of the compute time. The Dirac operator is made up of three functions: `deo`, `doe` and a `zaxpy`-like function (which is negligible in terms of computation time). A direct measurement indicated that the performance of the OpenAcc versions of the double precision functions `deo` and `doe` functions were on par with the CUDA ones.

After this promising start [198], we proceeded to implement the full algorithm in OpenAcc, as it has been briefly described in Section A.1.2.

The next step has been the introduction of the action improvements to the algorithm, the aim of which is to reduce discretization errors. The improvements have been of two kinds: on the fermionic part, and on the gauge part. On the fermionic part, the improvement is the introduction of stouting, along the lines described in [17]: in the fermionic part of the action, the gauge links are replaced by a spatially smeared version of themselves with the positive side effect of reducing the condition number of the Dirac operator, thus making the solution of the linear systems in Eq.(A.8) faster. On the gauge part, the improvement consists in the introduction of rectangle terms in the action in Eq. (A.1). The implementation of the improvements consists of two sets of functions: the ones needed for the evaluation of the action, and the ones needed for the evaluation of the forces that act on momenta during the molecular dynamics evolution.

The development of these new features started with coding the logic of the improvements, then testing the results running it in a single thread fashion. Once we made sure that the results were correct, we could switch acceleration on making use of OpenAcc, annotating the code with `#pragma` constructs.

In order to have a more readable and duplicate-less code, the most complex kernels have been split in a number of functions. While small functions can be used in kernels when declared as `static inline`, for large ones we had to use the routine `seq OpenAcc` directive (because large functions won't be inlined)⁶.

Kernels have been parallelized on the device following two possible approaches. The ones which have to access data pertaining to nearest neighbors (and/or second neighbors) have been parallelized using the `#pragma acc loop` directive on 4 nested cycles (one per dimension). This allowed us to use a 3D thread blocks, which should improve data reuse between threads thus reducing the bandwidth need, which is our major concern here. The ones which instead consisted of only single-site operations have been parallelized making use of a single cycle, acting on the necessary set of lattice sites.

Here we proceed to a more detailed description of it in Algorithms 1,2, 3,4, 5 and 6 in order to give the context for the content of the present section.

⁶This is also necessary when inlining is disabled, e.g. at low levels of optimization.

In Algorithm 1 the main computational tasks are shown: the most consuming is Molecular Dynamics at step 6, which is described in Algorithm 2. A non negligible compute time is also taken by the heatbath generation of the pseudo fermions (at step 4) and the calculation of the final action (at step 7). The steps 4 and 7 consist basically in a call to the multi shift inverter function (described in Algorithm 6), with a high target accuracy.

Algorithm 1 High level scheme of the algorithm

- 1: Read gauge configuration U
 - 2: Create momenta p
 - 3: Smooth U_μ STOUT_LEVEL times
 - 4: Generate pseudo fermions with heat bath
 - 5: Calculation of initial action
 - 6: Molecular Dynamics [possibly in single precision]
 - 7: Calculate action variation ΔS
 - 8: Montecarlo step accepted with probability $\min(1, e^{-\Delta S})$
 - 9: Take measurements
-

The outer level of the multistep integrator for Molecular Dynamic evolution is described in Algorithm 2. In zero temperature simulations or for small quark masses usually the costliest parts in terms of compute time are the calculations of the fermion force, which is detailed in Algorithm 4. In high temperature simulations the load is shifted more inside the Gauge cycles, described in Algorithm 3.

Algorithm 2 MD evolution - 2nd order MN integrator (outer cycle),[190]

- 1: Fermion Force Calculation
 - 2: Evolve momenta for $\lambda\Delta T/N_{md}$ $\{\lambda = 0.1931833275037836, [189]\}$
 - 3: **for** $i = 1$ to $N_{md} - 1$ **do**
 - 4: **Gauge cycle** $(\Delta T/2N_{md})$
 - 5: Fermion Force Calculation
 - 6: Evolve momenta for $(1 - 2\lambda)\Delta T/N_{md}$
 - 7: **Gauge cycle** $(\Delta T/2N_{md})$
 - 8: Fermion Force Calculation
 - 9: Evolve momenta for $2\lambda\Delta T/N_{md}$
 - 10: **end for**
 - 11: **Gauge cycle** $(\Delta T/2N_{md})$
 - 12: Fermion Force Calculation
 - 13: Evolve momenta for $(1 - 2\lambda)\Delta T/N_{md}$
 - 14: **Gauge cycle** $(\Delta T/2N_{md})$
 - 15: Fermion Force Calculation
 - 16: Evolve momenta for $\lambda\Delta T/2N_{md}$
-

As can be seen in Algorithm 3, the actual evolution of the gauge configuration happens inside the inner gauge cycle, where the gauge contribution to the momenta evolution is also calculated. Among the tasks in Algorithm 3, the computation of staples in the gauge force calculation is the most time consuming. It consists of calculating 6 products of 3 and 5 SU(3) matrices representing links on C-shaped paths on the lattice. These functions have been parallelized using the `#pragma acc loop` directive on 4 nested cycles (one per dimension). This allowed us to use a 3D thread blocks, which should improve data reuse between threads thus reducing the bandwidth need, which is our major concern here. We shall also remark that since second-nearest-neighbor-site addressing is needed, for the sake of simplicity we decided to use

indirect addressing⁷. Notice that the function `PPMMM_5mat_prod` (as well as similar ones) has to be declared with `#pragma acc routine seq` to be used inside a kernel.

```

#pragma acc routine seq
void PPMMM_5mat_prod(...)

[...]

void calc_loc_improved_staples_typeA_nnptrick_all_bulk(
    __restrict const su3_soa * const u,
    __restrict su3_soa * const loc_stap )
{
    int d0, d1, d2, d3, mu, iter;
#pragma acc kernels present(u) present(loc_stap) present(nnp_openacc)
present(nnm_openacc)
#pragma acc loop independent gang
    for (d3=D3_HALO+GAUGE_HALO; d3<nd3-D3_HALO-GAUGE_HALO; d3++){
        [...]
#pragma acc loop independent vector(32)
        for (d0=0; d0 < nd0; d0++) {
#pragma acc loop seq
            for (mu=0; mu<4; mu++){

                [...]

                const int idx_pmu = nnp_openacc[idxh][mu][parity];
// r+mu

                [...]

                PPMMM_5mat_prod(&u[dir_nu_1R], idx_pmu, [...])

                [...]

```

LISTING A.1: The implementation of a kind of staple calculation.

Fermion force calculation is sketched in Algorithm 4. The costliest computation here is solving the equations $(M + \sigma)x^\sigma = b$, by making use of the multi shift solver (Algorithm 6). It has to be pointed out that, in this case, it is not necessary to calculate the solutions to the best possible accuracy: as long as reversibility is granted, the Metropolis step assures the stochastic correctness of the algorithm [125]. Moreover, when performing molecular dynamics in single precision, the target accuracy for the solutions has to be set to a reasonable level. It has to be remarked that the task at step 12 needs the stouted gauge configuration U^{s-1} in order to compute $i\tilde{F}^{(s-1)}$ from $i\tilde{F}^{(s)}$: this means that either the full stack of stouted gauge configurations U^s must be kept in memory, or they have to be computed again at every time. We opted for the first solution for performance reasons, but it has to be said that in some cases memory can be a concern (and this is one of the most compelling reasons to go for a multi-gpu setup).

⁷ The code would be greatly more complicated if using direct addressing, also because of some limitations in the coding options necessary to avoid branches that would destroy thread coherence.

Algorithm 3 MD Evolution - 2nd order MN integrator - Gauge cycle (for a time $\Delta_g T$)

```

1: Gauge Force Calculation
2: Evolve momenta for  $\lambda \Delta_g T / N_{gs}$ 
3: Evolve  $U$  for  $\Delta_g T / (2N_{gs})$ 
4: for  $j = 0$  to  $N_{gs} - 1$  do
5:   Gauge Force Calculation
6:   Evolve momenta for  $(1 - 2\lambda) \Delta_g T / N_{gs}$ 
7:   Evolve  $U$  for  $\Delta_g T / (2N_{gs})$ 
8:   Gauge Force Calculation
9:   Evolve momenta for  $2\lambda \Delta_g T / N_{gs}$ 
10:  Evolve  $U$  for  $\Delta_g T / (2N_{gs})$ 
11: end for
12: Gauge Force Calculation
13: Evolve momenta for  $(1 - 2\lambda) \Delta_g T / N_{gs}$ 
14: Evolve  $U$  for  $\Delta_g T / (2N_{gs})$ 
15: Gauge Force Calculation
16: Evolve momenta for  $\lambda \Delta_g T / N_{gs}$ 

```

} Gauge Block type 0
 } Gauge Block type 1
 } Gauge Block type 2
 } Gauge Block type 3

Algorithm 4 The fermion force calculation

```

1: for  $s = 1$  to STOUT_LEVEL do
2:   Calculate  $U^{(s)}$  from  $U^{(s-1)}$  {[17]}
3: end for
4:  $i\tilde{F}^{(\text{STOUT\_LEVEL})} = 0$ 
5: for  $i_{ps} = 1$  to  $N_{ps}$  do
6:   Solve  $(M + \sigma)x^\sigma = b$  {See Algorithm 6}
7:   Use  $x^\sigma$  to compute  $i\tilde{F}_{i_{ps}}$  on  $U^{(\text{STOUT\_LEVEL})}$ 
8:    $i\tilde{F}_{i_{ps}} = \exp(i\phi_{i_{ps}})i\tilde{F}_{i_{ps}}$  { $\phi_{i_{ps}}$  is the  $U(1)$  external phase associated to the pseudofermion  $i$ }
9:    $i\tilde{F}^{(\text{STOUT\_LEVEL})} += i\tilde{F}_{i_{ps}}$ 
10: end for
11: for  $s = \text{STOUT\_LEVEL}$  to 1 do
12:   Calculate  $i\tilde{F}^{(s-1)}$  from  $i\tilde{F}^{(s)}$  {[17]}
13: end for
14:  $iF = \text{traceless anti-hermitean part of } [U\tilde{F}]$ 

```

The Conjugate Gradient solver is described in Algorithm 5. It is used exclusively during measurements: note that in case it is used during the Molecular Dynamics evolution the trial solution must be chosen so to maintain time reversibility when convergence is incomplete. A possible choice for the trial solution is the null vector. The matrix-vector multiplication at step 6 is by far the most time consuming task, followed by the *zaxpy* operations at steps 9 and 10.

The Multi-Shift Conjugate gradient solver is described in Algorithm 6. The matrix-vector multiplication at step 9 is usually the most time consuming task, with the multiple *zaxpy*-like operations at steps 15 and 24. These kernels have to perform operations of the kind of $p^\sigma = \gamma^\sigma p^\sigma + \zeta_n^\sigma r$ on a number of vectors $\sigma = 1, \dots, N$ that may range from about 5 to about 20 when the solver is started, then decreases when a solution has been computed with the required precision, and finally reaches 0 when the algorithm terminates. The simplest solution to get this task done is to write a single kernel which will be launched N times, but for such a light kernel the overhead is extremely significant (around 10 μ s for synchronous mode, which would have to be paid N times). For this reason, we decided to write a kernel that also includes the iterations on N vectors. It must be remarked that there are some possible optimizations, that are still not implemented in the code. For example, it has been noted that the solutions that are the slowest to converge give also a smaller contribution to the fermion force. This suggests that the accuracy

Algorithm 5 The CG solver algorithm for the equation $Mx = b$. Lower case Latin letters represent vectors, Greek letters represent scalars.

```

1:  $s = Mx_0$  //  $x_0$  is the trial solution
2:  $r = b - s$ 
3:  $p = r$ 
4:  $\delta = \|r\|^2$ 
5: while  $\|r\|^2 / \|b\|^2 > \text{tolerance}$  do
6:    $s = Mp$  // matrix-vector multiplication
7:    $\alpha = \mathbf{Re}\{s \cdot p\}$ 
8:    $\omega = \delta / \alpha$ 
9:    $x = x + \omega p$ 
10:   $r = r - \omega s$ 
11:   $\lambda = \|r\|^2$ 
12:   $\gamma_g = \lambda / \delta$ 
13:   $\delta = \lambda$ 
14:   $p = \gamma_g p + r$ 
15: end while

```

could be relaxed on these solutions, or that a multi-scale integration scheme could be used, where the force contribution is calculated more often for the most important solutions, and less often for the least important ones [199].

In order to improve the performance of the single process program, we also implemented a single precision version of the code for the molecular dynamics evolution. Due to the low arithmetic density of the LQCD algorithms, on GPUS at least all the kernels are memory-bound. This means that, when precision is not an issue, it is preferable to use a single precision version of selected algorithms and structures, and it is reasonable to expect a plain $\times 2$ reduction in execution times for single precision kernels w.r.t double precision ones. It must be remarked though that the action computations for the Metropolis test must be performed using the highest possible precision.

A.3.3 Multi-rank implementation

The general idea for the multi-rank implementation was to have a number N_{Ranks} of MPI processes (*ranks*), each performing the computations pertaining to a portion of the whole lattice which has been split in N_{Ranks} equal parts along one direction. The choice of the direction to split the lattice along has to be done in order to minimize the amount of data that need to be transferred, which is proportional to the volume of the 3D hypersurface between the different portions of the lattice. This criterion suggests that the longest direction is the one to cut, i.e. the Euclidean time direction for zero-temperature simulations, and one of the three spatial directions in the finite temperature case. This required our code to be versatile enough so that we could map the physical directions of the lattice to the logical directions in our code, so that the direction along which the lattice has the largest size is mapped on x_3 (the “slowest” index) in Eq.(A.10).

A brief explanation of the terminology is in order. With *local lattice* of a rank we indicate the portion of the lattice to which all the position-dependent quantities computed on that rank are related. With *halo* we refer to the portions of the lattice that are needed for the computation on a given rank, but are not a part of the local lattice, and the data relative to it must be received from other ranks prior to the computation. With *border* we refer to the parts of the local lattice which correspond to the halos for the neighboring ranks. We usually refer with *bulk* to the part of the local lattice which does not include the border.

Algorithm 6 The shifted CG solver for the equations $(M + \sigma)x^\sigma = b$. Lower case Latin letters represent vectors, Greek letters represent scalars.

```

1:  $x^\sigma = 0$  // ( $\forall \sigma$ )
2:  $p = r = b$ 
3:  $\delta = \|r\|^2$ 
4:  $\omega_0 = 1$ 
5:  $\gamma_g = 0$ 
6:  $\zeta_{-1}^\sigma = \zeta_0^\sigma = 1$ ,  $\gamma_s^\sigma = 0$ ,  $p^\sigma = b$  // ( $\forall \sigma$ )
7:  $n = 1$ 
8: while not all  $x^\sigma$  converged with required accuracy do
9:    $s = Mp$  // matrix-vector multiplication
10:   $\alpha = \mathbf{Re}\{s \cdot p\}$ 
11:   $\omega_n = -\delta/\alpha$ 
12:  if  $x^\sigma$  not yet converged then
13:     $\zeta_n^\sigma = \frac{\zeta_{n-2}^\sigma \zeta_{n-1}^\sigma \omega_{n-1}}{\omega_n \gamma_g (\zeta_{n-2}^\sigma - \zeta_{n-1}^\sigma) + \zeta_{n-2}^\sigma \omega_{n-1} (1 - \sigma \omega_n)}$ ,
14:     $\omega^\sigma = \omega_n \frac{\zeta_n^\sigma}{\zeta_{n-1}^\sigma}$ ,
15:     $x^\sigma = x^\sigma - \omega^\sigma p^\sigma$  // multiple vector operations
16:  end if
17:   $r = r - \omega s$ 
18:   $\lambda = \|r\|^2$ 
19:   $\gamma_g = \lambda/\delta$ 
20:   $\delta = \lambda$ 
21:   $p = \gamma_g p + r$ 
22:   $\gamma^\sigma = \gamma_g \omega^\sigma \frac{\zeta_n^\sigma}{\zeta_{n-1}^\sigma}$ 
23:  if  $x^\sigma$  not yet converged then
24:     $p^\sigma = \gamma^\sigma p^\sigma + \zeta_n^\sigma r$  // multiple vector operations
25:     $\kappa^\sigma = \frac{\delta (\zeta_{n-1}^\sigma)^2}{\|b\|}$ 
26:    if  $\kappa < \text{tolerance}$  then
27:       $x^\sigma$  converged
28:    end if
29:  end if
30:   $n = n + 1$ 
31: end while

```

In our simple setup (with only a single-direction cut), thanks to a clever order of lattice sites in memory, it is possible to have a natural division of halo-border-bulk sections of the data structures, as visible in Figs.A.1 and A.2, thus avoiding the need of using gather-scatter kernels. It has to be remarked that, for gauge-related computations, the *halo* and *border* regions must have a thickness of 2 lattice sites when the tree level Symanzik improvement is turned on (because of the rectangular 2×1 staples and rectangles) and 1 lattice site otherwise, while for the fermion part the halo and border are 1-site thick. For the sake of simplicity, as far as structure allocations are concerned, we did not distinguish between these two cases and the halo-border thickness has been taken as the maximum necessary, while of course during communications only the strictly necessary data are transferred.

The largest communications between ranks are of two types: gauge links and pseudo fermion field. In Figs.A.1 and A.2 the portion of the data structures that has to be transferred is shown. In the pseudo fermion case, each rank has to send 6 packets while receiving 6. When double precision is used, the size of each packet is

$$s = (V_4/L_{cut}) \text{ sizeof(double)} , \quad (\text{A.11})$$

where V_4 is the 4-dimensional volume of lattice, and L_{cut} is the size of the direction which has been cut. In the case of a $32^3 \times L_{cut}$ lattice, packet size is around 260KB. In the case of gauge links, the number of such packets for each rank is 96 to send and 96 to receive.

In order to achieve a better scalability it was necessary to superpose the calculation in the bulk with the transfers of the data pertaining to halos and borders. This means to duplicate some functions, to have a version acting on the bulk and another acting on the borders. This has been done for the `deo` and `doe` functions, and for the three elements of the Gauge Blocks in Algorithm 3: the force calculation, momenta evolution and gauge link evolution. It must be remarked that we made use of the CUDA-aware feature of Open MPI in order for the `MPI_send` and `MPI_recv` instructions to manage the transfers directly from and to device memory. Another observation is that all functions implementing linear combinations of vectors did not need to be split, and operated on the whole local lattice and halos (in this case just 1-site thick). If the task to split required to access data pertaining to nearest neighbors, then only the outer cycle was split into three cycles with different limits; if the task consisted only of single-site operations the only cycle was split in three cycles.

For both the `deo` and `doe` functions it was convenient to write a wrapper that would perform the calculations on the borders, communicate the border results to neighboring ranks (and receive the halo results from neighboring ranks) and perform calculations in the bulk. In order to achieve the communication-computation superposition, we had to use the asynchronous versions of the MPI “send” and “recv” functions, and the `async` clause in the `kernels` construct (see listing A.3), and then use `MPI_Waitall` functions to wait for the end of the transfers.

In the case of gauge cycle, we came to the conclusion that the most convenient approach was to perform all the computations of a Gauge Block on the borders, then communicate the evolved gauge links while performing the computations of the same Gauge Block in the bulk.

In the case of the gauge functions we used the asynchronous versions of the MPI “send” and “recv” functions, but no `async` directive was necessary.

```
inline void acc_Deo( __restrict const su3_soa * const u,
    __restrict vec3_soa * const out,
    __restrict const vec3_soa * const in,
    const double_soa * backfield)
{
    MPI_Request send_border_requests[6], recv_border_requests[6];

    // computations on the borders
    acc_Deo_d3p(u, out, in, backfield); // on async(2)
    acc_Deo_d3m(u, out, in, backfield); // on async(3)

    #pragma acc wait(2)
    #pragma acc wait(3) // waiting for computations on the border to end

    communicate_fermion_borders_async(out, send_border_requests,
        recv_border_requests); // using MPI_Isend() and MPI_Irecv()

    // computations on the bulk
    acc_Deo_bulk(u, out, in, backfield); // on async(1)

    MPI_Waitall(6, recv_border_requests, MPI_STATUSES_IGNORE);
    MPI_Waitall(6, send_border_requests, MPI_STATUSES_IGNORE);
    #pragma acc wait(1)
}
```

LISTING A.2: The high level implementation of the *deo* function in the multinode setup, with asynchronous communications

```

void multistep_2MN_gauge_async_bloc(su3_soa *tconf_acc_old,
    su3_soa *tconf_acc_new, su3_soa *local_staples, tamat_soa *tipdot,
    thmat_soa *tmomenta, int omelyan_index)
{

    MPI_Request send_border_requests[96];
    MPI_Request recv_border_requests[96];

    // force calculations on the borders
    calc_ipdot_gauge_soloopenacc_d3c(tconf_acc_old, local_staples, tipdot,
        HALO_WIDTH, GAUGE_HALO);
    [...]

    // momenta evolution on the borders
    mom_sum_mult_d3c(tmomenta, tipdot, deltas_Omelyan, omelyan_index,
        HALO_WIDTH, GAUGE_HALO);
    [...]

    // gauge links evolution on the borders
    mom_exp_times_conf_soloopenacc_d3c(
        tconf_acc_old, tconf_acc_new, tmomenta,
        deltas_Omelyan, 4,
        HALO_WIDTH, GAUGE_HALO);
    [...]

    // asynchronous communication of the evolved gauge links
    // with MPI_Isend and MPI_Irecv
    communicate_su3_borders_async(tconf_acc_new, GAUGE_HALO,
        send_border_requests, recv_border_requests);

    // Same computations, on the bulk
    calc_ipdot_gauge_soloopenacc_bulk(tconf_acc_old, local_staples, tipdot);
    mom_sum_mult_bulk(tmomenta, tipdot, deltas_Omelyan, omelyan_index);
    mom_exp_times_conf_soloopenacc_bulk(
        tconf_acc_old, tconf_acc_new, tmomenta,
        deltas_Omelyan, 4);

    MPI_Waitall(96, send_border_requests, MPI_STATUSES_IGNORE);
    MPI_Waitall(96, recv_border_requests, MPI_STATUSES_IGNORE);
}

```

LISTING A.3: The high level implementation of the gauge molecular dynamics evolution in the multi-rank setup, with asynchronous communications

Appendix B

Measurement of Fermionic observables

B.1 Noisy estimators and noise vectors

Let's take a set of uncorrelated stochastic *real* variables η_i , which satisfy the property

$$\langle \eta_i \eta_j \rangle_{noise} = \delta_{i,j} , \quad (\text{B.1})$$

where $\langle \dots \rangle_{noise}$ represent the average over “noise” fluctuations.

Let's assume we have a *noise vector* η , with components η_i (where i will label a lattice site), and a determined matrix $A_{i,j}$ (which is not stochastic!), then we obtain

$$\left\langle \left(\sum_{ij} \eta_i A_{ij} \eta_j \right) \right\rangle_{noise} = \sum_{ij} A_{ij} \delta_{ij} = \text{Tr} A . \quad (\text{B.2})$$

Notice that the sum and the average over noise commute. Let's do another exercise now. We want to compute

$$(\text{Tr} A)^2 . \quad (\text{B.3})$$

It must be remarked that¹

$$\left(\left\langle \left(\sum_{ij} \eta_i A_{ij} \eta_j \right) \right\rangle_{noise} \right)^2 \neq \left\langle \left(\sum_{ij} \eta_i A_{ij} \eta_j \right)^2 \right\rangle_{noise} , \quad (\text{B.4})$$

indeed

$$\left\langle \left(\sum_{ij} \eta_i A_{ij} \eta_j \right)^2 \right\rangle_{noise} = \left\langle \sum_{ijkl} \eta_i A_{ij} \eta_j \eta_k A_{kl} \eta_l \right\rangle_{noise} . \quad (\text{B.5})$$

First of all, the only terms in the sum which give a nonzero contribution are the ones in which $i = j$ and $k = l$, or $i = k$ and $j = l$, or $i = l$ and $j = k$. Moreover, if $i = j = k = l$, we have to take into consideration also the value of $\langle \eta_i^4 \rangle$ (the *contact term*), so

$$\left\langle \left(\sum_{ij} \eta_i A_{ij} \eta_j \right)^2 \right\rangle_{noise} = \sum_{i \neq j} [A_{ii} A_{jj} + A_{ij} A_{ji} + A_{ij} A_{ij}] + \sum_i A_{ii}^2 \langle \eta_i^4 \rangle_{noise} \quad (\text{B.6})$$

¹ The right hand side of Eq.(B.4) is exactly what one would obtain using only *one* random vector to evaluate $(\langle \text{Tr} A \rangle_{noise})^2$.

In order to properly estimate the LHS of Eq.(B.4), we have to use *more than one* random vector. Different *independent* random vectors, labeled by Greek indices, must satisfy the relation

$$\langle \eta_i^\alpha \eta_j^\beta \rangle_{noise} = \delta_{ij} \delta^{\alpha\beta} . \quad (\text{B.7})$$

Then, if $\alpha \neq \beta$,

$$\left\langle \sum_{ij} \eta_i^\alpha A_{ij} \eta_j^\alpha \sum_{kl} \eta_k^\beta A_{kl} \eta_l^\beta \right\rangle_{noise} = \sum_i A_{ii} \sum_j A_{jj} = (\text{Tr}A)^2 , \quad (\text{B.8})$$

which is exactly what we want.

Notice one could use *complex* noise vectors, satisfying

$$\begin{cases} \langle \eta_i^\dagger \eta_j \rangle_{noise} = \delta_{ij} , \\ \langle \eta_i \eta_j \rangle_{noise} = 0 , \end{cases}$$

which implies that the real part and the imaginary part of η must satisfy a relation like Eq.(B.7). Then,

$$\left\langle \left(\sum_{ij} \eta_i^\dagger A_{ij} \eta_j \right)^2 \right\rangle_{noise} = \sum_{i \neq j} [A_{ii} A_{jj} + A_{ij} A_{ji}] + \sum_i A_{ii}^2 \left\langle \left(\eta_i^\dagger \eta_i \right)^2 \right\rangle_{noise} , \quad (\text{B.9})$$

which is not yet what we want.

B.1.1 Errors

Getting back to the real case, we can see what is the variance² of our estimator of $\text{Tr} A$, that is

$$\frac{1}{N} \sum_{\alpha, ij} \eta_i^\alpha A_{ij} \eta_j^\alpha . \quad (\text{B.10})$$

To calculate this, we need to compute the average of the modulus of its square first:

$$\frac{1}{N^2} \sum_{\alpha\beta} \sum_{ij,kl} A_{ij} A_{kl}^* \langle \eta_i^\alpha \eta_j^\alpha \eta_k^\beta \eta_l^\beta \rangle_{noise} . \quad (\text{B.11})$$

This is equal to

$$\frac{1}{N^2} \sum_{\alpha \neq \beta} \sum_{ij,kl} A_{ij} A_{kl}^* \langle \eta_i^\alpha \eta_j^\alpha \eta_k^\beta \eta_l^\beta \rangle_{noise} + \frac{1}{N^2} \sum_{\alpha} \sum_{ij,kl} A_{ij} A_{kl}^* \langle \eta_i^\alpha \eta_j^\alpha \eta_k^\alpha \eta_l^\alpha \rangle_{noise} . \quad (\text{B.12})$$

The first part is just related to the square of the trace, because if $\alpha \neq \beta$ the η vectors are independent. The second term instead has been already calculated in Eq.(B.6), so we obtain

$$\frac{N(N-1)}{N^2} |\text{Tr} A|^2 + \frac{1}{N} \left[\sum_{i \neq j} [A_{ii} A_{jj}^* + A_{ij} A_{ji}^* + A_{ij} A_{ij}^*] + \sum_i |A_{ii}|^2 \langle (\eta_i^\alpha)^4 \rangle_{noise} \right] \quad (\text{B.13})$$

² The variance of a complex number $z = x + iy$ should be defined as

$$\langle x^2 \rangle + \langle y^2 \rangle - \langle x \rangle^2 - \langle y \rangle^2 = \langle z^* z \rangle - \langle z^* \rangle \langle z \rangle$$

In the following, we will assume $\langle (\eta_i^\alpha)^4 \rangle_{noise} = c_4$ for all α and i . The terms can be rearranged to give

$$|\mathrm{Tr} A|^2 + \frac{1}{N} \left[\mathrm{Tr} AA^* + \mathrm{Tr} AA^\dagger + \sum_i |A_{ii}|^2 (c_4 - 3) \right] \quad (\text{B.14})$$

In order to obtain the variance of the trace estimator, we have to subtract

$$\left\langle \frac{1}{N} \sum_{\alpha, ij} \eta_i^\alpha A_{ij} \eta_j^\alpha \right\rangle_{noise}^2 = |\mathrm{Tr} A|^2 \quad (\text{B.15})$$

and then we obtain

$$\varepsilon^2 = \frac{1}{N} \left[\mathrm{Tr} AA^* + \mathrm{Tr} AA^\dagger + \sum_i |A_{ii}|^2 (c_4 - 3) \right]. \quad (\text{B.16})$$

Notice that, if η_i is Gaussian, $c_4 = 3$, while if η_i is a stochastic Z_2 variable, $c_4 = 1$. Moreover, for any probability distribution, $\langle x^4 \rangle \geq \langle x^2 \rangle^2$, and since we fixed $\langle x^2 \rangle = 1$ in Eq.(B.1), we see that the Z_2 choice is the one that minimizes the errors.

Moreover, it is straightforward to verify that ε^2 above vanishes when using Z_2 noise in the case where A is real and diagonal.

B.2 Chiral condensate

The chiral condensate for a given quark is defined as

$$\langle \bar{\psi}_q \psi_q \rangle = \frac{\partial}{\partial m_q} \log Z \quad (\text{B.17})$$

On the lattice, it is calculated through noisy estimators.

$$\langle \bar{\psi}_q \psi_q \rangle = \mathrm{Tr} M_q^{-1} = \langle \phi M_q^{-1} \phi \rangle_{noise}, \quad (\text{B.18})$$

where M_q is the Dirac matrix associated to the quark q (thus including the $SU(3)$ gauge links, which are the same for all quarks, and the optional $U(1)$ phase field, which may include electromagnetic fields and *imaginary* chemical potentials), and $\langle \dots \rangle_{noise}$ means an average on the noise vectors ϕ . As a necessary and sufficient condition for the last equality to hold, the scalar product between two different noise vectors ϕ_i must satisfy

$$\langle \phi_i \phi_j \rangle_{noise} = \delta_{ij} \quad (\text{B.19})$$

Given a Z_2 noise vector³ ϕ , an estimate of the chiral condensate will be

$$\langle \bar{\psi}_q \psi_q \rangle = \phi M_q^{-1} \phi. \quad (\text{B.20})$$

The issue here is to estimate

$$\chi = M_q^{-1} \phi. \quad (\text{B.21})$$

³It may also be Gaussian, but it seems that Z_2 works best.

Notice that the algorithm used in the code to invert a matrix (the *conjugate gradient* method) requires the matrix to be *Hermitian*. M_q is not, but $M_q^\dagger M_q$ is. Then, the trick will be to calculate

$$\chi = (M_q^\dagger M_q)^{-1} M_q^\dagger \phi. \quad (\text{B.22})$$

In order to be more concrete, let's say a bit more about the structure of the Dirac matrix (let's forget for the sake of my fingers the subscript q , we're concerned by only a quark species at a time anyway). In the staggered formulation (see, for example [9])

$$M_{i,j} = \sum_{\mu=1}^4 [U_\mu(i) \delta_{i+\hat{\mu},j} - U_\mu^\dagger(i-\hat{\mu}) \delta_{i-\hat{\mu},j}] + m \delta_{i,j} \quad (\text{B.23})$$

where U_μ contains also *all* the $U(1)$ phases you can think of (the staggered phases η_μ , the imaginary chemical potentials and the electromagnetic fields), while i and j are indices for the lattice sites. It is very apparent that the first term only connects *even* sites to *odd* sites. Symbolically, we can write

$$M = \begin{pmatrix} M_{ee} & M_{eo} \\ M_{oe} & M_{oo} \end{pmatrix} = \begin{pmatrix} m & D_{eo} \\ D_{oe} & m \end{pmatrix},$$

where the gauge links and $U(1)$ phases are contained in the D_{eo} and D_{oe} sub-matrices. Notice that the matrix

$$D = \begin{pmatrix} 0 & D_{eo} \\ D_{oe} & 0 \end{pmatrix}$$

is anti Hermitian⁴. This means that

$$M^\dagger M = \begin{pmatrix} m^2 - D_{eo} D_{oe} & 0 \\ 0 & m^2 - D_{oe} D_{eo} \end{pmatrix}.$$

Notice that the sub-matrices $(m^2 - D_{eo} D_{oe})$ and $(m^2 - D_{oe} D_{eo})$ are Hermitian. So our ploy shown in Eq.(B.22) turns into

$$\begin{pmatrix} \chi_e \\ \chi_o \end{pmatrix} = \begin{pmatrix} [m^2 - D_{eo} D_{oe}]^{-1} & 0 \\ 0 & [m^2 - D_{oe} D_{eo}]^{-1} \end{pmatrix} \begin{pmatrix} m & -D_{eo} \\ -D_{oe} & m \end{pmatrix} \begin{pmatrix} \phi_e \\ \phi_o \end{pmatrix},$$

from which we read

$$\chi_e = [m^2 - D_{eo} D_{oe}]^{-1} (m \phi_e - D_{eo} \phi_o) \quad (\text{B.25})$$

and a similar equation for χ_o . From this reasoning it may look like we need to perform two inversions, one to obtain χ_e and another to obtain χ_o . We can avoid the second inversion by making use of the original statement of the problem, (Eq. B.21), which implies $\phi = M \chi$:

$$\begin{pmatrix} \phi_e \\ \phi_o \end{pmatrix} = \begin{pmatrix} m & D_{eo} \\ D_{oe} & m \end{pmatrix} \begin{pmatrix} \chi_e \\ \chi_o \end{pmatrix}.$$

⁴There are two ways to see this: the clever one is to notice that D is the lattice discretization of a derivative, and as such must be anti-hermitian. The *poor man* way to see this (or the *pedantic man* way to check it) is to use Eq.(B.23), noticing that

$$(D_{eo})_{ij} = -(D_{oe})_{ji}^\dagger, \quad (\text{B.24})$$

as it must be.

This tells us that $\phi_o = D_{oe}\chi_e + m\chi_o$, which implies

$$\chi_o = \frac{1}{m} (\phi_o - D_{oe}\chi_e) .$$

Once χ_e and χ_o are calculated, our estimate of the chiral condensate (for a given quark) will be

$$\langle \bar{\psi}\psi \rangle = \phi_e^\dagger \chi_e + \phi_o^\dagger \chi_o . \quad (\text{B.26})$$

An alternative consists of exploiting the obvious relation, valid only stochastically on an ensemble of configurations:

$$\langle \phi_o^\dagger \chi_o \rangle = \langle \phi_e^\dagger \chi_e \rangle . \quad (\text{B.27})$$

B.3 Nonzero chemical potential on the lattice and the quark number

Let's for the sake of simplicity limit the present discussion to one quark only. In the continuum, in the Euclidean formulation, in the presence of a nonzero chemical potential, we have

$$Z = \int DA^E D\bar{\psi} D\psi \exp \{ -S_g^E(A^E) - \bar{\psi} [\gamma_V^E (\partial_V - iA_V^E) + m] \psi + \mu \bar{\psi} \gamma_4 \psi \} . \quad (\text{B.28})$$

This is equivalent to substitute the usual Dirac operator with

$$M(\mu) = [\gamma_V^E (\partial_V - iA_V^E) - \mu \gamma_4 + m] \quad (\text{B.29})$$

Two remarks are in order:

1. The usual Hybrid Montecarlo algorithm relies on the Euclidean action S^E being real. The gauge Euclidean action S_g^E being real, this requires the determinant of the fermion matrix $M(\mu)$ to be real. A sufficient condition for this, is the γ_5 -hermiticity condition⁵, $\gamma_5 M \gamma_5 = M^\dagger$, which is only true if μ is zero or *pure imaginary*, that is $\mu = i\mu_I$.
2. The term containing μ can be reabsorbed in A_4^E , once one replaces A_4^E with

$$A_4^E = A_4^E - i\mu \mathbf{1} = A_4^E + \mu_I \mathbf{1} . \quad (\text{B.30})$$

This means that, if we take μ pure imaginary, we can interpret it as an additional $U(1)$ phase in the Fermion Matrix⁶.

With these observations, the (i, j) element of the μ -dependent staggered Dirac operator might be written as

$$M_{i,j} = \frac{1}{2a} \sum_V \eta_V(i) \left[e^{\mu a \delta_{V,4}} U_V(i) \delta_{i+\hat{V},j} - e^{-\mu a \delta_{V,4}} U_V^\dagger(j) \delta_{i-\hat{V},j} \right] \quad (\text{B.31})$$

⁵Of course this relies on the property

$$\text{Det}(M) = \text{Det}(\gamma^5 M \gamma^5) .$$

⁶ A little discussion here is in order. The first idea one can have for introducing a nonzero chemical potential on the lattice, is to “naively” discretize the term $\bar{\psi} \gamma_4 \psi$. Unfortunately, this recipe produces (additional) divergences that cannot be “renormalized away” even in the free-field case[200].

where i and j label the lattice sites, $\eta_v(i)$ are the staggered phases, and $U_v(i)$ are the $SU(3)$ gauge links. Notice that, since in our case $\mu = i\mu_I$,

$$M_{i,j} = \frac{1}{2a} \sum_v \eta_v(i) \left[e^{i\mu_I a \delta_{v,4}} U_v(i) \delta_{i+\hat{v},j} - e^{-i\mu_I a \delta_{v,4}} U_v^\dagger(j) \delta_{i-\hat{v},j} \right] \quad (\text{B.32})$$

The quark number observable n_q on the lattice can be written as

$$n_q = \frac{\partial}{\partial \mu} \log Z = Z^{-1} \int DU e^{-S_g^E} \frac{\partial \det M(\mu)}{\partial \mu}. \quad (\text{B.33})$$

Noticing that $\det M(\mu) = \prod_i \lambda_i$, we have⁷

$$\frac{\partial \det M(\mu)}{\partial \mu} = \sum_i \frac{\partial \lambda_i}{\partial \mu} \frac{1}{\lambda_i} \prod_j \lambda_j = \text{Tr} \left(\frac{\partial M}{\partial \mu} M^{-1} \right) \det M. \quad (\text{B.34})$$

Notice that $\partial M / \partial \mu$, from Eq.(B.31), is

$$\begin{aligned} \frac{\partial M_{i,j}}{\partial \mu} &= \frac{1}{2} \eta_4(i) \left[e^{\mu a} U_4(i) \delta_{i+\hat{4},j} + e^{-\mu a} U_4^\dagger(j) \delta_{i-\hat{4},j} \right] = \\ &= \frac{1}{2} \eta_4(i) \left[e^{\mu a} U_4(i) \delta_{i+\hat{4},j} + e^{-\mu a} U_4^\dagger(j) \delta_{i-\hat{4},j} \right]. \end{aligned}$$

Notice that $\mu a = \frac{\mu}{n_f T}$.

B.3.1 The case of a biased estimator: $|\text{Im}N|$

In some cases, it is necessary to evaluate the quantity $|\text{Im}N|$ (where N is the quark number) instead of $\text{Im}N$ (see, e.g., Eq.3.24). It is expected that applying a nonlinear function to the non-biased estimator

$$N = \frac{1}{N} \sum_{\alpha=1}^N \eta_\alpha^\dagger \frac{\partial M}{\partial \mu} M^{-1} \eta_\alpha \quad (\text{B.35})$$

will give a biased estimator. A brute force solution to the bias issue can be just ‘‘get more statistics’’, if the estimator is asymptotically unbiased. But in this case, the number of random vectors per configuration is set at the beginning of the simulation: the value of N for *every* configuration will be biased, and it will not be possible to take other measurements on the same gauge configurations.

This is necessary as in the Polyakov loop, for example, to locate the Roberge-Weiss transition looking at quark number: the disconnected susceptibility of $|\text{Im}N|$ exhibits a peak at the transition, while the connected susceptibility of $\text{Im}N$ at finite volume and infinite statistics does not decrease for $T > T_c$, due to nonzero tunnel probability.

The problem is to find an unbiased estimator for the quantity $|\langle x \rangle|$, where $\langle \dots \rangle$ means the noise mean. The naive estimator is $|\bar{x}|$: assuming that the estimator \bar{x} has a variance ϵ^2 , the bias can be easily calculated:

$$\langle |\bar{x}| \rangle = \bar{x} \text{Erf} \left(\frac{\bar{x}}{\epsilon} \right) + \sqrt{\frac{2}{\pi}} \epsilon e^{-\frac{\bar{x}^2}{2\epsilon^2}}, \quad (\text{B.36})$$

⁷It is also possible to use the classical trick $\det M = e^{\text{Tr} \log M}$ with the same effect.

where

$$\text{Erf}(z) = 2/\sqrt{\pi} \int_0^z e^{-t^2} dt . \quad (\text{B.37})$$

It can be seen that the maximum value of the bias is when $\frac{\bar{x}}{\varepsilon} = 0$, and that the bias is negligible when $|\frac{\bar{x}}{\varepsilon}| > 3$ or so. The question one can ask oneself is if there is an unbiased estimator $f(x)$ for which ⁸

$$\int_{-\infty}^{+\infty} f(\bar{x}) p(\bar{x}) d\bar{x} = |\langle x \rangle| . \quad (\text{B.40})$$

Now, let's assume that \bar{x} is a Gaussian random variable, with mean μ and standard deviation ε : then Eq.(B.40) becomes

$$\frac{1}{\sqrt{2\pi\varepsilon}} \int_{-\infty}^{+\infty} f(\bar{x}) e^{-\frac{(\bar{x}-\mu)^2}{2\varepsilon^2}} d\bar{x} = |\mu| . \quad (\text{B.41})$$

It can be easily argued that such a $f(x)$ that would satisfy Eq.B.41 cannot exist, because any non-pathological function smoothed with a Gaussian low-pass filter will never exhibit a singular point as the one of $|x|$. To prove this point, a solution can be looked for using using the Fourier transform. In fact, Fourier transforming Eq.(B.41) one obtains

$$\frac{1}{\sqrt{2\pi}} \tilde{f}(y) e^{-\frac{(\varepsilon y)^2}{2}} e^{-i\mu y} = -\sqrt{\frac{2}{\pi}} \frac{1}{y^2} , \quad (\text{B.42})$$

which would imply

$$f(x) = -\frac{1}{\sqrt{2\pi}} \int dy \frac{2}{y^2} e^{\frac{(\varepsilon y)^2}{2}} e^{i(\mu+x)y} . \quad (\text{B.43})$$

This integral cannot be computed, or made sense of. It is not possible to anti-transform $\tilde{f}(y)$ in order to obtain $f(x)$, since the integral would be too violently divergent in the ultraviolet.

A possible way out is to regularize the integral: for example, regularizing with a factor $e^{-\frac{(\varepsilon y)^2}{2}}$ would yield the naive estimator $f(x) = |x|$. It can be noted that a numerical approach that tries to obtain a zero bias on a grid of points is in principle possible, but it will yield an estimator with a divergent variance as the grid is made finer and finer. A compromise could be made between the need of correcting the bias and the need of keeping the variance small enough for the estimator to be useful.

B.3.2 A pedagogical failure: the susceptibility of $|\text{Im } n_l|$ at the transition

As an example of biased estimator, here are estimates of the absolute values of the light quark number, and its disconnected susceptibility

$$\chi_{\text{Im } n_l} \propto \langle (\text{Im } n_l)^2 \rangle - \langle |\text{Im } n_l| \rangle^2 . \quad (\text{B.44})$$

⁸In this frame of mind it is possible, for example, to look for an estimator $g(x)$ so that

$$\frac{1}{\sqrt{2\pi\varepsilon}} \int_{-\infty}^{+\infty} g(x) e^{-\frac{(x-\mu)^2}{2\varepsilon^2}} d\bar{x} = \mu^2 . \quad (\text{B.38})$$

It is very easy to see that $g(x) = x^2 - \varepsilon^2$ satisfy the given equation. Of course, this requires ε to be known a priori. An unbiased estimator for ε from N variables would be the function f that satisfy the equation

$$\int d^N x f(x_1, \dots, x_N) \exp\left(-\frac{\sum_{i=1}^N (x_i - \mu)^2}{2\varepsilon^2}\right) = \varepsilon \quad (\text{B.39})$$

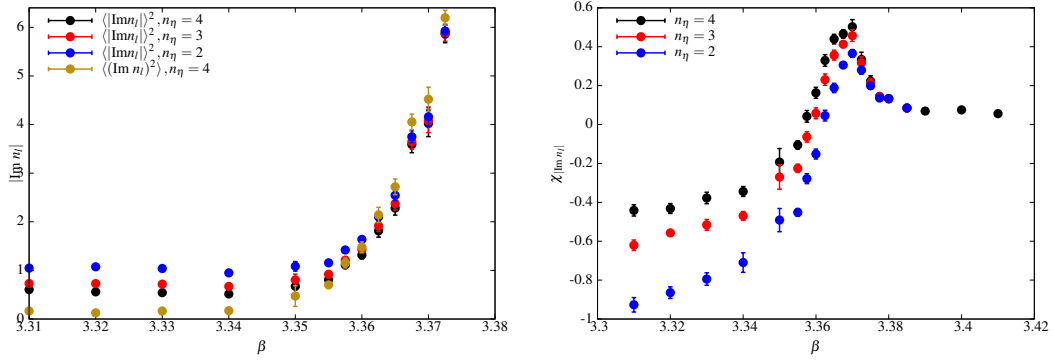


FIGURE B.1: **Left:** The square of the absolute value of the imaginary part of the light quark number estimator, at $m_l a = 0.00075$ for $L = 20$, measured with 2,3 and 4 random vectors per quark, and the square of the imaginary part of the light quark number estimator, measured with 4 random vectors (bias on $(\text{Im } n_l)^2$ is negligible). The bias is evident for $|\text{Im } n_l|^2$. **Right:** The susceptibility of the absolute value of the imaginary part of the light quark number for the same setup, measured with 2,3 and 4 random vectors per quark.

A catastrophic effect of bias is visible on the susceptibility, in Fig. B.1: a quantity which should be definite positive is not as such anymore, especially at low β where $\text{Im } n_l$ should be very close to zero. This is due to the fact that, as shown in Fig.B.1, due to the bias on the $|\text{Im } n_l|^2$ estimator the quantity $\langle |\text{Im } n_l|^2 \rangle$ is larger than the quantity $\langle (\text{Im } n_l)^2 \rangle$. Notice that bias is increased as the number of measurements is lowered.

Bibliography

- [1] David J. Gross and Frank Wilczek. Ultraviolet Behavior of Nonabelian Gauge Theories. *Phys. Rev. Lett.*, 30:1343–1346, 1973. doi: 10.1103/PhysRevLett.30.1343.
- [2] H. David Politzer. Reliable Perturbative Results for Strong Interactions? *Phys. Rev. Lett.*, 30: 1346–1349, 1973. doi: 10.1103/PhysRevLett.30.1346.
- [3] K. Symanzik. Continuum Limit and Improved Action in Lattice Theories. 1. Principles and ϕ^4 Theory. *Nucl. Phys.*, B226:187–204, 1983. doi: 10.1016/0550-3213(83)90468-6.
- [4] K. Symanzik. Continuum Limit and Improved Action in Lattice Theories. 2. $O(N)$ Nonlinear Sigma Model in Perturbation Theory. *Nucl. Phys.*, B226:205–227, 1983. doi: 10.1016/0550-3213(83)90469-8.
- [5] P. Weisz. Continuum Limit Improved Lattice Action for Pure Yang-Mills Theory. 1. *Nucl. Phys.*, B212:1, 1983. doi: 10.1016/0550-3213(83)90595-3.
- [6] G. Curci, P. Menotti, and G. Paffuti. Symanzik’s Improved Lagrangian for Lattice Gauge Theory. *Phys. Lett.*, B130:205, 1983. doi: 10.1016/0370-2693(83)91043-2. [Erratum: *Phys. Lett.* B135,516(1984)].
- [7] M. Luscher and P. Weisz. On-Shell Improved Lattice Gauge Theories. *Commun. Math. Phys.*, 97: 59, 1985. doi: 10.1007/BF01206178. [Erratum: *Commun. Math. Phys.* 98,433(1985)].
- [8] Y. Iwasaki. Renormalization Group Analysis of Lattice Theories and Improved Lattice Action. II. Four-dimensional non-Abelian $SU(N)$ gauge model. *arXiv*, hep-lat:1111.7054, 1983.
- [9] Heinz J. Rothe. *Lattice Gauge Theories: An Introduction*. World Scientific, 2012. ISBN 978-981-4365-86-4.
- [10] E. Marinari, G. Parisi, and C. Rebbi. Monte Carlo Simulation of the Massive Schwinger Model. *Nucl. Phys.*, B190:734, 1981. doi: 10.1016/0550-3213(81)90048-1. [,595(1981)].
- [11] Michael Creutz. Flavor extrapolations and staggered fermions. *arXiv*, hep-lat:0603020, 2006.
- [12] Claude Bernard, Maarten Golterman, Yigal Shamir, and Stephen R. Sharpe. Comment on ‘Chiral anomalies and rooted staggered fermions’. *Phys. Lett.*, B649:235–240, 2007. doi: 10.1016/j.physletb.2007.04.018.
- [13] Michael Creutz. Diseases with rooted staggered quarks. *PoS*, LAT2006:208, 2006.
- [14] Stephen R. Sharpe. Rooted staggered fermions: Good, bad or ugly? *PoS*, LAT2006:022, 2006.

- [15] A. Bazavov et al. Nonperturbative QCD Simulations with 2+1 Flavors of Improved Staggered Quarks. *Rev. Mod. Phys.*, 82:1349–1417, 2010. doi: 10.1103/RevModPhys.82.1349.
- [16] E. Follana, Q. Mason, C. Davies, K. Hornbostel, G. P. Lepage, J. Shigemitsu, H. Trottier, and K. Wong. Highly improved staggered quarks on the lattice, with applications to charm physics. *Phys. Rev.*, D75:054502, 2007. doi: 10.1103/PhysRevD.75.054502.
- [17] Colin Morningstar and Mike J. Peardon. Analytic smearing of SU(3) link variables in lattice QCD. *Phys. Rev.*, D69:054501, 2004. doi: 10.1103/PhysRevD.69.054501.
- [18] Maarten F. L. Golterman. STAGGERED MESONS. *Nucl. Phys.*, B273:663–676, 1986. doi: 10.1016/0550-3213(86)90383-4.
- [19] Maarten F. L. Golterman. Irreducible Representations of the Staggered Fermion Symmetry Group. *Nucl. Phys.*, B278:417–435, 1986. doi: 10.1016/0550-3213(86)90220-8.
- [20] Szabolcs Borsanyi, Zoltan Fodor, Christian Hoelbling, Sandor D Katz, Stefan Krieg, Claudia Ratti, and Kalman K. Szabo. Is there still any T_c mystery in lattice QCD? Results with physical masses in the continuum limit III. *JHEP*, 09:073, 2010. doi: 10.1007/JHEP09(2010)073.
- [21] Alexei Bazavov and Peter Petreczky. Taste symmetry and QCD thermodynamics with improved staggered fermions. *PoS, LATTICE2010*:169, 2010.
- [22] Holger Bech Nielsen and Masao Ninomiya. Absence of Neutrinos on a Lattice. 1. Proof by Homotopy Theory. *Nucl. Phys.*, B185:20, 1981. doi: 10.1016/0550-3213(81)90361-8,10.1016/0550-3213(82)90011-6. [,533(1980)].
- [23] Holger Bech Nielsen and Masao Ninomiya. No Go Theorem for Regularizing Chiral Fermions. *Phys. Lett.*, B105:219–223, 1981. doi: 10.1016/0370-2693(81)91026-1.
- [24] Holger Bech Nielsen and Masao Ninomiya. Absence of Neutrinos on a Lattice. 2. Intuitive Topological Proof. *Nucl. Phys.*, B193:173–194, 1981. doi: 10.1016/0550-3213(81)90524-1.
- [25] Paul H. Ginsparg and Kenneth G. Wilson. A Remnant of Chiral Symmetry on the Lattice. *Phys. Rev.*, D25:2649, 1982. doi: 10.1103/PhysRevD.25.2649.
- [26] Herbert Neuberger. More about exactly massless quarks on the lattice. *Phys. Lett.*, B427:353–355, 1998. doi: 10.1016/S0370-2693(98)00355-4.
- [27] Martin Luscher. Exact chiral symmetry on the lattice and the Ginsparg-Wilson relation. *Phys. Lett.*, B428:342–345, 1998. doi: 10.1016/S0370-2693(98)00423-7.
- [28] C. Lang C. Gattringer. *Quantum Chromodynamics on the Lattice: An Introductory Presentation*. Springer, 2010. ISBN 978-3-642-01850-3.
- [29] Owe Philipsen. Lattice qcd at non-zero temperature and baryon density. *arXiv*, hep-lat:1009.4089, 09 2010.
- [30] Mark G. Alford, Anton Kapustin, and Frank Wilczek. Imaginary chemical potential and finite fermion density on the lattice. *Phys. Rev.*, D59:054502, 1999. doi: 10.1103/PhysRevD.59.054502.
- [31] Y. Aoki, G. Endrodi, Z. Fodor, S. D. Katz, and K. K. Szabo. The Order of the quantum chromodynamics transition predicted by the standard model of particle physics. *Nature*, 443:675–678, 2006. doi: 10.1038/nature05120.

- [32] Y. Aoki, Z. Fodor, S. D. Katz, and K.K. Szabo. The QCD transition temperature: Results with physical masses in the continuum limit. *Phys. Lett.*, B643:46–54, 2006. doi: 10.1016/j.physletb.2006.10.021.
- [33] A. Bazavov et al. The chiral and deconfinement aspects of the QCD transition. *Phys. Rev.*, D85:054503, 2012. doi: 10.1103/PhysRevD.85.054503.
- [34] Tanmoy Bhattacharya et al. QCD Phase Transition with Chiral Quarks and Physical Quark Masses. *Phys. Rev. Lett.*, 113(8):082001, 2014. doi: 10.1103/PhysRevLett.113.082001.
- [35] Frank R. Brown, Frank P. Butler, Hong Chen, Norman H. Christ, Zhi-hua Dong, Wendy Schaffer, Leo I. Unger, and Alessandro Vaccarino. On the existence of a phase transition for QCD with three light quarks. *Phys. Rev. Lett.*, 65:2491–2494, 1990. doi: 10.1103/PhysRevLett.65.2491.
- [36] Robert D. Pisarski and Frank Wilczek. Remarks on the Chiral Phase Transition in Chromodynamics. *Phys. Rev.*, D29:338–341, 1984. doi: 10.1103/PhysRevD.29.338.
- [37] Philippe de Forcrand and Massimo D’Elia. Continuum limit and universality of the Columbia plot. 2017. URL <https://inspirehep.net/record/1511686/files/arXiv:1702.00330.pdf>.
- [38] Sean Gavin, Andreas Gocksch, and Robert D. Pisarski. QCD and the chiral critical point. *Phys. Rev.*, D49:R3079–R3082, 1994. doi: 10.1103/PhysRevD.49.R3079.
- [39] Constantia Alexandrou, Artan Borici, Alessandra Feo, Philippe de Forcrand, Andrea Galli, Fred Jegerlehner, and Tetsuya Takaishi. The Deconfinement phase transition in one flavor QCD. *Phys. Rev.*, D60:034504, 1999. doi: 10.1103/PhysRevD.60.034504.
- [40] Frithjof Karsch and Sven Stickan. The Three-dimensional, three state Potts model in an external field. *Phys. Lett.*, B488:319–325, 2000. doi: 10.1016/S0370-2693(00)00902-3.
- [41] Masataka Fukugita, Masanori Okawa, and Akira Ukawa. Finite Size Scaling Study of the Deconfining Phase Transition in Pure SU(3) Lattice Gauge Theory. *Nucl. Phys.*, B337:181–232, 1990. doi: 10.1016/0550-3213(90)90256-D.
- [42] Claudio Bonati, Philippe de Forcrand, Massimo D’Elia, Owe Philipsen, and Francesco Sanfilippo. Chiral phase transition in two-flavor QCD from an imaginary chemical potential. *Phys. Rev.*, D90(7):074030, 2014. doi: 10.1103/PhysRevD.90.074030.
- [43] Stephen L. Adler. Axial vector vertex in spinor electrodynamics. *Phys. Rev.*, 177:2426–2438, 1969. doi: 10.1103/PhysRev.177.2426.
- [44] J. S. Bell and R. Jackiw. A PCAC puzzle: $\pi^0 \rightarrow \gamma \gamma$ in the sigma model. *Nuovo Cim.*, A60:47–61, 1969. doi: 10.1007/BF02823296.
- [45] Kazuo Fujikawa. Path Integral for Gauge Theories with Fermions. *Phys. Rev.*, D21:2848, 1980. doi: 10.1103/PhysRevD.21.2848,10.1103/PhysRevD.22.1499. [Erratum: *Phys. Rev.* D22,1499(1980)].
- [46] Heng-Tong Ding. Lattice QCD at nonzero temperature and density. In *Proceedings, 34th International Symposium on Lattice Field Theory (Lattice 2016): Southampton, UK, July 24-30, 2016*, 2017. URL <https://inspirehep.net/record/1511681/files/arXiv:1702.00151.pdf>.

- [47] Alexander M. Polyakov. Thermal Properties of Gauge Fields and Quark Liberation. *Phys. Lett.*, B72:477–480, 1978. doi: 10.1016/0370-2693(78)90737-2.
- [48] Leonard Susskind. Lattice Models of Quark Confinement at High Temperature. *Phys. Rev.*, D20:2610–2618, 1979. doi: 10.1103/PhysRevD.20.2610.
- [49] Larry D. McLerran and Benjamin Svetitsky. Quark Liberation at High Temperature: A Monte Carlo Study of SU(2) Gauge Theory. *Phys. Rev.*, D24:450, 1981. doi: 10.1103/PhysRevD.24.450.
- [50] Andre Roberge and Nathan Weiss. Gauge Theories With Imaginary Chemical Potential and the Phases of QCD. *Nucl. Phys.*, B275:734, 1986. doi: 10.1016/0550-3213(86)90582-1.
- [51] Nathan Weiss. The Effective Potential for the Order Parameter of Gauge Theories at Finite Temperature. *Phys. Rev.*, D24:475, 1981. doi: 10.1103/PhysRevD.24.475.
- [52] Nathan Weiss. The Wilson Line in Finite Temperature Gauge Theories. *Phys. Rev.*, D25:2667, 1982. doi: 10.1103/PhysRevD.25.2667.
- [53] David J. Gross, Robert D. Pisarski, and Laurence G. Yaffe. QCD and Instantons at Finite Temperature. *Rev. Mod. Phys.*, 53:43, 1981. doi: 10.1103/RevModPhys.53.43.
- [54] Owe Philipsen and Christopher Pinke. Nature of the Roberge-Weiss transition in $N_f = 2$ QCD with Wilson fermions. *Phys. Rev.*, D89(9):094504, 2014. doi: 10.1103/PhysRevD.89.094504.
- [55] Y. Aoki, Szabolcs Borsanyi, Stephan Durr, Zoltan Fodor, Sandor D. Katz, Stefan Krieg, and Kalman K. Szabo. The QCD transition temperature: results with physical masses in the continuum limit II. *JHEP*, 06:088, 2009. doi: 10.1088/1126-6708/2009/06/088.
- [56] Szabolcs Borsanyi, Gergely Endrodi, Zoltan Fodor, Antal Jakovac, Sandor D. Katz, Stefan Krieg, Claudia Ratti, and Kalman K. Szabo. The QCD equation of state with dynamical quarks. *JHEP*, 11:077, 2010. doi: 10.1007/JHEP11(2010)077.
- [57] Szabolcs Borsanyi, Zoltan Fodor, Christian Hoelbling, Sandor D. Katz, Stefan Krieg, and Kalman K. Szabo. Full result for the QCD equation of state with 2+1 flavors. *Phys. Lett.*, B730:99–104, 2014. doi: 10.1016/j.physletb.2014.01.007.
- [58] Andrei D. Linde. Infrared Problem in Thermodynamics of the Yang-Mills Gas. *Phys. Lett.*, B96:289–292, 1980. doi: 10.1016/0370-2693(80)90769-8.
- [59] Yoichiro Nambu and G. Jona-Lasinio. Dynamical Model of Elementary Particles Based on an Analogy with Superconductivity. 1. *Phys. Rev.*, 122:345–358, 1961. doi: 10.1103/PhysRev.122.345.
- [60] Michael Buballa and Stefano Carignano. Inhomogeneous chiral condensates. *Prog. Part. Nucl. Phys.*, 81:39–96, 2015. doi: 10.1016/j.pnpnp.2014.11.001.
- [61] Peter N. Meisinger and Michael C. Ogilvie. Chiral symmetry restoration and Z(N) symmetry. *Phys. Lett.*, B379:163–168, 1996. doi: 10.1016/0370-2693(96)00447-9.
- [62] Kenji Fukushima. Chiral effective model with the Polyakov loop. *Phys. Lett.*, B591:277–284, 2004. doi: 10.1016/j.physletb.2004.04.027.
- [63] Claudia Ratti, Michael A. Thaler, and Wolfram Weise. Phases of QCD: Lattice thermodynamics and a field theoretical model. *Phys. Rev.*, D73:014019, 2006. doi: 10.1103/PhysRevD.73.014019.

- [64] A. Di Giacomo, Hans Gunter Dosch, V. I. Shevchenko, and Yu. A. Simonov. Field correlators in QCD: Theory and applications. *Phys. Rept.*, 372:319–368, 2002. doi: 10.1016/S0370-1573(02)00140-0.
- [65] Yu. A. Simonov. Nonperturbative equation of state of quark-gluon plasma. *Annals Phys.*, 323:783, 2008. doi: 10.1016/j.aop.2007.05.005,10.1016/j.aop.2007.05.007.
- [66] A. V. Nefediev, Yu. A. Simonov, and M. A. Trusov. Deconfinement and quark-gluon plasma. *Int. J. Mod. Phys.*, E18:549–599, 2009. doi: 10.1142/S0218301309012768.
- [67] V. A. Dexheimer and S. Schramm. Chiral Symmetry Restoration and Deconfinement to Quark Matter in Neutron Stars. *Nucl. Phys. Proc. Suppl.*, 199:319–324, 2010. doi: 10.1016/j.nuclphysbps.2010.02.051.
- [68] Z. Fodor and S. D. Katz. Critical point of QCD at finite T and mu, lattice results for physical quark masses. *JHEP*, 04:050, 2004. doi: 10.1088/1126-6708/2004/04/050.
- [69] G. Endrodi, Z. Fodor, S. D. Katz, and K. K. Szabo. The QCD phase diagram at nonzero quark density. *JHEP*, 04:001, 2011. doi: 10.1007/JHEP04(2011)001.
- [70] Philippe de Forcrand and Owe Philipsen. The Chiral critical line of $N(f) = 2+1$ QCD at zero and non-zero baryon density. *JHEP*, 01:077, 2007. doi: 10.1088/1126-6708/2007/01/077.
- [71] Stephen D. H. Hsu and Myckola Schwetz. On the QCD phase transition at finite baryon density. *Phys. Lett.*, B432:203–208, 1998. doi: 10.1016/S0370-2693(98)00615-7.
- [72] Juergen Berges and Krishna Rajagopal. Color superconductivity and chiral symmetry restoration at nonzero baryon density and temperature. *Nucl. Phys.*, B538:215–232, 1999. doi: 10.1016/S0550-3213(98)00620-8.
- [73] Mark G. Alford, Andreas Schmitt, Krishna Rajagopal, and Thomas Schaefer. Color superconductivity in dense quark matter. *Rev. Mod. Phys.*, 80:1455–1515, 2008. doi: 10.1103/RevModPhys.80.1455.
- [74] Roberto Anglani, Roberto Casalbuoni, Marco Ciminale, Nicola Ippolito, Raoul Gatto, Massimo Mannarelli, and Marco Ruggieri. Crystalline color superconductors. *Rev. Mod. Phys.*, 86:509–561, 2014. doi: 10.1103/RevModPhys.86.509.
- [75] P. Braun-Munzinger, J. Stachel, J. P. Wessels, and N. Xu. Thermal equilibration and expansion in nucleus-nucleus collisions at the AGS. *Phys. Lett.*, B344:43–48, 1995. doi: 10.1016/0370-2693(94)01534-J.
- [76] P. Braun-Munzinger, J. Stachel, J. P. Wessels, and N. Xu. Thermal and hadrochemical equilibration in nucleus-nucleus collisions at the SPS. *Phys. Lett.*, B365:1–6, 1996. doi: 10.1016/0370-2693(95)01258-3.
- [77] Francesco Becattini. A Thermodynamical approach to hadron production in $e^+ e^-$ collisions. *Z. Phys.*, C69(3):485–492, 1996. doi: 10.1007/BF02907431.
- [78] F. Becattini and Ulrich W. Heinz. Thermal hadron production in $p p$ and p anti- p collisions. *Z. Phys.*, C76:269–286, 1997. doi: 10.1007/s002880050551. [Erratum: *Z. Phys.*C76,578(1997)].

- [79] F. Becattini, J. Cleymans, A. Keranen, E. Suhonen, and K. Redlich. Features of particle multiplicities and strangeness production in central heavy ion collisions between 1.7A-GeV/c and 158A-GeV/c. *Phys. Rev.*, C64:024901, 2001. doi: 10.1103/PhysRevC.64.024901.
- [80] P. Braun-Munzinger, D. Magestro, K. Redlich, and J. Stachel. Hadron production in Au - Au collisions at RHIC. *Phys. Lett.*, B518:41–46, 2001. doi: 10.1016/S0370-2693(01)01069-3.
- [81] A. Andronic, P. Braun-Munzinger, and J. Stachel. Hadron production in central nucleus-nucleus collisions at chemical freeze-out. *Nucl. Phys.*, A772:167–199, 2006. doi: 10.1016/j.nuclphysa.2006.03.012.
- [82] J. Cleymans, H. Oeschler, K. Redlich, and S. Wheaton. Comparison of chemical freeze-out criteria in heavy-ion collisions. *Phys. Rev.*, C73:034905, 2006. doi: 10.1103/PhysRevC.73.034905.
- [83] Paolo Alba, Wanda Alberico, Rene Bellwied, Marcus Bluhm, Valentina Mantovani Sarti, Marlene Nahrgang, and Claudia Ratti. Freeze-out conditions from net-proton and net-charge fluctuations at RHIC. *Phys. Lett.*, B738:305–310, 2014. doi: 10.1016/j.physletb.2014.09.052.
- [84] Francesco Becattini, Marcus Bleicher, Thorsten Kollegger, Tim Schuster, Jan Steinheimer, and Reinhard Stock. Hadron Formation in Relativistic Nuclear Collisions and the QCD Phase Diagram. *Phys. Rev. Lett.*, 111:082302, 2013. doi: 10.1103/PhysRevLett.111.082302.
- [85] P. Antonioli et al. INFN What Next. *Frascati Phys. Ser.*, 62, 2016.
- [86] Debasish Banerjee, Jajati K. Nayak, and Raju Venugopalan. Two introductory lectures on high energy QCD and heavy ion collisions. *Lect. Notes Phys.*, 785:105–137, 2010. doi: 10.1007/978-3-642-02286-9_3.
- [87] Michael L. Miller, Klaus Reyers, Stephen J. Sanders, and Peter Steinberg. Glauber modeling in high energy nuclear collisions. *Ann. Rev. Nucl. Part. Sci.*, 57:205–243, 2007. doi: 10.1146/annurev.nucl.57.090506.123020.
- [88] Edmond Iancu, Andrei Leonidov, and Larry D. McLerran. Nonlinear gluon evolution in the color glass condensate. 1. *Nucl. Phys.*, A692:583–645, 2001. doi: 10.1016/S0375-9474(01)00642-X.
- [89] Francois Gelis and Raju Venugopalan. Three lectures on multi-particle production in the glasma. *Acta Phys. Polon.*, B37:3253–3314, 2006.
- [90] L. Del Zanna, V. Chandra, G. Inghirami, V. Rolando, A. Beraudo, A. De Pace, G. Pagliara, A. Drago, and F. Becattini. Relativistic viscous hydrodynamics for heavy-ion collisions with ECHO-QGP. *Eur. Phys. J.*, C73:2524, 2013. doi: 10.1140/epjc/s10052-013-2524-5.
- [91] Fred Cooper and Graham Frye. Comment on the Single Particle Distribution in the Hydrodynamic and Statistical Thermodynamic Models of Multiparticle Production. *Phys. Rev.*, D10:186, 1974. doi: 10.1103/PhysRevD.10.186.
- [92] Charles Gale, Sangyong Jeon, Bjoern Schenke, Prithwish Tribedy, and Raju Venugopalan. Event-by-event anisotropic flow in heavy-ion collisions from combined Yang-Mills and viscous fluid dynamics. *Phys. Rev. Lett.*, 110(1):012302, 2013. doi: 10.1103/PhysRevLett.110.012302.
- [93] I. Arsene et al. Quark gluon plasma and color glass condensate at RHIC? The Perspective from the BRAHMS experiment. *Nucl. Phys.*, A757:1–27, 2005. doi: 10.1016/j.nuclphysa.2005.02.130.

- [94] Jean-Yves Ollitrault. Anisotropy as a signature of transverse collective flow. *Phys. Rev.*, D46: 229–245, 1992. doi: 10.1103/PhysRevD.46.229.
- [95] A. Andronic et al. Heavy-flavour and quarkonium production in the LHC era: from proton–proton to heavy-ion collisions. *Eur. Phys. J.*, C76(3):107, 2016. doi: 10.1140/epjc/s10052-015-3819-5.
- [96] T. Matsui and H. Satz. J/ψ Suppression by Quark-Gluon Plasma Formation. *Phys. Lett.*, B178: 416–422, 1986. doi: 10.1016/0370-2693(86)91404-8.
- [97] C. R. Allton, S. Ejiri, S. J. Hands, O. Kaczmarek, F. Karsch, E. Laermann, C. Schmidt, and L. Scorzato. The QCD thermal phase transition in the presence of a small chemical potential. *Phys. Rev.*, D66:074507, 2002. doi: 10.1103/PhysRevD.66.074507.
- [98] O. Kaczmarek, F. Karsch, E. Laermann, C. Miao, S. Mukherjee, P. Petreczky, C. Schmidt, W. Soeldner, and W. Unger. Phase boundary for the chiral transition in (2+1) -flavor QCD at small values of the chemical potential. *Phys. Rev.*, D83:014504, 2011. doi: 10.1103/PhysRevD.83.014504.
- [99] Sz. Borsanyi, G. Endrodi, Z. Fodor, S. D. Katz, S. Krieg, C. Ratti, and K. K. Szabo. QCD equation of state at nonzero chemical potential: continuum results with physical quark masses at order mu^2 . *JHEP*, 08:053, 2012. doi: 10.1007/JHEP08(2012)053.
- [100] Prasad Hegde and Heng-Tong Ding. The curvature of the chiral phase transition line for small values of μ_B . *PoS, LATTICE2015*:141, 2016.
- [101] Philippe de Forcrand and Owe Philipsen. The QCD phase diagram for small densities from imaginary chemical potential. *Nucl. Phys.*, B642:290–306, 2002. doi: 10.1016/S0550-3213(02)00626-0.
- [102] Philippe de Forcrand and Owe Philipsen. The QCD phase diagram for three degenerate flavors and small baryon density. *Nucl. Phys.*, B673:170–186, 2003. doi: 10.1016/j.nuclphysb.2003.09.005.
- [103] Massimo D’Elia and Maria-Paola Lombardo. Finite density QCD via imaginary chemical potential. *Phys. Rev.*, D67:014505, 2003. doi: 10.1103/PhysRevD.67.014505.
- [104] Massimo D’Elia and Maria Paola Lombardo. QCD thermodynamics from an imaginary $\mu(B)$: Results on the four flavor lattice model. *Phys. Rev.*, D70:074509, 2004. doi: 10.1103/PhysRevD.70.074509.
- [105] Vicente Azcoiti, Giuseppe Di Carlo, Angelo Galante, and Victor Laliena. Phase diagram of QCD with four quark flavors at finite temperature and baryon density. *Nucl. Phys.*, B723:77–90, 2005. doi: 10.1016/j.nuclphysb.2005.06.026.
- [106] Liang-Kai Wu, Xiang-Qian Luo, and He-Sheng Chen. Phase structure of lattice QCD with two flavors of Wilson quarks at finite temperature and chemical potential. *Phys. Rev.*, D76:034505, 2007. doi: 10.1103/PhysRevD.76.034505.
- [107] Paolo Cea, Leonardo Cosmai, Massimo D’Elia, and Alessandro Papa. The Critical line from imaginary to real baryonic chemical potentials in two-color QCD. *Phys. Rev.*, D77:051501, 2008. doi: 10.1103/PhysRevD.77.051501.

- [108] Paolo Cea, Leonardo Cosmai, Massimo D’Elia, Chiara Manneschi, and Alessandro Papa. Analytic continuation of the critical line: Suggestions for QCD. *Phys. Rev.*, D80:034501, 2009. doi: 10.1103/PhysRevD.80.034501.
- [109] Paolo Cea, Leonardo Cosmai, Massimo D’Elia, and Alessandro Papa. The phase diagram of QCD with four degenerate quarks. *Phys. Rev.*, D81:094502, 2010. doi: 10.1103/PhysRevD.81.094502.
- [110] Keitaro Nagata and Atsushi Nakamura. Imaginary Chemical Potential Approach for the Pseudo-Critical Line in the QCD Phase Diagram with Clover-Improved Wilson Fermions. *Phys. Rev.*, D83:114507, 2011. doi: 10.1103/PhysRevD.83.114507.
- [111] Paolo Cea, Leonardo Cosmai, Massimo D’Elia, Alessandro Papa, and Francesco Sanfilippo. The critical line of two-flavor QCD at finite isospin or baryon densities from imaginary chemical potentials. *Phys. Rev.*, D85:094512, 2012. doi: 10.1103/PhysRevD.85.094512.
- [112] E. Laermann, Florian Meyer, and M. P. Lombardo. Making the most of Taylor expansion and imaginary μ . *J. Phys. Conf. Ser.*, 432:012016, 2013. doi: 10.1088/1742-6596/432/1/012016.
- [113] Paolo Cea, Leonardo Cosmai, and Alessandro Papa. Critical line of 2+1 flavor QCD. *Phys. Rev.*, D89(7):074512, 2014. doi: 10.1103/PhysRevD.89.074512.
- [114] R. Bellwied, S. Borsanyi, Z. Fodor, J. Guenther, S. D. Katz, C. Ratti, and K. K. Szabo. The QCD phase diagram from analytic continuation. *Phys. Lett.*, B751:559–564, 2015. doi: 10.1016/j.physletb.2015.11.011.
- [115] Paolo Cea, Leonardo Cosmai, and Alessandro Papa. Critical line of 2+1 flavor QCD: Toward the continuum limit. *Phys. Rev.*, D93(1):014507, 2016. doi: 10.1103/PhysRevD.93.014507.
- [116] Z. Fodor and S. D. Katz. Lattice determination of the critical point of QCD at finite T and μ . *JHEP*, 03:014, 2002. doi: 10.1088/1126-6708/2002/03/014.
- [117] Slavo Kratochvila and Philippe de Forcrand. The Canonical approach to finite density QCD. *PoS*, LAT2005:167, 2006.
- [118] Andrei Alexandru, Manfred Faber, Ivan Horvath, and Keh-Fei Liu. Lattice QCD at finite density via a new canonical approach. *Phys. Rev.*, D72:114513, 2005. doi: 10.1103/PhysRevD.72.114513.
- [119] A. Bazavov et al. Additional Strange Hadrons from QCD Thermodynamics and Strangeness Freezeout in Heavy Ion Collisions. *Phys. Rev. Lett.*, 113(7):072001, 2014. doi: 10.1103/PhysRevLett.113.072001.
- [120] S. Borsanyi, Z. Fodor, S. D. Katz, S. Krieg, C. Ratti, and K. K. Szabo. Freeze-out parameters: lattice meets experiment. *Phys. Rev. Lett.*, 111:062005, 2013. doi: 10.1103/PhysRevLett.111.062005.
- [121] M. Cheng et al. The QCD equation of state with almost physical quark masses. *Phys. Rev.*, D77:014511, 2008. doi: 10.1103/PhysRevD.77.014511.
- [122] Massimo D’Elia and Francesco Sanfilippo. Thermodynamics of two flavor QCD from imaginary chemical potentials. *Phys. Rev.*, D80:014502, 2009. doi: 10.1103/PhysRevD.80.014502.
- [123] Massimo D’Elia, Francesco Di Renzo, and Maria Paola Lombardo. The Strongly interacting quark gluon plasma, and the critical behaviour of QCD at imaginary μ . *Phys. Rev.*, D76:114509, 2007. doi: 10.1103/PhysRevD.76.114509.

- [124] M. A. Clark, A. D. Kennedy, and Z. Sroczynski. Exact 2+1 flavour RHMC simulations. *Nucl. Phys. Proc. Suppl.*, 140:835–837, 2005. doi: 10.1016/j.nuclphysbps.2004.11.192. [,835(2004)].
- [125] M. A. Clark and A. D. Kennedy. Accelerating Staggered Fermion Dynamics with the Rational Hybrid Monte Carlo (RHMC) Algorithm. *Phys. Rev.*, D75:011502, 2007. doi: 10.1103/PhysRevD.75.011502.
- [126] M. A. Clark and A. D. Kennedy. Accelerating dynamical fermion computations using the rational hybrid Monte Carlo (RHMC) algorithm with multiple pseudofermion fields. *Phys. Rev. Lett.*, 98:051601, 2007. doi: 10.1103/PhysRevLett.98.051601.
- [127] Claudio Bonati, Massimo D’Elia, Marco Mariti, Michele Mesiti, Francesco Negro, and Francesco Sanfilippo. Curvature of the chiral pseudocritical line in QCD. *Phys. Rev.*, D90(11):114025, 2014. doi: 10.1103/PhysRevD.90.114025.
- [128] S. Ejiri, F. Karsch, E. Laermann, C. Miao, S. Mukherjee, P. Petreczky, C. Schmidt, W. Soeldner, and W. Unger. On the magnetic equation of state in (2+1)-flavor QCD. *Phys. Rev.*, D80:094505, 2009. doi: 10.1103/PhysRevD.80.094505.
- [129] Maria-Paola Lombardo. Finite density (might well be easier) at finite temperature. *Nucl. Phys. Proc. Suppl.*, 83:375–377, 2000. doi: 10.1016/S0920-5632(00)91678-5.
- [130] Massimo D’Elia and Francesco Sanfilippo. The Order of the Roberge-Weiss endpoint (finite size transition) in QCD. *Phys. Rev.*, D80:111501, 2009. doi: 10.1103/PhysRevD.80.111501.
- [131] Claudio Bonati, Guido Cossu, Massimo D’Elia, and Francesco Sanfilippo. The Roberge-Weiss endpoint in $N_f = 2$ QCD. *Phys. Rev.*, D83:054505, 2011. doi: 10.1103/PhysRevD.83.054505.
- [132] Philippe de Forcrand and Owe Philipsen. Constraining the QCD phase diagram by tricritical lines at imaginary chemical potential. *Phys. Rev. Lett.*, 105:152001, 2010. doi: 10.1103/PhysRevLett.105.152001.
- [133] Andrei Alexandru and Anyi Li. QCD at imaginary chemical potential with Wilson fermions. *PoS, LATTICE2013*:208, 2014.
- [134] Liang-Kai Wu and Xiang-Fei Meng. Nature of the Roberge-Weiss transition end points in two-flavor lattice QCD with Wilson quarks. *Phys. Rev.*, D87(9):094508, 2013. doi: 10.1103/PhysRevD.87.094508.
- [135] Liang-Kai Wu and Xiang-Fei Meng. Nature of Roberge-Weiss transition endpoints for heavy quarks in $N_f = 2$ lattice QCD with Wilson fermions. *Phys. Rev.*, D90(9):094506, 2014. doi: 10.1103/PhysRevD.90.094506.
- [136] Keitaro Nagata, Kouji Kashiwa, Atsushi Nakamura, and Shinsuke M. Nishigaki. Lee-Yang zero distribution of high temperature QCD and the Roberge-Weiss phase transition. *Phys. Rev.*, D91(9):094507, 2015. doi: 10.1103/PhysRevD.91.094507.
- [137] Takahiro Makiyama, Yuji Sakai, Takuya Saito, Masahiro Ishii, Junichi Takahashi, Kouji Kashiwa, Hiroaki Kouno, Atsushi Nakamura, and Masanobu Yahiro. Phase structure of two-color QCD at real and imaginary chemical potentials; lattice simulations and model analyses. *Phys. Rev.*, D93(1):014505, 2016. doi: 10.1103/PhysRevD.93.014505.

- [138] Christopher Czaban, Francesca Cuteri, Owe Philipsen, Christopher Pinke, and Alessandro Sciarra. Roberge-Weiss transition in $N_f = 2$ QCD with Wilson fermions and $N_\tau = 6$. *Phys. Rev.*, D93(5): 054507, 2016. doi: 10.1103/PhysRevD.93.054507.
- [139] Christopher Pinke and Owe Philipsen. The $N_f = 2$ chiral phase transition from imaginary chemical potential with Wilson Fermions. *PoS, LATTICE2015*:149, 2016.
- [140] Thomas DeGrand and Roland Hoffmann. QCD with one compact spatial dimension. *JHEP*, 02: 022, 2007. doi: 10.1088/1126-6708/2007/02/022.
- [141] Biagio Lucini, Agostino Patella, and Claudio Pica. Baryon currents in QCD with compact dimensions. *Phys. Rev.*, D75:121701, 2007. doi: 10.1103/PhysRevD.75.121701.
- [142] Hiroaki Kouno, Yuji Sakai, Kouji Kashiwa, and Masanobu Yahiro. Roberge-Weiss phase transition and its endpoint. *J. Phys.*, G36:115010, 2009. doi: 10.1088/0954-3899/36/11/115010.
- [143] Yuji Sakai, Kouji Kashiwa, Hiroaki Kouno, Masayuki Matsuzaki, and Masanobu Yahiro. Determination of QCD phase diagram from the imaginary chemical potential region. *Phys. Rev.*, D79:096001, 2009. doi: 10.1103/PhysRevD.79.096001.
- [144] Yuji Sakai, Takahiro Sasaki, Hiroaki Kouno, and Masanobu Yahiro. Entanglement between deconfinement transition and chiral symmetry restoration. *Phys. Rev.*, D82:076003, 2010. doi: 10.1103/PhysRevD.82.076003.
- [145] Takahiro Sasaki, Yuji Sakai, Hiroaki Kouno, and Masanobu Yahiro. Quark-mass dependence of the three-flavor QCD phase diagram at zero and imaginary chemical potential: Model prediction. *Phys. Rev.*, D84:091901, 2011. doi: 10.1103/PhysRevD.84.091901.
- [146] Hiroaki Kouno, Mizuho Kishikawa, Takahiro Sasaki, Yuji Sakai, and Masanobu Yahiro. Spontaneous parity and charge-conjugation violations at real isospin and imaginary baryon chemical potentials. *Phys. Rev.*, D85:016001, 2012. doi: 10.1103/PhysRevD.85.016001.
- [147] Gert Aarts, S. Prem Kumar, and James Rafferty. Holographic Roberge-Weiss Transitions. *JHEP*, 07:056, 2010. doi: 10.1007/JHEP07(2010)056.
- [148] James Rafferty. Holographic Roberge Weiss Transitions II - Defect Theories and the Sakai Sugimoto Model. *JHEP*, 09:087, 2011. doi: 10.1007/JHEP09(2011)087.
- [149] Kenji Morita, Vladimir Skokov, Bengt Friman, and Krzysztof Redlich. Probing deconfinement in a chiral effective model with Polyakov loop at imaginary chemical potential. *Phys. Rev.*, D84: 076009, 2011. doi: 10.1103/PhysRevD.84.076009.
- [150] Kouji Kashiwa, Thomas Hell, and Wolfram Weise. Nonlocal Polyakov-Nambu-Jona-Lasinio model and imaginary chemical potential. *Phys. Rev.*, D84:056010, 2011. doi: 10.1103/PhysRevD.84.056010.
- [151] V. Pagura, D. Gomez Dumm, and N. N. Scoccola. Deconfinement and chiral restoration in nonlocal PNJL models at zero and imaginary chemical potential. *Phys. Lett.*, B707:76–82, 2012. doi: 10.1016/j.physletb.2011.11.064.
- [152] David Scheffler, Michael Buballa, and Jochen Wambach. PNJL Model Analysis of the Roberge-Weiss Transition Endpoint at Imaginary Chemical Potential. *Acta Phys. Polon. Supp.*, 5:971–976, 2012. doi: 10.5506/APhysPolBSupp.5.971.

- [153] Kouji Kashiwa and Robert D. Pisarski. Roberge-Weiss transition and 't Hooft loops. *Phys. Rev.*, D87(9):096009, 2013. doi: 10.1103/PhysRevD.87.096009.
- [154] Kouji Kashiwa, Takahiro Sasaki, Hiroaki Kouno, and Masanobu Yahiro. Two-color QCD at imaginary chemical potential and its impact on real chemical potential. *Phys. Rev.*, D87(1):016015, 2013. doi: 10.1103/PhysRevD.87.016015.
- [155] Frank Wilczek. Application of the renormalization group to a second order QCD phase transition. *Int. J. Mod. Phys.*, A7:3911–3925, 1992. doi: 10.1142/S0217751X92001757. [Erratum: *Int. J. Mod. Phys.*A7,6951(1992)].
- [156] C. Domb and J. L. Lebowitz, editors. *PHASE TRANSITIONS AND CRITICAL PHENOMENA. VOL. 11.* 1987.
- [157] Claudio Bonati, Massimo D’Elia, Marco Mariti, Michele Mesiti, Francesco Negro, and Francesco Sanfilippo. Roberge-Weiss endpoint at the physical point of $N_f = 2 + 1$ QCD. *Phys. Rev.*, D93(7):074504, 2016. doi: 10.1103/PhysRevD.93.074504.
- [158] Szabolcs Borsanyi et al. High-precision scale setting in lattice QCD. *JHEP*, 09:010, 2012. doi: 10.1007/JHEP09(2012)010.
- [159] Martin Luescher. Properties and uses of the Wilson flow in lattice QCD. *JHEP*, 08:071, 2010. doi: 10.1007/JHEP08(2010)071, 10.1007/JHEP03(2014)092. [Erratum: *JHEP*03,092(2014)].
- [160] H. W. J. Blote, E. Luijten, and J. R. Heringa. Ising universality in three dimensions: a Monte Carlo study. *Journal of Physics A Mathematical General*, 28:6289–6313, November 1995. doi: 10.1088/0305-4470/28/22/007.
- [161] K. Binder. Finite size scaling analysis of Ising model block distribution functions. *Z. Phys.*, B43:119–140, 1981. doi: 10.1007/BF01293604.
- [162] K. Binder. Critical Properties from Monte Carlo Coarse Graining and Renormalization. *Phys. Rev. Lett.*, 47:693–696, 1981. doi: 10.1103/PhysRevLett.47.693.
- [163] Andrea Pelissetto and Ettore Vicari. Critical phenomena and renormalization group theory. *Phys. Rept.*, 368:549–727, 2002. doi: 10.1016/S0370-1573(02)00219-3.
- [164] Mehran Kardar. *Statistical Physics of Fields.* Cambridge University Press, 2007. ISBN 978-0-521-87341-3.
- [165] John Cardy. *Scaling and Renormalization in Statistical Physics.* Cambridge University Press, Cambridge, 004 1996. ISBN 9781316036440. doi: 10.1017/CBO9781316036440. URL <https://www.cambridge.org/core/books/scaling-and-renormalization-in-statistical-physics/924C0B0D39123F681CF3353C42E5E836>.
- [166] M.E.J. Newman and G.T. Barkema. *Monte Carlo Methods in Statistical Physics.* Clarendon Press, 1999. ISBN 9780198517979.
- [167] L.D. Landau and E.M. Lifshitz. *Statistical Physics.* Number v. 5. 2013. ISBN 9780080570464.
- [168] K. Binder and D. P. Landau. Finite-size scaling at first-order phase transitions. *Phys. Rev.*, B30(3):1477, 1984. doi: 10.1103/PhysRevB.30.1477.

- [169] Murty S. S. Challa, D. P. Landau, and K. Binder. Finite size effects at temperature driven first order transitions. *Phys. Rev.*, B34:1841–1852, 1986. doi: 10.1103/PhysRevB.34.1841.
- [170] Christian Borgs and Roman Kotecky. A Rigorous Theory of Finite Size Scaling at First Order Phase Transitions. *J. Stat. Phys.*, 61:79, 1990.
- [171] Christian Borgs and Roman Kotecky. Finite size effects at asymmetric first order phase transitions. *Phys. Rev. Lett.*, 68:1734–1737, 1992. doi: 10.1103/PhysRevLett.68.1734.
- [172] R. J. Baxter. Potts model at critical temperature. *J. Phys.*, C6:L445–L448, 1973.
- [173] Claudio Bonati and Massimo D’Elia. The three-dimensional, three state Potts model in a negative external field. *Phys. Rev.*, D82:114515, 2010. doi: 10.1103/PhysRevD.82.114515.
- [174] Claudio Bonati and Massimo D’Elia. Phase diagram of the 4D U(1) model at finite temperature. *Phys. Rev.*, D88(6):065025, 2013. doi: 10.1103/PhysRevD.88.065025.
- [175] H W J Blote, E Luijten, and J R Heringa. Ising universality in three dimensions: a monte carlo study. *Journal of Physics A: Mathematical and General*, 28(22):6289, 1995. URL <http://stacks.iop.org/0305-4470/28/i=22/a=007>.
- [176] A. M. Ferrenberg and R. H. Swendsen. New Monte Carlo Technique for Studying Phase Transitions. *Phys. Rev. Lett.*, 61:2635–2638, 1988. doi: 10.1103/PhysRevLett.61.2635.
- [177] Alan M. Ferrenberg and Robert H. Swendsen. Optimized Monte Carlo analysis. *Phys. Rev. Lett.*, 63:1195–1198, 1989. doi: 10.1103/PhysRevLett.63.1195.
- [178] Claudio Bonati, Massimo D’Elia, Marco Mariti, Guido Martinelli, Michele Mesiti, Francesco Negro, Francesco Sanfilippo, and Giovanni Villadoro. Axion phenomenology and θ -dependence from $N_f = 2 + 1$ lattice QCD. *JHEP*, 03:155, 2016. doi: 10.1007/JHEP03(2016)155.
- [179] Kenneth G. Wilson. Confinement of Quarks. *Phys. Rev.*, D10:2445–2459, 1974. doi: 10.1103/PhysRevD.10.2445. [,45(1974)].
- [180] D. H. Weingarten and D. N. Petcher. Monte Carlo Integration for Lattice Gauge Theories with Fermions. *Phys. Lett.*, B99:333–338, 1981. doi: 10.1016/0370-2693(81)90112-X.
- [181] S. Duane, A. D. Kennedy, B. J. Pendleton, and D. Roweth. Hybrid Monte Carlo. *Phys. Lett.*, B195:216–222, 1987. doi: 10.1016/0370-2693(87)91197-X.
- [182] A. D. Kennedy. Algorithms for dynamical fermions. *arXiv*, hep-lat:0607038, 2006.
- [183] Beat Jegerlehner. Krylov space solvers for shifted linear systems. *arXiv*, hep-lat:9612014, 1996.
- [184] Thomas DeGrand and Carleton E. Detar. *Lattice methods for quantum chromodynamics*. New Jersey, USA: World Scientific, 2006.
- [185] Thomas A. DeGrand and Pietro Rossi. Conditioning Techniques for Dynamical Fermions. *Comput. Phys. Commun.*, 60:211–214, 1990. doi: 10.1016/0010-4655(90)90006-M.
- [186] J. C. Sexton and D. H. Weingarten. Hamiltonian evolution for the hybrid Monte Carlo algorithm. *Nucl. Phys.*, B380:665–677, 1992. doi: 10.1016/0550-3213(92)90263-B.

- [187] C. Urbach, K. Jansen, A. Shindler, and U. Wenger. HMC algorithm with multiple time scale integration and mass preconditioning. *Comput. Phys. Commun.*, 174:87–98, 2006. doi: 10.1016/j.cpc.2005.08.006.
- [188] I. P. Omelyan, I. M. Mryglod, and R. Folk. Optimized verlet-like algorithms for molecular dynamics simulations. *Phys. Rev. E*, 65:056706, May 2002. doi: 10.1103/PhysRevE.65.056706. URL <http://link.aps.org/doi/10.1103/PhysRevE.65.056706>.
- [189] I.P. Omelyan, I.M. Mryglod, and R. Folk. Symplectic analytically integrable decomposition algorithms: classification, derivation, and application to molecular dynamics, quantum and celestial mechanics simulations. *Computer Physics Communications*, 151(3):272 – 314, 2003. ISSN 0010-4655. doi: [http://dx.doi.org/10.1016/S0010-4655\(02\)00754-3](http://dx.doi.org/10.1016/S0010-4655(02)00754-3). URL <http://www.sciencedirect.com/science/article/pii/S0010465502007543>.
- [190] Tetsuya Takaishi and Philippe de Forcrand. Testing and tuning new symplectic integrators for hybrid Monte Carlo algorithm in lattice QCD. *Phys. Rev.*, E73:036706, 2006. doi: 10.1103/PhysRevE.73.036706.
- [191] P. De Forcrand, D. Lellouch, and C. Roiesnel. OPTIMIZING A LATTICE QCD SIMULATION PROGRAM. *J. Comput. Phys.*, 59:324–330, 1985. doi: 10.1016/0021-9991(85)90149-4.
- [192] M. A. Clark, R. Babich, K. Barros, R. C. Brower, and C. Rebbi. Solving Lattice QCD systems of equations using mixed precision solvers on GPUs. *Comput. Phys. Commun.*, 181:1517–1528, 2010. doi: 10.1016/j.cpc.2010.05.002.
- [193] Simon Heybrock, Balint Joo, Dhiraj D. Kalamkar, Mikhail Smelyanskiy, Karthikeyan Vaidyanathan, Tilo Wettig, and Pradeep Dubey. Lattice QCD with Domain Decomposition on Intel Xeon Phi Co-Processors. In *The International Conference for High Performance Computing, Networking, Storage, and Analysis: SC14: HPC matters (SC) New Orleans, LA, USA, November 16-21, 2014*, 2014. doi: 10.1109/SC.2014.11. URL <http://inspirehep.net/record/1333236/files/arXiv:1412.2629.pdf>.
- [194] Milc Collaboration. The MILC Lattice Computation (MILC) Collaboration, 2017. URL <http://www.physics.utah.edu/~detar/milc/>.
- [195] Francesco Sanfilippo. NISSA Is a Set of Su(3) Algorithms, 2017. URL <https://github.com/sunpho84/nissa/>.
- [196] C. Bonati, G. Cossu, M. D’Elia, and P. Incardona. QCD simulations with staggered fermions on GPUs. *Comput. Phys. Commun.*, 183:853–863, 2012. doi: 10.1016/j.cpc.2011.12.011.
- [197] E. Calore, N. Demo, S. F. Schifano, and R. Tripiccion. Experience on vectorizing lattice boltzmann kernels for multi- and many-core architectures. In *Parallel Processing and Applied Mathematics: 11th International Conference, PPAM 2015, Krakow, Poland, September 6-9, 2015. Revised Selected Papers, Part I*, pages 53 – 62. Springer International Publishing, 2016. doi: http://dx.doi.org/10.1007/978-3-319-32149-3_6.
- [198] Claudio Bonati, Enrico Calore, Simone Coscetti, Massimo D’Elia, Michele Mesiti, Francesco Negro, Sebastiano Fabio Schifano, and Raffaele Tripiccion. Designing and Optimizing LQCD codes using OpenACC. In *Proceedings, GPU Computing in High-Energy Physics (GPUHEP2014): Pisa, Italy, September 10-12, 2014*, pages 151–156, 2015. doi: 10.3204/

DESY-PROC-2014-05/27. URL <http://inspirehep.net/record/1386632/files/27.pdf>.

- [199] M. A. Clark, Ph. de Forcrand, and A. D. Kennedy. Algorithm shootout: R versus RHMC. *PoS, LAT2005*:115, 2006.
- [200] P. Hasenfratz and F. Karsch. FINITE FERMION DENSITY ON THE LATTICE. *Phys. Rept.*, 103:219–223, 1984. doi: 10.1016/0370-1573(84)90083-8.